A SIMPLIFIED MODEL FOR UNDERSTANDING THE EVOLUTION OF CIRRUS CLOUDS

by

Clinton Todd Schmidt

A thesis submitted to the faculty of
The University of Utah
in partial fulfillment of the requirements for the degree of

Master of Science

Department of Atmospheric Sciences

The University of Utah

May 2011

The University of Utah Graduate School

STATEMENT OF THESIS APPROVAL

The thesis of **Clinton Todd Schmidt**
has been approved by the following supervisory committee members:

Timothy Garrett	, Chair	**11-09-2010** Date Approved
Steven Krueger	, Member	**11-09-2010** Date Approved
Jay Mace	, Member	**11-09-2010** Date Approved

and by **W. James Steenburgh** , Chair of
the Department of **Atmospheric Sciences**

and by Charles A. Wight, Dean of The Graduate School.

ABSTRACT

Developing an understanding of cloud evolution is central to understanding the climate system as a whole. Stratiform cirrus layers play a significant role in the radiative interaction with the climate system. Radiational effects are a driving force in the dynamic evolution of these layers, particularly in determining the areal coverage, vertical distribution, and microphysical properties of the stratiform clouds. The deposition of energy by radiative flux divergence in a cloud layer provides potential energy to drive cloud evolution.

This work uses a large eddy simulation model (LESM) to investigate a number of parameters that can be used to easily predict how a cirrus cloud will evolve. This work also includes a study of the sensitivity of formation of mammatus-like features in clouds to the below cloud layer relative humidity.

Three distinct modes of cloud evolution were found to occur due to the radiative processes simulated in this study. These modes include isentropic adjustment, mixing, and evaporation/condensation. These modes of evolution were found to be independent of each other in the sense that one mode did not always occur with either of the other two modes. Similarly, the modes of evolution did not always occur in isolation and were found to simultaneously occur in many cases. Two dimensionless numbers are derived in this work that provide a basic framework for understanding the modes of evolution that can be expected of an initial cloud. These dimensionless numbers are found to have strong predictive power for cloud evolution.

The simulations of several clouds produced mammatus-like structures forming at the base of the simulated clouds at the end of the model runs. These formations prompted further investigation of the processes that influence mammatus formation. The theory proposed by this work is that the mammatus cloud formation is a radiative process, mediated by the below cloud layer relative humidity. Several simulations were performed to test this theory. The analysis of these simulated clouds determined the varying degree of mammatus formation through a variety of methods. These analytical methods indicate that the below cloud layer relative humidity plays a substantial role in the formation of mammatus clouds by mediating the radiative energy from the warm surface that is available to the cloud.

TABLE OF CONTENTS

Chapter

Appendices

ACKNOWLEDGMENTS

I'd like to thank my advisor Dr. Tim Garrett for his insight into cloud evolution and radiative processes as well as his patience and guidance through the process of writing this thesis. I'd like to thank the members of my thesis committe, Dr. Jay Mace and Dr. Steve Krueger, for their insights and assistance in writing and editing of this thesis. I'd also like to thank Dr. Mike Zulauf for the UU LES code as well as help in getting it working and the output in a easy to work with format. I'd like to thank Stina Kihlgren for her previous work as well as the basic Matlab scripts for analysis that she developed. I would especially like to thank Melissa Maestas for her efforts in helping to get the UU LES model code working again after every computer system update, as well as her work on streamlining the Matlab scripts and making them much more robust that I could have alone. I would also like to thank Martin Cuma at the Center for High Performance Computing at the University of Utah for his seemingly limitless knowledge on the subject of computing in general and parallel processing in particular as well as for his help in getting the model up and running again after each system update. I am also very grateful for the work that Céline Cornet at the University of Lille in France has done at Dr. Garrett's request in creating the wonderful images of the model output using SHDOM. Last, but not least, I'd like to thank my friends throughout the department of Atmospheric Sciences and the University of Utah and in Salt Lake City for making the time not spent working on this master's thesis a thoroughly enjoyable experience.

This research was funded through a grant to Dr. Garrett from the NASA New Investigator Program, award number NNX06AE24G.

CHAPTER 1

INTRODUCTION

Terrestrial clouds modify both incoming solar shortwave radiation through reflection and absorption (a cooling effect) and outgoing longwave thermal radiation through absorption and re-emission at usually lower temperatures and intensities (a warming effect). While both of these globally-averaged effects are large, amounting to 31.3 W m^2 of warming and 44.5 W m^2 of cooling (from Earth Radiation Budget Experiment (ERBE) data (Kiehl et al., 1994)), they have opposing effects on the global energy budget and largely cancel each other out, leaving a much smaller net impact on the global energy balance (Ramanathan et al., 1989) . An increase or decrease in either the warming or cooling effects of clouds without a corresponding change in the other would lead to a shift in the current globally averaged value of cloud radiative forcing of -13.2 W m^2 (Ramanathan et al., 1989).

Since clouds play a significant role in determining the global energy balance of the Earth (Sellers, 1969; Wetherald and Manabe, 1980; Hartmann et al., 1992), it is important to understand how clouds might evolve under the changing climate conditions forced by growing concentrations of atmospheric carbon dioxide (Schneider, 1972; Cess, 1976; Slingo, 1989). Variations in cloud expanse and lifetime have a strong impact on the local radiation field (Webster and Stephens, 1980) and understanding how the interaction of radiation and clouds might change in response to a warming atmosphere is necessary for understanding global-scale climate feedbacks (Hartmann and Larson, 2002; Soden and Held, 2006; Stephens, 2005).

The behavior of clouds in response to varying global temperatures is one of the largest uncertainties in current climate models (Slingo, 1989; Senior, 1999). To conduct a sensitivity study on the effect of clouds on global radiative balances, it is necessary to first understand the behavior and evolution of clouds under a static climatological condition where the temperature profile and chemical makeup of the atmosphere and their interactions with the various feedback effects in the climate system remain constant (Stephens, 2005). Cloud-climate feedbacks currently account for a large portion of the existing uncertainty in climate modeling (Dufresne and Bony, 2008) due to poor understanding of how clouds both drive and respond to the general circulation, the hydrological cycle, and the atmospheric radiation budget. By improving understanding of cloud evolution for current conditions, it should be possible to improve forecasts of their response and impacts on a future global climate. This could be done by improving the parameterization of clouds in global climate models as well as smaller scale regional climate models.

On scales on the order of the size of a cloud droplet, the relevant governing equations are well described (Rogers and Yau, 1989; Salby, 1996). Extending these equations to larger scale parameterizations is more difficult due to a wide range of dynamically interacting spatial and time scales, including radiation, aerosols, latent heating, microphysical changes (Dobbie and Jonas, 2001). Often, simplifications can lead to inadequate representations of bulk cloud properties at GCM grid scales (Fu and Liou, 2008).

However, there has been some success in parameterizing the governing equations such that they function for larger scales without needing to know the details at the scale of cloud droplets, using bulk quantities such as a parcel average relative humidity, rather than relative humidity of the air directly adjacent to the cloud droplet, and updraft velocity as a proxy for the local processes (Fu and Liou, 2008; Hong et al., 2004). The cloud parameterizations in global climate models as well as regional numeric weather prediction models take advantage of this. Essentially, the small scale processes that depend on the characteristics of the atmosphere directly adjacent to the cloud droplet can be statistically averaged and reduced to equations depending on larger scale, measurable quantities. These are the governing equations of current numerical weather prediction models. For example, a cloud mass mixing ratio q parameterization proposed (Tompkins, 2002) for the ECMWF (European Center for Medium-range Weather Forecasts) is

$$\frac{dq}{dt} = (q_0 - q)(\frac{1}{\tau_v} - \frac{1}{\tau_h}) \tag{1.1}$$

where q_0 is the initial spatial distribution function of cloud mass mixing ratio, τ_h is the timescale for horizontal mixing, respectively, and τ_v is a timescale for energy dissipation due to three dimensional turbulence.

Improving cloud parameterizations through observational studies alone presents significant challenges (Wang and Sassen, 2002). Not only are observational studies expensive in both resources, cost, and manpower, but the data collected is subject to environmental factors beyond the control of the study (i.e. what types of cloud, if any are observed) and can require long running data sets to provide statistically sound measurements (Campbell et al., 2002). An observational study can be designed to occur in favorable places and times for the occurrence of the cloud that the study wishes to observe, however rapid changes in environmental variables and from cloud to cloud introduce additional variables that are difficult to account for in subsequent data analysis.

Given the challenges of observational studies, it is often advantageous to investigate theories relating to clouds using both theoretical and mathematical models. These have the distinct advantage of having all elements controlled, so single parameters may be varied to investigate results.

1.1 Theoretical Studies of Cloud Evolution

1.1.1 Numerical Models

There are two basic approaches to modeling cloud evolution. There is both a top-down approach and a bottom-up approach. In a bottom-up approach to modeling of cloud evolution, the full complexity of the system is explicitly modeled in an attempt to gain understanding of the various interactions of cloud processes with each other. On the other hand, a top-down approach strips out many of the complicating complex internal facets of the cloud and builds an understanding of the basics of cloud evolution from an understanding of externally imposed thermodynamic constraints.

One of the earliest top-down frameworks was the “Mixed-Layer-Model” (Lilly, 1968) developed to simulate the sustained marine stratocumulus cloud decks that are often observed at the top of oceanic planetary boundary layers. Clouds evolved naturally through the balancing effects of turbulent fluxes of heat and moisture from the ocean below, radiative cooling of the cloud layer, and turbulent entrainment of dry air from the free troposphere above cloud top. Modeled enthalpy and moisture flux convergence rates based on climatological means led to simulated stratus cloud evolution that was in general agreement with observations.

Lilly extended the cloud model from his earlier work to describe a cloud layer bounded above and below by a stable layer at a generalized level of the atmosphere, and in particular, cirrus clouds and their outflows (Lilly, 1988). This improved model demonstrated that simplified models can recreate real phenomenon. However, several unrealistic assumptions were used. The cloud layer was assumed to be well mixed, when in actuality, a floating anvil cirrus layer can possess significant stratification, similar to that of the surrounding atmosphere (Garrett et al., 2005). The other assumption that doesn’t hold true when extending the earlier mixed-layer model to cirrus anvils is that Lilly’s anvil cirrus cloud model allowed only for vertical deepening, assuming the cloud had an effectively infinite extent horizontally. While this may be effectively true for central portions of extensive cirrus decks, cirrus anvils spread significantly in the horizontal direction Krueger and Zulauf (2005). In fact, it has been shown that anvil cirrus must spread horizontally due to radiatively driven heating at cloud base and top (Garrett et al., 2005, 2006b).

Other work suggests that the outflow of tropical convection can persist as sub-visible cirrus clouds for several days (Jensen et al., 1996). While made up of relatively small ice crystals ($< 10\mu$m), these clouds can have relatively large ice crystal number densities (> 0.5cm^{-3}). If absorbed radiation drives sustained heating of a cloud layer at constant pressure, the cloud will dissipate quickly. However, if the absorbed radiation drives vertical motions within the cloud layer, increasing supersaturation with respect to ice can drive diffusional growth of cloud ice particles. As the layer ascends, it moves into the stratosphere, where the diffusional growth will draw moisture out of the stratosphere due to the ambient supersaturation, eventually resulting in the removal of water from the stratosphere as the ice crystals fall out when they become large. This model of cloud evolution proposed by Jensen et al. is important since it can be used to explain stratospheric dehydration.

Similar to the work by Jensen et al., Corti et al. (2005) investigated the source of vertical mass flux from the upper tropical troposphere into the stratosphere. Several mechanisms were identified, including the Brewer-Dobson circulation, extremely deep convection, wave dissipation, and infrared cloud heating. Vertical motions driven by cloud radiative heating were found to be confined to the lower levels of the stratosphere, but the identification of their contribution to mass flux into the stratosphere highlights the importance of the interaction of radiation with cloud condensate.

Hartmann and Larson (2002) proposed that the detrainment of convective towers occurs preferentially at a specific temperature that corresponds to the pressure at which radiative cooling at the top of a cirrus anvil is maximized. The pressure level is controlled by the vertical profile of water vapor. In simulations that used different air temperature profiles, the detrained cirrus anvils consistently occurred at a constant temperature. Given that this work suggests that the cloud top temperature of cirrus anvils is roughly constant, this theory has been named the “Fixed Anvil Temperature” or FAT hypothesis.

Subsequent work has validated the FAT hypothesis in both observational and modeling studies. Work by Xu et al. (2007) utilized data from the CERES (Clouds and the Earth’s Radiant Energy System) experiment during the 1998 El Niño to show that observations suggest that the detrainment height of tropical anvils is strongly regulated by temperature at anvil top. In conjunction, a series of simulations using a cloud resolving model to explicitly resolve the convective motions of the cirrus anvils were conducted by Kuang and Hartmann (2007). Their work varied sea surface temperature as well as the profiles of several greenhouse gasses. The result of these simulations was that the temperature of anvil detrainment was notably insensitive to variations in surface temperature as well as greenhouse gas composition.

The importance of the work that has been done to validate the FAT hypothesis is that it suggests that the detrainment height of convective anvils occurs preferentially where clouds can cool by most efficiently radiating atmospheric energy to space. It demonstrates that interactions between clouds and radiation are of a fundamental phenomenon to the earth-climate system.

1.1.2 Cirrus-Radiation Interactions

The work conducted by Hartmann and Larson (2002) suggests that cirrus cloud properties, along with the properties of other cloud types (e.g., deep convection), may be fundamentally constrained by interactions with atmospheric radiation. Conversely, cirrus clouds themselves strongly influence local and global weather and climate processes through their interaction with atmospheric radiation and subsequently the radiation budget of the earth and atmosphere (Fu and Liou, 2008). As such, the evolving interactions between cloud condensate and solar and thermal radiation require quantification.

A study by Ackerman et al. (1988) used satellite measurements of cloud top temperature, ice-water path, and optical depth and high altitude aircraft measurements of temperature, total water concentration, and ice crystal size distribution to calculate the heating rate and vertical profile of the heating rate inside cirrus anvils due to radiative flux divergence within the anvil. They determined that the heating at cloud base and cloud top, as well as the vertical profile of heating within the cloud, are determined primarily by the ice-water content and the distribution of the ice with respect to height inside the cloud. Strong infrared heating and cooling gradients are possible in clouds with substantial ice content. Thick cirrus clouds between 15 and 17 km in altitude with ice water contents (IWC) of 0.1 g m^{-1} have heating rates of 68 K d^{-1} at cloud base and cooling rates of 23 K d^{-1} at cloud top. Their work also indicates that, while the infrared spectrum dominates the heating/cooling of a cloud, the effect of solar radiation, particularly in the tropics where solar radiation is the most intense, is not necessarily negligible. Also included in the work by Ackerman et al. (1988) was a calculation of how radiative heating of a cloud could drive vertical motion of the cloud. Their calculations, however, assumed that the heating was distributed throughout the depth of the cloud through turbulent mixing and the cloud itself could be treated as an individual parcel that moved vertically in a uniform fashion.

Ramanathan et al. (1983) demonstrated that interactions of radiation with clouds play a major role in the general circulation. The treatment of cirrus anvils as a specific type of cloud, rather than part of a general cloud parameterization produced a significant improvement in the modeling of the general circulation. Likewise, a study of cirrus clouds by Star and Cox highlighted the importance of understanding the development and evolution of cirrus clouds (Starr and Cox, 1985a,b). In their study, a simplified cirrus cloud model was utilized to probe the role of various physical processes in the life cycle of the cloud. The goal was to provide a better understanding of cloud evolution such that an appropriate parameterization for the formation and maintenance of cirrus clouds could be implemented in large scale models. They determined that radiative interaction with condensate in cirrus clouds plays an important role in determining the microphysical properties of the clouds as well as adjustment of potential temperature profiles of the atmosphere. These effects were on both a local and global scale due to the large extent of global cirrus cloud coverage.

Fu et al. (1995) demonstrated that tropical convection can be enhanced through several radiative mechanisms. Cloud top cooling and cloud base heating act to prolong the lifetime of the cirrus anvils produced by convection, which in turn prolongs the effect that the cloud has on the radiation balance of the atmosphere. Destabilization of the cloud layer is due to cloud top cooling and cloud base heating. Clear sky radiative cooling by thermal emission to space also has the effect of destabilizing the atmosphere facilitating generation of tropical convective systems and tropical cirrus anvils.

Garrett et al. (2005) and Garrett et al. (2006c) showed that in addition to the widely accepted vertical motions of lifting and mixing (Ackerman et al., 1988; Lilly, 1988), radiative interactions can also drive horizontal motions in a stable environment if the heating is concentrated in a thin layer at the top and bottom of the anvil. In fact, if a thin tropopause layer of cirrus is located above the anvil, it can have a dramatic impact on the lifetime of underlying cirrus clouds. The anvil is exposed to a warmer body than the cold upper atmosphere and this reduces the temperature contrasts between anvil top and its environment. The result of this is that the horizontal motions discussed previously are lessened and the anvil spreads and thin more slowly than in the absence of thin tropopause cirrus.

Durran et al. (2009) used numerical simulations of thin tropopause layer cirrus to investigate their role in the radiation balance in the tropics. Their work concluded that a thin layer of tropopause cirrus can contribute significantly to the heating of the upper troposphere. Mesoscale circulations that result from this heating moderate the temperature rise of the cirrus cloud itself, as well as producing updraft velocities sufficient to overcome sedimentation, allowing longer persistence of the cirrus layer. The updraft created by the radiatively induced mesoscale circulations was also suggested as a possible mechanism for stratospheric dehydration in which the cloud ice particles are carried into the stratosphere, where they increase in size through diffusional growth. The stably stratified air in the stratosphere inhibits the mesoscale circulations that carried the cloud ice into the stratosphere, allowing for sedimentation. In conjunction, Dinh et al. (2010) demonstrated with numerical simulations that thin tropopause cirrus can be maintained through water vapor convergence that is driven by the mesoscale circulations. This work also confirmed that thin tropopause cirrus may play a role in stratospheric dehydration, not only in the vertical column containing the cloud due to vertical motions, but also due to horizontal motions as well.

Fusina and Spichtinger (2010) studied the role that radiative flux divergence plays in super-saturated clear sky regions. Their work found that in a narrow region of a parameter space in stability and relative humidity, radiative flux divergence in super-saturated regions of the troposphere can initiate cirrus cloud formation. This is achieved through radiative cooling destabilizing the air, enhancing the turbulent motions of the air to the point where they can overcome the inhibition to vertical motions imparted by the stably stratified air. Once this is overcome, the updrafts initiated by the radiative heating are sufficient to form cirrus clouds. Outside this narrow region of a parameter space in stability, the air is either too stable to form a cloud, or is too unstable for radiative flux divergence to play a role. Additionally, outside this narrow region of a parameter space in relative humidity, the air either has sufficient water vapor to spontaneously form a cloud, or insufficient vapor to form a cloud despite the effects of radiative flux divergence

Dobbie and Jonas (2001) conducted a numerical study on the effects of radiation in cirrus clouds. Their study showed that radiation plays an important role in shaping the the structure of cirrus clouds. This was done by forming an inhomogeneous cloud in their simulation and then allowing it to evolve with radiation turned on or off. The resulting clouds showed significant structural and circulation differences between the case with radiation and the one without it. Clouds allowed to evolve with the influence of radiation also were simulated to last longer than the corresponding cloud that was not exposed to thermal or solar radiation. They also determined that for thick clouds (~3km in depth), that thermal spectrum radiation, rather than solar, dominates the evolution of the structure of the simulated cirrus cloud.

1.1.3 Simplified Representations of Cloud Evolution

Dobbie and Jonas (2001) described a dimensionless radiative stability number

$$R_{sn} = \frac{(\partial\theta_v(z,t)/\partial z)}{-(\theta_v(z,t)/T_v)(\partial\mathcal{H}/\partial z)\delta t} \tag{1.2}$$

where θ_v is the virtual potential temperature, T_v is the virtual temperature, and $\mathcal{H}$ is the heating rate of the cloud. The radiative stability number R_{sn} gives the time scale δt for initiation of convective instability in clouds through radiative heating or cooling. This dimensionless number was used in their study to describe the generation of instability through a combination of several observable quantities such as potential temperature and the heating rate. The dimensionless number R_{sn}, when compared to model simulations, was found to predict the occurrence of instability, so long as the effects of latent heating were also accounted for.

However, one drawback of the Dobbie and Jonas (2001) study was that it was conducted in a 2D framework with no limits placed on the horizontal extent of the cloud. This had the effect of limiting the degrees of freedom available for cloud evolution, effectively restricting any horizontal expansion of the cloud.

One of the more pertinent studies on clouds and their life cycle, examined outflow dynamics of stably stratified nocturnal thunderstorm clouds in response to lower atmospheric evaporational cooling of precipitation (Raymond and Rotunno, 1989). Rather than directly calculating the dynamical forces that caused outflows, Raymond and Rotunno identified a parameter space of two dimensionless numbers

$$F = \frac{\mid U \mid}{(Qdl)^{1/3}} \tag{1.3}$$

$$G = \frac{\pi \mid U \mid}{Nd} \tag{1.4}$$

that could be used to describe atmospheric flows, where l and d are the length and depth of the region, U is the ambient wind speed, N is the Brunt-Vaisala frequency, and Q is the cooling rate expressed as a buoyancy depletion rate. They used these dimensionless numbers to map out a phase space that describes the cooling driven flow under idealized atmospheric conditions, as well as critical values for which the cooling driven flow that matched the wave propagation velocity and the material outflow velocity given by

$$F = F_c = F_0 \left[\frac{G^2}{G_o^2 + G^2} \right]^{1/3} \tag{1.5}$$

Numerical modeling was used to verify that the theoretical phase space would produce the appropriate evolution. As a result of this, Raymond and Rotunno were able to determine idealized conditions under which nocturnal convective systems could be self-sustaining, i.e. producing new convective cells ahead of currently established convective cells. They described a process where downdrafts from the existing convective cells create horizontal outflows at the surface. These outflows result in convergence and lift, which leads to the development of new convective cells.

The work by Raymond and Rotunno indicated that in idealized environments, it is possible to take a very complex dynamical system and reduce the governing equations of the system from a highly complex, nonlinear model into simple dimensionless numbers, and still retain predictive power. The work by Raymond and Rotunno also demonstrated that idealized modeling can be utilized to investigate very complicated systems to gain understanding of their basic workings, and even develop insight into important processes.

However, the work done by Raymond and Rotunno focused on the environment surrounding the cloud rather than the cloud itself. The dynamical motions of their simulations were driven by down-drafts caused by the evaporation of hydrometeors. They also did not address radiative processes. In principle, longwave radiation can produce significant heating rates at cloud base and cooling rates at cloud top (Ackerman et al., 1988), and this energy input could be sufficiently large to play a significant role, especially in cold stratiform clouds where latent heat effects are small (Heymsfield and Miloshevich, 1991).

1.2 Approach of This Thesis

Perhaps a more intuitive approach to the problem of cloud dynamic evolution is to start with an extremely idealized situation and build up complexity from there. In this thesis, rather than include complications such as precipitation and shear dynamics, we begin with a simple uniform cloud at rest such that the cloud evolution from an initial state is due solely to radiative interactions with cloud condensate - warming from the ground at cloud base, and cooling to space at cloud top.

In the development of the conceptual model presented in Chapter 2, this study considers the thermodynamic basis for cloud evolution. Radiative heating creates a potential energy difference in the cloud, and the cloud has multiple means to utilize the available potential energy provided through radiative interactions with cloud condensate: isentropic lifting (descent), convective mixing, or evaporation (condensation) of cloud water. These processes compete against each other to utilize the available, limited energy supplied to the cloud. While all processes can be expected at all times, some will be more efficient at utilizing the limited energy supply at any given moment. The most efficient process will dominate the cloud's evolutionary path, while the less efficient processes will have significantly smaller rates of occurrence.

There is a timescale associated with each evolutionary process. This timescale is determined by how rapidly the available potential energy can be used by a cloud, which is determined by the environmental parameters. The ratios of these timescales provide dimensionless numbers useful in describing how a cloud will evolve. These dimensionless numbers are derived such that they are evaluated at a particular isentrope in the atmosphere and at a particular time.

1.3 Thesis Outline

Chapter 2 outlines a theoretical framework for the study of radiatively driven evolution of cirrus clouds. Several dimensionless numbers will be derived and discussed. Chapter 3 describes the numerical model utilized to perform simulations of cirrus clouds. Chapter 4 describes the results of the simulations in detail and discusses the predictive ability of the dimensionless numbers, evaluated at the initialization of the simulations, for the simulated cloud evolution. Chapter 5 discusses a theory of mammatus formation and the simulations of mammatus clouds that stemmed from the work in Chapter 4. Chapter 6 will offer some conclusions and a discussion of the shortcomings of this study as well as work for the future.

CHAPTER 2

THEORETICAL DEVELOPMENT

Clouds are sometimes thought of as simple Carnot heat engines, performing work through the movement of heat from one warm reservoir to another, cooler reservoir(Emanuel and Bister, 1996). However, in the case of many cloud models that treat clouds as a heat engine, the cloud is treated as a steady-state system in which the rate of doing work is constant. Here, clouds will be treated as fully dynamic systems. Work performed by the cloud heat engine acts on the cloud itself, modifying the cloud heat engine and the work it performs.

In the case of cirrus anvils, radiative energy is transferred from the warm reservoir of the surface to a colder reservoir, either space or a higher, cooler portion of the atmosphere or cloud, through radiative transfer, convection, or isentropic lifting. As with any real heat engine, the thermal contrasts provides the energy available to the the cloud heat engine to do work. It is the deposition of energy through radiative flux divergence and convergence that both drives the heat engine of the cloud, as well as the evolution of the cloud through the work performed by the cloud heat engine.

This chapter will address the transfer of radiation from the surface through the lower troposphere to the cloud, the absorption of the radiation by the cloud and finally the dynamic flows generated by the influx of radiative energy into the cloud that govern the evolution of the cloud.

2.1 Radiative Transfer

All matter emits thermal spectrum radiation. This emission is governed by the Planck function

$$B(\lambda, T) = \frac{8\pi hc}{\lambda^5}\frac{1}{\exp(\frac{hc}{\lambda kT}) - 1} \tag{2.1}$$

which gives the relation between the energy density of emission as a function of wavelength λ and temperature of the emitting body T. Using a surface temperature of 28°C or 301K, Equation 2.1 gives the spectral energy density curve shown in Figure 2.1.

The flux of radiative energy is given by the Stefan-Boltzmann Law,

$$F = \sigma T^4 \tag{2.2}$$

which is the integral of equation 2.1 over the full hemisphere of emission angles and all wavelengths, and is dependent solely on the temperature of the emitting source. The radiative flux is equivalent to the radiation pressure of a photon gas, times the speed of light c. The Stefan-Boltzmann law assumes that the emitting object is a blackbody. If the emitting

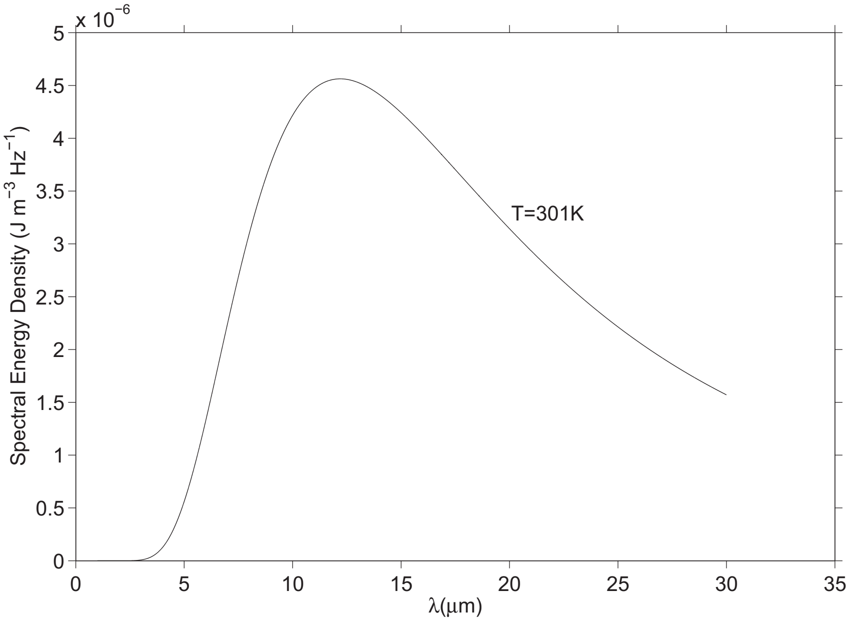

Figure 2.1: Spectral energy density plot of the Planck's Function for T=301K

object is not, then the flux of radiative energy becomes

$$F = \epsilon \sigma T^4 \tag{2.3}$$

Thermal spectrum radiation emitted from the surface passes through the atmosphere before interacting with cloud condensate. In this intervening layer of atmosphere, thermal spectrum radiation is attenuated by various greenhouse gases, including water vapor which will be the primary constituent of the lower troposphere that will be considered in this work.

For there to be interaction between the surface emitted radiation and the atmosphere, there must be something in the atmosphere that either absorbs or scatters in the peak wavelengths of the emission spectrum. While there is negligible scattering of thermal radiation by atmospheric constituents, water vapor is a strong absorber in the bands above 15μm due to the rotational bands of absorption.

However, objects that absorb radiation also emit radiation. The Schwartzchild equation,

$$\frac{dI}{ds} = \beta_a (B(T) - I) \tag{2.4}$$

describes succinctly how radiation passing through an absorbing medium changes its intensity. The atmosphere, being a graybody, does not absorb all radiation, but rather a fraction β_a. Using Kirchhoff's Law,

$$\epsilon_\lambda = a_\lambda \tag{2.5}$$

which states that the absorptivity of a material is equal to its emissivity, the change in intensity of radiation along a path of length s decreases due to absorption and increases due to emission. From Equations 2.3 and 2.5, it is possible to determine the flux of energy out of the atmosphere.

A simple layer model of the subcloud atmosphere, shown in Figure 2.2, is useful for vi-

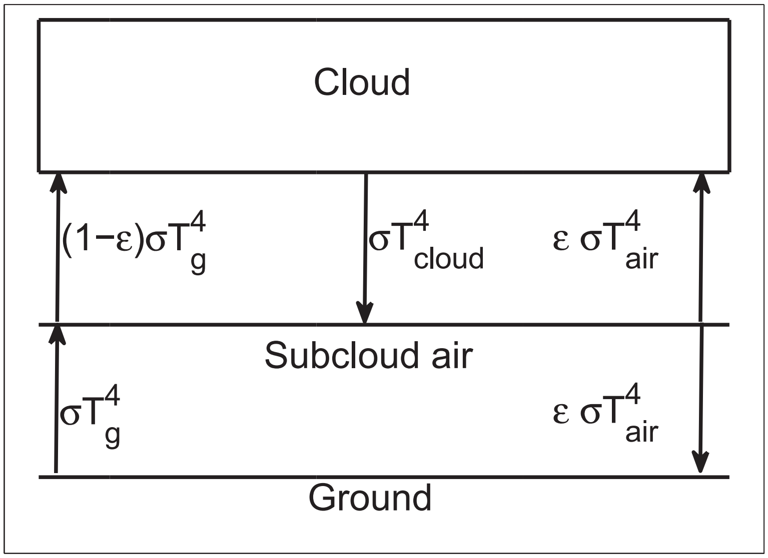

Figure 2.2: Simple layer model of the cloud-ground system

sualizing the radiative fluxes in the atmosphere. The emissivity of the atmosphere between the surface and the cloud controls the amount of radiative flux from the surface that reaches the cloud as well as the portion of incident flux on cloud base that comes from the cooler subcloud layer.

Figure 2.2 depicts only the subcloud atmosphere, and as such has no upward fluxes out of the top of the cloud or downward fluxes into the cloud. If it were to include these fluxes, the upward flux out of the cloud would be σT_{cloud}^4 and the downward flux into the cloud would be $\epsilon\sigma T_{stratosphere}^4$ from the layer of air between the cloud and space.

Net upward flux of thermal radiation at cloud base, based on the simple layer model in Figure 2.2, is given by

$$(1-\epsilon)\sigma T_g^4 + \epsilon\sigma T_{air}^4 - \sigma T_{cloud}^4 \tag{2.6}$$

Varying the water vapor, or any other greenhouse constituent, of the lower atmosphere will have the effect of changing the emissivity of the subcloud layer. The total flux of radiative energy is decreased by the presence of water vapor and other greenhouse constituents by both absorbing some of the stronger flux of energy from the surface, and re-emitting a less intense flux of radiation at cooler temperatures. Since water vapor in the atmosphere is emitting at a cooler temperature than the surface, increasing the amount of water vapor would have the effect of increasing the emissivity of the lower atmosphere and decreasing the intensity of radiation incident on the cloud.

There are two ways that govern how a change in the amount of a substance in the atmosphere changes how that substance absorbs radiation: strong-line and weak-line absorption (Petty, 2004). In the thermal spectrum, water vapor obeys the physics governing strong-line absorption. This means that at the fundamental absorption frequency, water vapor absorption is saturated, with zero transmittance. However, in a frequency band around the fundamental absorption frequency, where the absorption is not fully saturated, the amount of radiation absorbed by water vapor in that frequency band is determined by the square root of the density of water, rather than linearly in the case of weak-line absorption (Petty, 2004). Given this, the energy that the ground supplies to cloud base, essentially, the transmittance through the subcloud layer of atmosphere, should increase proportionately to the square root of the decrease in water vapor.

The cloud heat engine is defined by the temperature contrast between the upper troposphere in which the cloud resides and the lower atmosphere and surface (Figure 2.3).

The temperature contrast $\Delta\tilde{T}$ is defined as

$$\Delta\tilde{T} = \tilde{T}_{cloud} - \tilde{T}_{air} \tag{2.7}$$

where, from the simple layer model of the atmosphere in Figure 2.2,

$$\tilde{T}^4_{air} = T^4_g + \varepsilon_{air}(T^4_{air} - T^4_g) \tag{2.8}$$

where ε_{air} is emissivity of the atmosphere. $\tilde{T}_c$ is effectively T_c, the temperature at cloud

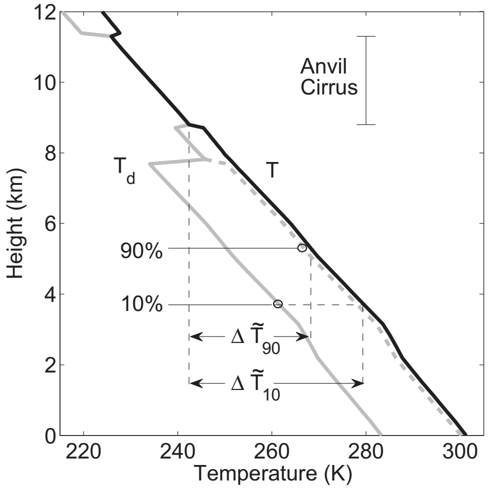

Figure 2.3: Dew point temperature and temperature profiles for a dry (10% RH) and a moist (90% RH) lower troposphere. The effective brightness temperature of the lower troposphere is indicated and $\Delta\tilde{T}$ represents the brightness temperature contrast that drive the cloud heat engine.

base due to kinetic motions. Using equation 2.7, equation 2.8 and the fact that temperatures decrease with increasing height, the temperature differential that drives the heat engine can be increased by increasing the height of the cloud, increasing the surface temperature or decreasing the emissivity of the intervening atmosphere.

Thermal emission from a black body is $F = \sigma\tilde{T}^4$ according to equation 2.2. The fourth power relation is a consequence of the emission being proportional to the radiation pressure, which is one third of the photon internal energy density (Zemanksy and Dittman, 1997). If $\Delta\tilde{T} = |\tilde{T}_c - \tilde{T}_a| \ll \tilde{T}_c$, then the flux of energy into the cloud is given by

$$\Delta F_{net} \simeq 4\sigma\tilde{T}_c^3\Delta\tilde{T} \tag{2.9}$$

which is an equivalent expression for the speed of light c times the local gradient in photon pressure. It is this gradient in photon pressure that drives energetic flows into the colder cloud.

2.2 Radiative Interaction with Condensed Matter

Condensed water in the atmosphere interacts strongly with radiation in the thermal spectrum. Reflection of radiation in this spectrum by cloudy air is minimal and can be ignored for the sake of simplicity. The heating rate of cloudy air due to local radiative flux divergence is given by

$$\mathcal{H} = \frac{dT}{dt} = -\frac{1}{\rho c_p}\frac{dF^{net}}{dz} \tag{2.10}$$

where θ is the potential temperature of the air, ρ is the density of the air, c_p is the specific heat of dry air at constant pressure, and F^{net} is the net radiative flux. The emissivity, and consequently the absorptivity of condensed water (in the case of cirrus clouds, condensed water takes the form of ice particles) increases with depth into the cloud δz (Petty, 2004) such that

$$\varepsilon(\delta z) = 1 - \exp(-\gamma k(r_{ice}) q_i \rho_{air} \delta z) \tag{2.11}$$

where γ is a diffusivity factor required to adjust isotropic thermal radiation to a 1-D flux framework. Its value is ~1.6. The absorption coefficient $k(r_e)$ is a function of the radius of the cloud ice crystals. The ice water mixing ratio q_i is given in units of kg of ice water per kg of air and ρ_{air} is the density of the air in which the ice water is contained. Emissivity and absorptivity are defined as the ratio between the actual emission and absorption of radiation of an object and the blackbody emission and absorption. Equation 2.11 describes how the emissivity of a cloud layer approaches that of a blackbody as the layer depth δz increases, the layer contains more ice water, or the diffusion of radiation in the layer increases.

This implies that the radiation can only penetrate a specific depth into the cloud before it is attenuated. This is the source of the radiative flux divergence in equation 2.10. As such the heating (or cooling) of the cloud is confined to a layer extending from the base (or top) of the cloud to a specific depth into the cloud. That depth is given by the characteristic scale of the decrease in emissivity such that Equation 2.11 is given by

$$\epsilon = (1 - e^{-1}) \tag{2.12}$$

yielding an e-folding depth into the cloud of

$$h = \frac{1}{\gamma k(r_e) q_i \rho_{air}} \tag{2.13}$$

and

$$\epsilon = 1 - \exp(-\delta z/h) \tag{2.14}$$

2.3 Thermodynamic Response

For a system at constant temperature and pressure, or equivalently for a system on an isentropic surface θ, such as the cloud system modeled in this work, energy deposited into the system through radiative flux divergence will increase the enthalpy H of the system where

$$H = U + PV \tag{2.15}$$

and U is the internal energy and PV is the pressure times the volume. Energy deposited into the cloud system can either increase the internal energy or increase the pressure or volume.

The first law of thermodynamics (Salby, 1996; Rogers and Yau, 1989; Kittel and Kroemer, 1998)

$$dU = \delta Q - PdV \tag{2.16}$$

written in terms of enthalpy becomes

$$dH = \delta Q + VdP \tag{2.17}$$

However, it it useful to add the implications of the second law of thermodynamics to express enthalpy in terms of the Gibbs free energy

$$G = H - TS \tag{2.18}$$

and

$$dG = dH - TdS \tag{2.19}$$

This can alternatively be expressed as

$$dH = dG + TdS \tag{2.20}$$

and if no work is done by the system,

$$dH = dG + dU \tag{2.21}$$

and dividing by volume to express in energy densities

$$dh = dg + du \tag{2.22}$$

Effectively, equation 2.22 states that the increase in enthalpy due to radiation will be partitioned between increasing the Gibbs potential of the system and increasing its internal energy. Also, since $dh = dp + du$, we can state that $dg = dp$ in this case. The ratio of this partitioning can be obtained from the 1st law of thermodynamics recognizing that

$$h = \rho c_p T \tag{2.23}$$

$$u = \rho c_v T \tag{2.24}$$

$$p = \rho R T \tag{2.25}$$

and dividing by temperature and density (Salby, 1996),

$$c_p = R + c_v \tag{2.26}$$

where c_p is the specific heat at constant pressure, c_v is the specific heat at constant volume, and R is the gas constant for air. Thus the time rate of change for enthalpy density can be expressed as

$$\frac{dh}{dt} = \rho c_p \frac{dT}{dt} \tag{2.27}$$

and for the Gibbs potential as

$$\frac{dg}{dt} = \rho \frac{R}{c_p} \frac{dT}{dt} \tag{2.28}$$

The Gibbs free energy of a system is at a minimum when a system is at equilibrium and any work done by a system at disequilibrium will move the Gibbs free energy to a lower value and back toward equilibrium. The enthalpy of a system exposed to a potential energy density difference will adjust over time. If that adjustment is done through radiative transfer, the time evolution will be

$$\frac{dh}{dt} = \rho c_p \frac{dT}{dt} = -\frac{dF^{net}}{dz} \tag{2.29}$$

which relates the heating rate (dT/dt) to the convergence of radiation flux through a layer in the system (dF^{net}/dz). Radiative flux F is a measurement of the energy contained in the radiation passing through a plane in a specified time. If the net flux F^{net}, the combination of upward and downward fluxes, changes with respect to height, the energy must be deposited in the medium that the flux passes through. This deposition of energy is then converted into an increase in temperature based upon the heat capacity of the medium and the density of that medium.

With respect to a microphysically homogeneous cloud, i.e., a cloud composed of identical cloud particles, initially at rest within an environment with no thermal or solar radiation, there will be no motions as the cloud is in gravitational equilibrium with its surrounding environment (Figure 2.4).

Now, suppose thermal radiation is turned on. At that instant, the cloud will become exposed to a gradient in potential energy due to thermal temperature contrasts, and consequently photon pressure, between the surface and the cloud.

Naturally, this gradient of energy density drives a flow of radiative energy into the cloud system, which is initially at equilibrium, increasing the Gibbs energy density by some amount Δg_{rad}, as shown in Figure 2.5.

The size of the perturbation Δg_{rad} is proportional to the flux of radiative energy into the system due to the gradient in photon pressure. Thus, the increase in Gibbs free energy density in time δt is given by

$$g(t+\delta t) \mid_{\theta} = g_{eq} \mid_{\theta} + \Delta g \mid_{\theta} \tag{2.30}$$

and

$$\Delta g \mid_{\theta} = \frac{\mid \Delta F \mid_{\theta} \mid A \delta t}{V} \frac{R}{c_p} \tag{2.31}$$

where ΔF is the net flux divergence across the cloud and A is the area of the cloud. Equa-

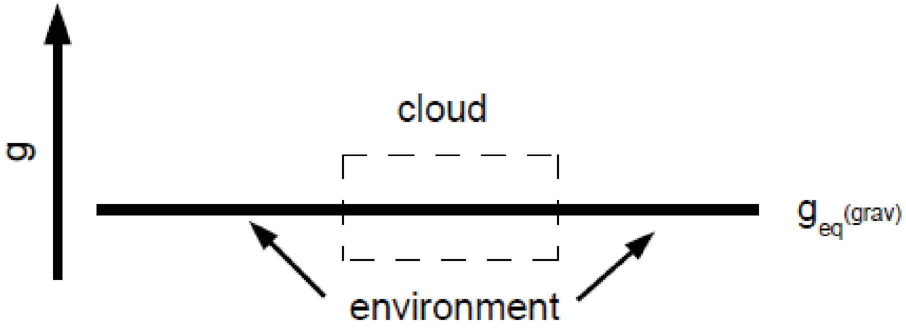

Figure 2.4: A conceptual sketch of a cloud in gravitational equilibrium with its surroundings

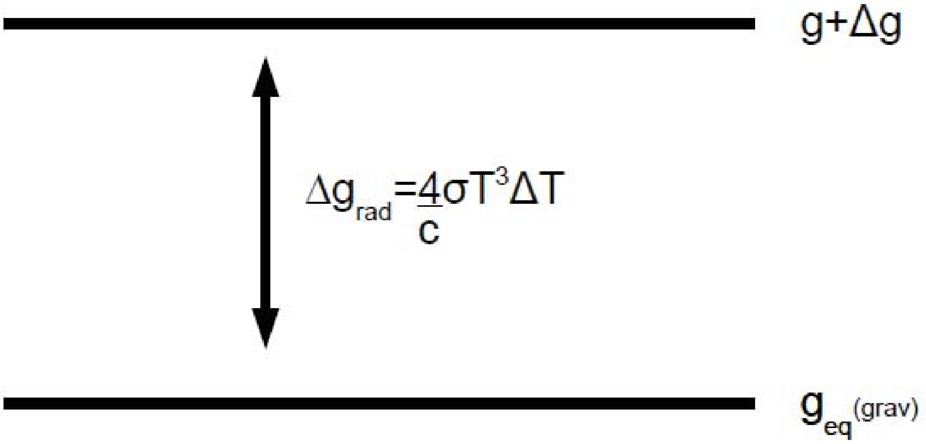

Figure 2.5: A conceptual sketch of a cloud exposed to a higher potential surface through radiative heating

tion 2.31 can be converted into a differential

$$\frac{d\Delta g}{dt}\mid_{\theta}=\frac{\mid \Delta F\mid_{\theta} A}{V}\frac{R}{c_p} \tag{2.32}$$

where V is the volume of the cloud affected by the flow of radiative energy and $V = Ah$ where h is the depth to which radiation penetrates into the cloud. The local rate of increase in the Gibbs energy density is

$$\frac{dg}{dt} = -\frac{R}{c_p}\frac{\partial F^{net}}{\partial z} \tag{2.33}$$

which is the divergence of enthalpy in the cloud layer modified by the fractional portion of enthalpy that is available to do work R/c_p, according to the relation in equation 2.26. The flow of energy into the cloud system is due to a contrast in g, as shown in Figure 2.6.

At the cold temperatures of cirrus anvils studied in this work, virtually all of the deposited energy is converted into heating of the cloud with a negligible amount used to change the phase of the cloud condensate, which would reduce the temperature contrast created by the flux deposition (Heymsfield and Miloshevich (1991)). The flux deposition

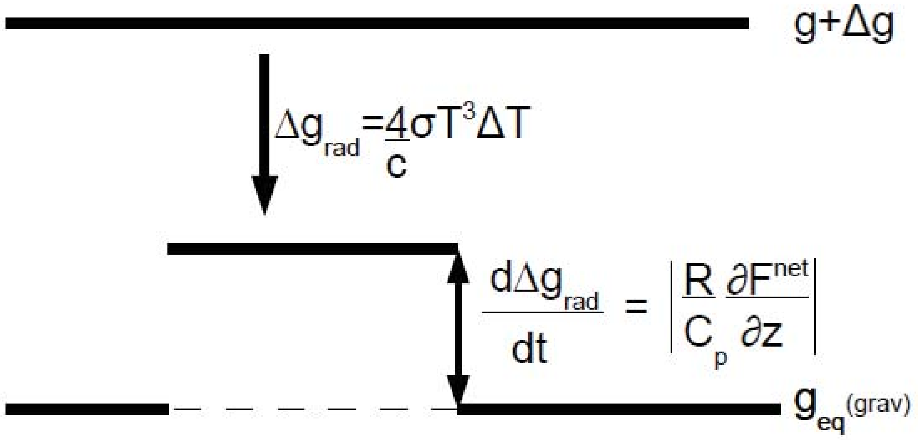

Figure 2.6: A conceptual sketch of a cloud perturbed from equilibrium by radiative transfer from a higher potential surface

creates a temperature contrast as described earlier according to

$$\mid \Delta F \mid_{\theta} = \mid F^{\uparrow} - F^{\downarrow} \mid_{\theta} \backsimeq 4\sigma T_c^3 \Delta T \tag{2.34}$$

where T_c is the temperature of the cloud.

As the cloud system is perturbed to a higher potential due to radiative energy deposition, the system is no longer in equilibrium with its environment. The excess potential Δg is therefore available to do work. This work is what allows the cloud system to evolve over time, moving back towards equilibrium, as is required by the 2nd law of thermodynamics. The system will evolve towards lower potential and higher entropy.

The rate at which the system moves back towards equilibrium is related to the potential contrast Δg between the new perturbed potential of the cloud system and the equilibrium potential of the surrounding environment g_{eq}. The cloud will relax back to equilibrium from perturbation, as shown in Figure 2.7. The factor of α is a relaxation timescale for the cloud system to use the available potential supplied by the perturbation Δg and return to equilibrium with the surrounding environment at a potential level of g_{eq}.

To more clearly demonstrate that α represents a relaxation time scale, consider the per-

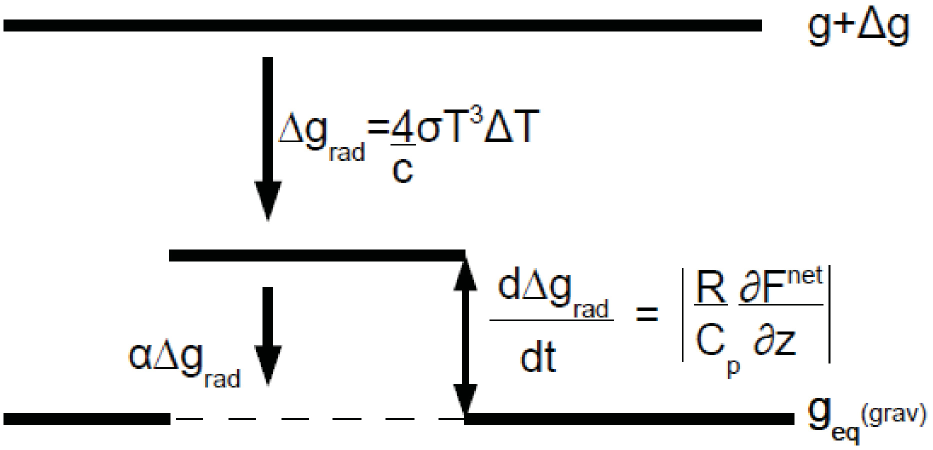

Figure 2.7: A conceptual sketch of a cloud system exposed to a higher potential surface by radiative heating

turbed cloud system if the radiative transfer of energy to/from the lower/higher potential surface is stopped. At this point, there is no new energy deposition into the cloud system, only available potential to do work given by Δg. To return to equilibrium, all of the potential energy Δg must be converted either into kinetic energy by driving dynamic motions, or through phase changes. The time evolution of the system can be written as

$$\frac{d\Delta g}{dt} = -\alpha \Delta g \tag{2.35}$$

the solution to which is

$$\Delta g(t) = \Delta g_0 \exp(-\alpha t) \tag{2.36}$$

Thus, $1/\alpha$ is the e-folding time scale for restoring equilibrium in potential energy density.

However, it is still possible for the cloud to be in a dynamic equilibrium, or rather have an equilibrium rate of evolution while exposed to the higher potential surface of the ground. If the energy input into the cloud system through radiative flux divergence exactly equals the energy being converted from potential energy into kinetic energy through cloud evolution processes described later on in this chapter, then the cloud system would maintain equilibrium.

$$\frac{d\Delta g}{dt} = \frac{R}{c_p}\frac{\partial F^{net}}{\partial z} - \alpha\Delta g = 0 \tag{2.37}$$

$$\frac{R}{c_p}\frac{\partial F^{net}}{\partial z} = \alpha\Delta g \tag{2.38}$$

2.3.1 Equipartition

A perturbation in potential energy density of a system Δg away from some equilibrium will be distributed through the available modes of evolution of the system, otherwise referred to as the degrees of freedom of the system, such that

$$\Delta g = \Delta g_i = \sum_i n_i \Delta\mu_i \tag{2.39}$$

These degrees of freedom are the ways in which the energy can be used (Kittel and Kroemer, 1998), also referred to later in this text as the individual orthogonal modes of evolution. In equation 2.39, n_i is the number density of the particular degree of freedom and $\Delta\mu_i$ is the specific potential to which matter must be raised to exist in that degree of freedom. This potential $\Delta\mu_i$ is defined as

$$\mu_i = \frac{dg_i}{dn_j}\ |_{i\neq j} \tag{2.40}$$

which means that there are two ways of adjusting the potential $\Delta\mu$, either through changing the Gibbs free energy associated with the potential level, or by changing the number density of the particular matter occupying that potential level.

$$d\ln\Delta g_i = d\ln n_i + d\ln\mu_i \tag{2.41}$$

Equipartition theory (Kittel and Kroemer, 1998), requires that the energy Δg be distributed across the individual modes Δg_i such that $n_i\Delta\mu_i = n_j\Delta\mu_j$. This means that the potential energy density is spread evenly across the system based on number density in each degree of freedom. If the potential energy density were not distributed in such a manner, there would be potential energy gradients when comparing degrees of freedom and potential energy density would flow from a higher potential energy density to a lower one, equilibrating the potential energy density levels.

As energy flows in for a quasi-equilibrium system, all energy levels will rise equally as required from the previous argument. According to this,

$$\frac{d(n_i \Delta\mu_i)}{dt} = \frac{d(n_j \Delta\mu_j)}{dt} \tag{2.42}$$

which can be discretized to

$$\frac{\Delta(n_i \Delta\mu_i)}{\tau_i} = \frac{\Delta(n_j \Delta\mu_j)}{\tau_j} \tag{2.43}$$

where τ is the timescale for the change to occur. Combining equations 2.43 and 2.38 yields

$$\alpha\Delta g = \sum_i \alpha_i \Delta g_i = \sum_i \frac{\Delta g_i}{\tau_i} \tag{2.44}$$

2.4 Specific Modes

The individual modes to which the imparted potential energy density Δg must be distributed are required by equipartition theory to be orthogonal modes. This requires that energy distributed to one degree of freedom becomes unavailable for another degree of freedom. Likewise, the characteristic means for which each degree of freedom to utilize the potential energy density supplied to it and relax back towards some equilibrium state, or mode of evolution, must also be orthogonal.

When considering a cirrus cloud, there are several degrees of freedom to which any potential energy density may be distributed. For example, as the potential energy density flows into the base of the cloud through radiative transfer from the ground and intervening atmosphere, several things can happen. The cloud base can be uniformly lifted to a higher potential temperature, or isentrope. This degree of freedom will be referred to as isentropic adjustment, due to the fact that the isentropic surfaces adjust in height. Alternatively, the cloud base can become convectively unstable and form a mixed-layer. This degree of freedom will be referred to as mixing. The third and final degree of freedom available to a cirrus cloud is evaporation/condensation. Horizontal motions, or spreading of cloud base are not considered an individual degree of freedom since, they do not form an orthogonal degree of freedom. These horizontal motions are simply a consequence of the circulations induced by both isentropic adjustment and mixing. As such, they are neither their own mode of cloud evolution nor solely a consequence of an individual mode. These three degrees of freedom and their associated modes of evolution will be discussed in depth in this section.

One might imagine that a purely radiative equilibrium could occur as an evolutionary mode. However, this could only occur when there is no temperature gradient between the cloud base and the lower troposphere (or cloud top and the stratosphere). Any temperature gradient will lead to a heating of the cloud. This heating will either result in a phase change of the cloud condensate or a density difference between the cloud and the surrounding air, either vertically or horizontally, which will drive dynamic motions.

The thermodynamic system of the cloud can now be defined. The cloud, initially at rest, has a width L and a height ΔZ with a volume $V \simeq L^2 \Delta Z$. Alternatively, one could define the thermodynamic system in radial coordinates with a radius r and height ΔZ and volume $\pi r^2 \Delta Z$. The choice of coordinate system is purely mathematical and has no bearing on the physical thermodynamical system. For ease of conceptual formulation, however, this text will be constrained to Cartesian coordinates.

There is also a layer of depth h into the cloud into which the radiative energy is deposited. The energy deposited into this layer of depth h is instantly mixed throughout a layer of constant potential energy density Δg. Initially, the depth to which that deposited energy is mixed δz, is equal to the characteristic penetration depth h, given by equation

2.13. However, the layer into which the deposited radiative energy is mixed will deepen as time progresses. A diagram of the initial cloud system is provided in Figure 2.8. The thermodynamic cloud system is defined by the depth of the layer δz with a constant potential energy density Δg.

2.4.1 Dynamic Response

The deposited radiative energy is spread throughout a mixed-layer of depth δz now larger than or equal to the radiation penetration depth h. This distribution of energy results in a homogeneous increase in the energy density of the layer δz, which increases at the rate

$$\frac{d\Delta g}{dt} = -\frac{R}{c_p}\frac{\Delta F^{net}}{\delta z} \tag{2.45}$$

The increase Δg is given by the product of the density of air in the mixed-layer, $\rho = m_{air}/(\delta z L^2)$ where m_{air} is the mass of air in the layer δz, and the gravitational potential

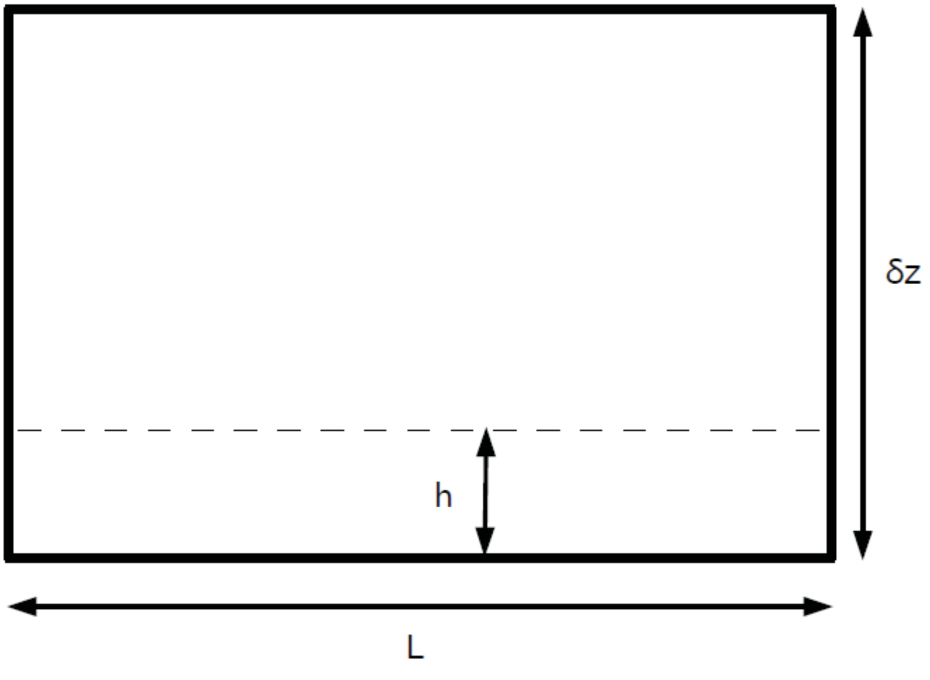

Figure 2.8: The initial thermodynamic cloud system. The section of the cloud shown here illustrates the radiative absorption depth h, and the deeper mixed-layer through which that energy is distributed δz

that can be used to drive turbulent motions, ΔG. Thus,

$$\Delta G = \frac{1}{2}\rho N^2 \delta z^2 \tag{2.46}$$

where $\frac{1}{2}\rho N^2 \delta z^2$ is the energy required to move against stratification, effectively the potential energy of a harmonic oscillator (Wallace and Hobbs, 2006). In order to develop a mixed-layer, it is necessary to overcome the potential difference between the top and bottom of the layer of depth δz so that there is no longer an impediment to vertical motions. As such, it is necessary to equalize the potential difference between the top and bottom of the mixed-layer. The energy required to equalize this potential difference is given by equation 2.46. Once the potential difference is eroded, there is no energy barrier to vertical mixing.

The time evolution of Δg can proceed in either of two ways. It can result from a change in the potential ΔG, or through a change in the density of material that exists at the given potential.

$$\frac{d \ln \Delta g}{dt} = \frac{\partial \ln \Delta G}{\partial t} |_{\rho} + \frac{\partial \ln \rho}{\partial t} |_{\Delta G} \tag{2.47}$$

Since

$$\Delta G \sim N^2 \delta z^2 \tag{2.48}$$

and

$$\rho = \frac{m}{V} \sim \frac{m}{L^2 \delta z} \tag{2.49}$$

and assuming that m is fixed (i.e., little or no entrainment of mass across the mixed-layer's vertical boundaries, equation 2.47 can be rewritten as

$$\frac{d \ln \Delta g}{dt} = 2\frac{\partial \ln \delta z}{\partial t} |_{L} - 2\frac{\partial \ln L}{\partial t} |_{\delta z} \tag{2.50}$$

Equation 2.50 has several implications. If the width of the cloud L is held constant, radiative heating will increase the potential energy density by deepening the mixed-layer over time with a rate of deepening given by

$$w_{strat} = \frac{d(\delta z)}{dt} = \frac{d\theta}{dt}\frac{d(\delta z)}{d\theta} = \frac{\mathcal{H}g}{(\theta N^2)} \tag{2.51}$$

Alternatively, with the height of the mixed-layer held fixed, the potential energy will decrease as the mixed-layer expands horizontally by spreading along constant potential surfaces (i.e., isentropes) into the lower potential energy environment surrounding the initial cloud system boundaries. This occurs due to the fact that in a mixed-layer surrounded by a stably stratified atmosphere, a horizontal density gradient develops that drives outflow Garrett et al. (2005). At the top of the mixed layer, the cloudy air will be more dense than the surrounding air driving the outward flows.

This density current outflow occurs at a speed

$$u_{mix} = \frac{dL}{dt} \sim N\delta z \tag{2.52}$$

which results from the conversion of the gravitational potential energy $\sim N^2\delta z^2$ into kinetic energy, where the kinetic energy of motion is $\sim u_{mix}^2$. With these characteristic speeds of motion, equation 2.50 can be rewritten as a difference between the rate of increase in potential energy density due to radiative heating (α_{strat}) and the rate of loss of potential energy density due to horizontal mixed-layer spreading (α_{mix})

$$\frac{d\ln\Delta g}{dt} = \alpha_{strat} - \alpha_{mix} = 2\frac{w_{strat}}{\delta z} - 2\frac{u_{mix}}{L} \tag{2.53}$$

Should the two rates

$$\alpha_{strat} = \frac{g\mathcal{H}}{\theta N^2 h} \tag{2.54}$$

and

$$\alpha_{mix} = \frac{Nh}{L} \tag{2.55}$$

be equal, equilibrium in terms of potential energy density is maintained. However, this does not imply that there is no motion or evolution of the cloud. The increase of potential energy density from radiative heating is balanced by a loss of potential energy density from outward density currents. The result of which would be for isentropic surfaces, which were initially flat, to remain flat as the cloud spreads horizontally.

The two rates α_{strat} and α_{mix} presented above suggest that there may be dimensionless "Spreading Number" as suggested by Garrett et al. (2005) that is a ratio of the two rates

$$S = \frac{\alpha_{strat}}{\alpha_{mix}} = \frac{g\mathcal{H}L}{\theta N^3 h} \tag{2.56}$$

where S is evaluated for the cloud initially at rest where $\delta z = h$. For values of $S > 1$, the rate at which the mixed-layer deepens is too fast for the horizontal spreading to sufficiently compensate. In this case, radiative heating will drive the formation of a turbulent mixed-layer which will spread outward from cloud base as a density current. However, for values of $S < 1$, radiative heating will drive laminar outflows from cloud base that maintain flat isentropic surfaces.

Likewise, the same processes occur at cloud top, with radiative cooling driving outward spreading, either through laminar flows or through density currents. The spreading type is determined by the same "Spreading Number" S evaluated at cloud top.

As the cloud evolves over time, the spreading number S will also evolve since

$$S(t) = \frac{g\mathcal{H}(t)L(t)}{N^3(t)\theta(t)\delta z(t)} \tag{2.57}$$

The time dependence of these four variables requires that S is also a function of time. For example, the heating rate of the cloud can change based on formation or loss of cloud condensate, or the lower atmosphere cooling. The mixed-layer in which radiative energy is distributed can deepen over time. The cloud can spread, changing the value of L. The temperature of the air at cloud base can change as it is radiatively heated, which in turn affects the stratification of the atmosphere. However, this time evolution of the "Spreading Number" S will not be considered in this work.

2.4.2 Microphysical Response

Alternatively, in lieu of creation of a mixed-layer, the heating of the layer δz may result in microphysical changes in the cloud condensate. Like the deepening of the mixed-layer, the conversion of cloud ice to vapor due to heating also increases the potential energy density of the layer, and is compensated by a loss of potential energy density out the sides of the system due to spreading.

The saturation of a parcel of air, and consequently the amount of condensed water contained in that parcel, is related to its temperature through the Clausius-Clapeyron equation

$$\frac{d\ln e}{d\ln T} = \frac{L_s}{R_v T} \tag{2.58}$$

where e is the saturation vapor pressure of the parcel at temperature T, R_v is the gas constant for water vapor, and L_s is the latent heat of sublimation (Salby, 1996). Since this work deals exclusively with condensed water in the form of ice, L_s is used as the appropriate latent heat, and e is the saturation vapor pressure with respect to an ice surface.

There are two competing energies to consider when it comes to heating and cooling a parcel towards either higher or lower saturation. Saturation is the relevant value to consider since saturation is restored, if possible, through either the conversion of vapor to condensed mater, or vice versa. The first energy to consider is the heat energy deposited or lost through radiation. The enthalpy density of the parcel H will change from heating of the parcel in a given time Δt through the relation $\Delta H_{rad} = m_{air} c_p \mathcal{H} \Delta t$. Thus the energy change is dependent on the radiative flux convergence through the parcel according to equation 2.29, as well as the mass of water that is heated/cooled through that interaction.

The second form of energy that needs to be considered is the latent heat absorbed or released due to a phase change of matter. If the parcel becomes subsaturated, condensed matter will be repartitioned into the vapor phase, cooling the parcel, which in turn also helps to restore saturation. Conversely, if the parcel is super-saturated, vapor will condense into the solid phase (the liquid phase is excluded from the model for simplicity), heating the parcel, which also drives the parcel back towards saturation. Thus the latent heat release is $\Delta H_{lat} = m_{air} L_s \frac{dq_i}{dt} \Delta t$.

From the perspective of the saturation adjustment scheme of the model that will be used in this study (discussed in Chapter 3), it is perhaps more appropriate to consider ΔH_{lat} as $m_{air} L_s q_i$. In the model, if air is subsaturated, the saturation adjustment scheme will entirely and instantaneously evaporate the mass of condensed water required to restore saturation if there is enough condensed water to do so.

The ratio of these two enthalpy terms gives

$$\frac{\Delta H_{rad}}{\Delta H_{lat}} = \frac{c_p \mathcal{H} \Delta t}{L_s q_i} \tag{2.59}$$

which when expressed in terms of an evaporation rate due to radiative heating gives

$$\alpha_{evap} = \frac{1}{\tau_{evap}} = \frac{c_p \mathcal{H}}{L_s q_i} \tag{2.60}$$

The ratio of α_{evap} to α_{strat} (Equation 2.54) gives the “Evaporation Number”, a dimensionless ratio between the rate of evaporation in the heated layer and the spreading of that layer

$$E = \frac{\alpha_{evap}}{\alpha_{strat}} = \frac{c_p \theta N^2 h}{g L_s q_i} \tag{2.61}$$

This number, like the “Spreading Number” can also evolve over time, or more precisely

$$E(t) = \frac{c_p \theta(t) N^2(t) h(t)}{g L_s q_i(t)} \tag{2.62}$$

For values of $E > 1$, heating at cloud base will drive evaporation that destroys cloud condensate by converting it into water vapor to help saturate the now warmer air with a higher saturation vapor pressure. However, for values of $E < 1$, heating at cloud base will drive vertical motions more quickly than evaporation. It is important to note here that the "Evaporation Number" should only be considered if the "Spreading Number" has values of $S < 1$. Should this condition not hold and $S > 1$, a convective mixed-layer will develop. With a mixed-layer developing, there is the continual reformation of cloud condensate as part of the localized circulations in the mixed-layer. The mixed-layer circulations extend throughout the mixed-layer, but also below cloud base. As the subcloud air is lifted, it cools adiabatically and reaches saturation, forming new cloud condensate. This has the effect of counteracting the effect of radiative heating on the mixed-layer in terms of evaporation. The time scale for the creation of cloud through the mixed-layer circulations is much faster than the time scale for evaporation through radiative heating.

2.4.3 Precipitation

It is important to note that precipitation also plays an important role in the evolution of cirrus clouds. While precipitation processes have been excluded from this idealized model for the purpose of understanding radiative processes in isolation of other cloud processes, certainly natural clouds have significant precipitation rates.

To obtain the characteristic precipitation timescale for the modeled cloud α_{precip}, it is necessary to know both a characteristic precipitation rate P as well as the ice water content IWC in a vertical column of air as it is the ratio of these two quantities that determines the precipitation timescale (Garrett et al., 2006a). A characteristic precipitation rate for a cirrus anvil in Florida, measured by aircraft during the TWP-ICE field campaign, is 0.05 g m^{-3} h^{-1} with a maximum value of IWC of 0.3 g m^{-3} (Garrett et al., 2005).

The ice water content is given by

$$IWC = \rho_{air} q_i \tag{2.63}$$

where ρ_{air} is the density of air and q_i is the mass mixing ratio of condensed ice water in the air.

Given this,

$$\alpha_{precip} = \frac{P}{IWC} \tag{2.64}$$

Evaluation of this number, using observed values from CRYSTAL-FACE (Garrett et al., 2005), results in

$$\alpha_{precip} = \frac{0.05\frac{g}{m^3 h}}{0.3\frac{g}{m^3}} \simeq 0.15h^{-1} \simeq 4 \times 10^{-5}s^{-1} \tag{2.65}$$

Comparatively from tables 3.3 and 3.4 using values for the thickest modeled clouds ($q_i = 1g/kg$, $L = 10km$),

$$\alpha_{mix} = \frac{Nh}{L} \simeq 3 \times 10^{-5}s^{-1} \tag{2.66}$$

and

$$\alpha_{strat} = \frac{\mathcal{H}g}{\theta N^2 h} \simeq 0.04 \tag{2.67}$$

showing that precipitation depletes cloud condensate at at comparable rate to radiatively driven cloud evolution. The anvil will spread in a few hours and precipitate in about half of a day in the highest IWC cases. Precipitation is neither more nor less important of a cloud evolution process than the other processes discussed in this study. It is important to note that the measured value of IWC from CRYSTAL-FACE is of comparable magnitude to the highest mixing ratio clouds simulated in this study. It is also assumed that precipitation rates scale approximately linearly with IWC.

CHAPTER 3

MODEL AND SIMULATIONS DESCRIPTION

3.1 Model

Simulations of cloud evolution were performed using the University of Utah Large Eddy Simulation Model (UU LESM) (Zulauf, 2001). We use a LES model because the resolved scales in LES models are small enough to properly model the dynamic motions observed in clouds. These dynamics include turbulent motions, convection, entrainment and mixing, and other cloud scale motions.

The UU LESM uses a set of fully prognostic 3D non-hydrostatic primitive equations, utilizing the quasi-compressible approximation (Zulauf, 2001) where the speed of sound has been reduced to 50 m s^{-1}. The speed of sound was reduced in order to damp out the propagation of fast moving sound waves that are generated in the model due to the prognostic equations, as they are unimportant for atmospheric phenomenon. The damping of sound waves in this fashion has been found to be computationally sound while maintaining the accuracy of the simulation results (Droegemeier and Wilhelmson, 1987). Radiation transfer code was included in the model setup, but solar radiation was turned off. The model domain was placed at the equator, $\phi = 0°$, to eliminate any Coriolis effects. Even in the largest domain simulations, the maximum departure from the equator (50km) is sufficiently small as to justify not including the Coriolis effect in the model calculations.

Other features of the UU LESM include a second order Runge-Kutta time-splitting scheme where the evolution of model variables are calculated forward in time using several sub-timestep calculations. Traditionally, Runge-Kutta schemes use a half timestep($\Delta t/2$)

to calculate the values at time $t + \Delta t$. The Runge-Kutta time-splitting scheme used in the UU LESM uses several time steps between t, $\Delta t/2$, and $t + \Delta t$. For example, to calculate a timestep forward of $\Delta t = 1s$, the time-splitting scheme might use timesteps of 0.1 s in order to calculate the model variable values at t, $\Delta t/2$, and $t + \Delta t$. Spatial evolution is handled in the UU LESM by a third order upwind advection scheme for momentum, a second order monotonic advection scheme for scalar quantities, and a second order centered finite difference scheme for other terms (Zulauf, 2001). Subgrid scale turbulent kinetic energy closure is performed according to Deardorff (1980), with the buoyancy and dissipation terms in the turbulent kinetic energy prognostic equation handled using a backwards time step scheme (Zulauf, 2001).

3.2 General Setup

For all cases in this study, a periodic domain was used. The horizontal extent was chosen to be large enough to contain the initialized cloud as well as allowing sufficient space for spreading of the cloud during the model run. The horizontal extent of the domain is important to consider due to the periodic boundary conditions in the UU LESM model. Fluxes through one side of the domain (moisture, cloud ice, turbulent fluxes, etc.) enter back into the model domain from the opposite side. Thus it is necessary to select a model domain sufficiently large that no effects from one edge of the simulated cloud “wrap around” to the opposite side of the cloud. As such, horizontal domain size is case dependent. Horizontal grid size was chosen to be 30 m to match the minimum value for vertical penetration depth of radiation into the cloud, as determined by equation (2.13). As radiation passes through the cloud, it is attenuated by interaction with the cloud condensate and its intensity falls off exponentially. The depth to which the radiation penetrates is the length which is required to fully attenuate the radiation. This is the depth h referenced in Figure 2.8. Radiation penetration depth is dependent on and inversely proportional to the mixing ratio of water, which in the simulations conducted was in the form of ice. The shortest radiation penetration depth, h, occurs for the highest ice mixing ratio, $q_i = 1$ g kg^{-1}. The smallest value of h is calculated below, using equation 2.13 as previously discussed in Chapter 2.

$$h = \frac{1}{\gamma k(r_e) q_i \rho_{air}} = \frac{1}{(1.7)(0.045\frac{m^2}{g})(0.001\frac{kg}{kg})(432\frac{g}{m^3})} = 30.2\,m$$

The values used for γ and $k(r_e)$ are 1.7 and ~ 0.045 m^2 g^{-1} respectively, according to Ackerman et al. (1990) using $r_e = 20\,\mu$m, and $\rho_{air} = 432$ g m^{-3}is the density of air at cloud base. ρ_{air} is calculated by using the form of the ideal gas law $P = \rho RT$ (Salby, 1996) with values for pressure and temperature taken from the standard tropical atmosphere profile used in the model simulations. Repeating the calculationfor cloud top, where $\rho_{air} = 321$ g m^{-3}, gives a radiation penetration depth h of 40.7 m. Likewise, the calculation of h can be repeated for cloud base and top for all scenarios. The values of h are summarized in Table 3.1.

For several cases, a special consideration must be taken for the radiation penetration depth. From equation 2.13, h is an inverse function of the ice-water mixing ratio q_i; h increases as q_i decreases. For values of $q_i = 0.01$ g kg^{-1}, the radiation penetration depth, shown in Table 3.1, reaches a value of over 3000 m at cloud base and over 4000 m at cloud top. Since the cloud is only 2500 m thick at initialization, the calculated value of h exceeds the depth of the cloud. In these cases, the penetration depth h was approximated to be half the cloud depth, or 1250 m. This is supported by the plots of the vertical heating rate profile in Figure 3.1. Figure 3.1 shows the heating rate as a smooth, linear transition between heating at cloud base, and cooling at cloud top for the simulated cloud with $q_i = 0.01$ g kg^{-1}.

Table 3.1: Summary of values for radiation penetration depth h used in the model simulations

	$q_i = 0.01$ g kg^{-1}	0.1 g kg^{-1}	1g kg^{-1}
cloud top	4072 m	407 m	40.7 m
cloud base	3026 m	302 m	30.2 m

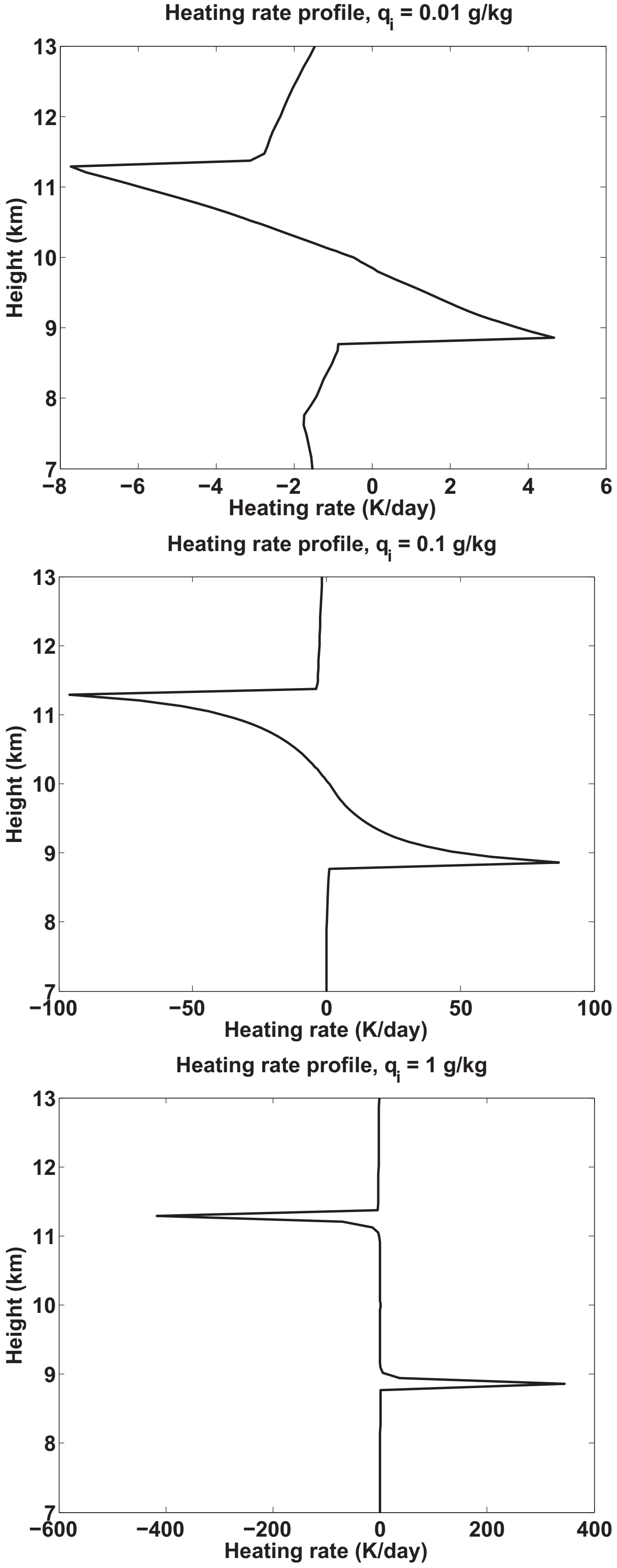

Figure 3.1: Heating rate profiles for $q_i = 0.01$ g kg^{-1}, $q_i = 0.1$ g kg^{-1}, and $q_i = 1$ g kg^{-1}

Horizontal grid size was increased to 100 m for the cases that required particularly large domains to facilitate reasonable computation times. As the horizontal domain size increases and horizontal resolution remains constant, the number of grid points and computational time increases as x^2 if x is the length of one side of the domain. If the domain size is doubled, i.e. from 1 km by 1 km to 2 km by 2 km, the time needed for computation roughly increases by a factor of 4. As such, it was necessary to reduce the horizontal resolution in the simulations with very large horizontal domains or the memory required for the model would exceed the memory allocation of the computer itself. Table 3.2 shows the horizontal resolution setup for each particular case.

The vertical domain spanned 17 km with a stretched grid spacing. The highest resolution for the stretched grid was placed at the center of the initial cloud with grid size of 30 m, again determined by the radiation penetration depth given in equation 2.13. The vertical resolution decreased logarithmically to a maximum grid spacing of approximately 300 m at the top of the model and approximately 400 m at the surface. A sponge layer was placed above 14 km to dampen vertical motions at the top of the model and to prevent reflection of gravity waves off the top of the model domain. The model time step for dynamics was between 1.0 and 10.0 s and was chosen to be the largest time step that would result in a stable model for computational efficiency. If too large of a time step is chosen, the model becomes computationally unstable. This means that the derivative values that the model uses to increment model variables between time steps become so large that they produce unrealistically large values of model variables, resulting eventually in values that exceed tolerance limits set in the model.

Radiative transfer calculations were performed at a time step of 60 s. Only thermal

Table 3.2: Model horizontal resolutions

horizontal grid size	L=100 m	1 km	10 km
q_i=0.01 g kg^{-1}	30 m	30 m	100 m
0.1 g kg^{-1}	30 m	30 m	100 m
1 g kg^{-1}	30 m	30 m	100 m

radiation was considered in this study, and solar radiation was not included in the radiation calculations as a simplification. This study acted as a sensitivity study on the response of clouds to thermal radiation. Solar radiation acts on a diurnal cycle while thermal radiation has a constant influence on clouds. In this regard, thermal radiation, while energetically less intense than solar radiation, is important at all times during the day. Thermal radiation can be considered the background radiative forcing experienced by clouds with solar radiation acting as a perturbation on the background field. By no means does this simplification imply that solar radiation is an unimportant feature. Further investigations can be conducted to investigate the effects of solar radiation on cloud evolution.

For all cases the model was initialized with a standard tropical profile of temperature and atmospheric gases with a Brünt-Vaisala frequency N of approximately 0.01 s^{-1}. Relative humidity was set to a constant 70% with respect to water in the layer below the cloud from the surface to a height of 7.8 km. In the upper layer in the model from 7.8 km upwards, which contained the cloud, relative humidity with respect to ice was set to a constant value of 70%. All clouds were initialized as homogeneous cylindrical ice clouds as shown in Figure 3.2. Ice particles within the cloud were of uniform size with a fixed effective radius of 20 μm and initialized with a specific, uniform mixing ratio as prescribed by the particular case. Cloud radius was prescribed by the particular case and a thickness of 2500 m with the cloud base set at 8.8 km. Cloud base was chosen such that the cloud top would be placed in accordance with the Fixed Anvil Temperature hypothesis (Hartmann and Larson, 2002). Both the cloud and surrounding atmosphere were initialized at rest. No precipitation was allowed in any of the model simulations. Cloud particle fall speed was also neglected. In reality the terminal velocity of ice, $V_t\;(r_e = 20\,\mu m) > 0$. All cases were run for one hour of model simulation time.

Figure 3.2: 3D surface of initialized cloud for all simulations

3.3 Specific Setups

Two parameters were varied throughout this study in order to describe a parameter space of cloud behavior. These variables were cloud radius L and cloud ice-water mixing ratio q_i. These two parameters were varied through several orders of magnitude to explore a wide parameter space of possible behaviors. Cloud radius was chosen to be 100m, 1km, or 10km. The ice-water mixing ratio was set at 0.01g/kg, 0.1g/kg, or 1g/kg. This provided 9 unique combinations of cloud size and density. These were the only changes made between each case. All other parameters of the the model were held constant.

These parameters were chosen to sweep out all possible combinations in parameter space, including combinations that do not occur naturally. In the case of these combinations that do not naturally occur, the results in Chapter 4 show that the combination is unstable and rapidly moves towards a more stable arrangement. It is recognized that the vast majority of cirrus clouds occur with values of q_i that are much smaller that 1g/kg. The values used in this study were chosen to examine a wide variety of clouds, rather than focus on only the most commonly occurring. As such, while very few cirrus clouds exist with q_i values of 1g/kg, the study of such clouds can yield insight into how radiative processes drive cloud evolution.

3.4 Summary of Initial α_i and Dimensionless Numbers

Tables 3.3, 3.4, and 3.5 list the values for α for each of the orthogonal evolution modes described in chapter 2 (Equations 2.54, 2.55, and 2.60). It is important to note that all these values are computed for the initial timestep at the base of the cloud.

As discussed previously in Chapter 2, evolution by means of precipitation is not considered in this study. However, the magnitude of α_{precip} is comparable or smaller than the magnitude of the other α's, meaning that the radiatively driven cirrus cloud evolution processes discussed in this study are at least as important as the precipitation processes.

Additionally, the set of dimensionless numbers S and E describe a phase space for cloud evolution. Tables 3.6 and 3.7 show the values for each number for all cases.

Table 3.3: Values for rate α_{strat} one of the orthogonal evolution modes

$\alpha_{strat} = \frac{\mathcal{H}g}{\theta N^2 h}$	L=100 m	1 km	10 km
q_i=0.01 g kg^{-1}	1.3×10^{-5}	1.3×10^{-5}	1.3×10^{-5}
0.1 g kg^{-1}	9.8×10^{-5}	9.8×10^{-5}	9.8×10^{-5}
1 g kg^{-1}	0.040	0.040	0.040

Table 3.4: Values for rate α_{mix} one of the orthogonal evolution modes

$\alpha_{mix} = \frac{Nh}{L}$	L=100 m	1 km	10 km
q_i=0.01 g kg^{-1}	0.12	0.012	1.2×10^{-3}
0.1 g kg^{-1}	0.030	3.0×10^{-3}	3.0×10^{-4}
1 g kg^{-1}	3.0×10^{-3}	3.0×10^{-4}	3.0×10^{-5}

Table 3.5: Values for rate α_{evap} one of the orthogonal evolution modes

$\alpha_{evap} = \frac{c_p \mathcal{H}}{L_v q_i}$	L=100 m	1 km	10 km
q_i=0.01 g kg^{-1}	0.0020	0.0020	0.0020
0.1 g kg^{-1}	0.0035	0.0035	0.0035
1 g kg^{-1}	0.0014	0.0014	0.0014

Table 3.6: Spreading number S

$S = \frac{\alpha_{strat}}{\alpha_{mix}} = \frac{\mathcal{H}gL}{\theta N^3 h}$	L=100 m	1 km	10 km
q_i=0.01 g kg^{-1}	1.1×10^{-4}	1.1×10^{-3}	0.011
0.1 g kg^{-1}	3.3×10^{-3}	0.033	0.33
1 g kg^{-1}	13	130	1300

Table 3.7: Evaporation number E

$E = \frac{\alpha_{evap}}{\alpha_{strat}} = \frac{c_p \theta N^2 h}{g L_s q_i}$	L=100 m	1 km	10 km
q_i=0.01 g kg^{-1}	150	150	150
0.1 g kg^{-1}	35	35	35
1 g kg^{-1}	0.35	0.35	0.35

CHAPTER 4

RESULTS

The simulations of clouds used to sweep out the parameter space of variables as described in section 3.3 can be divided according to their evolutionary behaviors. These are the independent orthogonal modes of evolution described in Chapter 2, specifically mixing and isentropic adjustment. In the following sections, only selected simulations will be discussed. Individual cases that provide a clear picture for each mode will be individually discussed in relation to the regime of dimensionless number space in which the case falls. Corresponding plots for all cases can be found in the appendix. The discussion of results in this chapter will be arranged according to the values of the dimensionless numbers S and E. Cases that describe the phase space in S will be discussed first, since values of E are relevant only when a mixed-layer does not form.

4.1 Isentropic Adjustment

For simulated clouds with values of $S < 1$, cloud base heating will drive a laminar lifting of cloud base and spreading of the cloud as return circulations from the laminar lifting carry condensed water outward. A good example of this behavior is the simulated cloud with $L = 1$ km and $q_i = 0.1$ g kg^{-1}. This case has a value of $S = 0.033$, favoring isentropic adjustment. Figure 4.1 shows the isentropes (contours in θ_e) becoming more closely stacked in the vertically due to the cloud scale circulations while remaining horizontal.

As expected, the simulated cloud undergoes rising at cloud base and sinking at cloud top, while spreading horizontally. This can be seen in Figure 4.2.

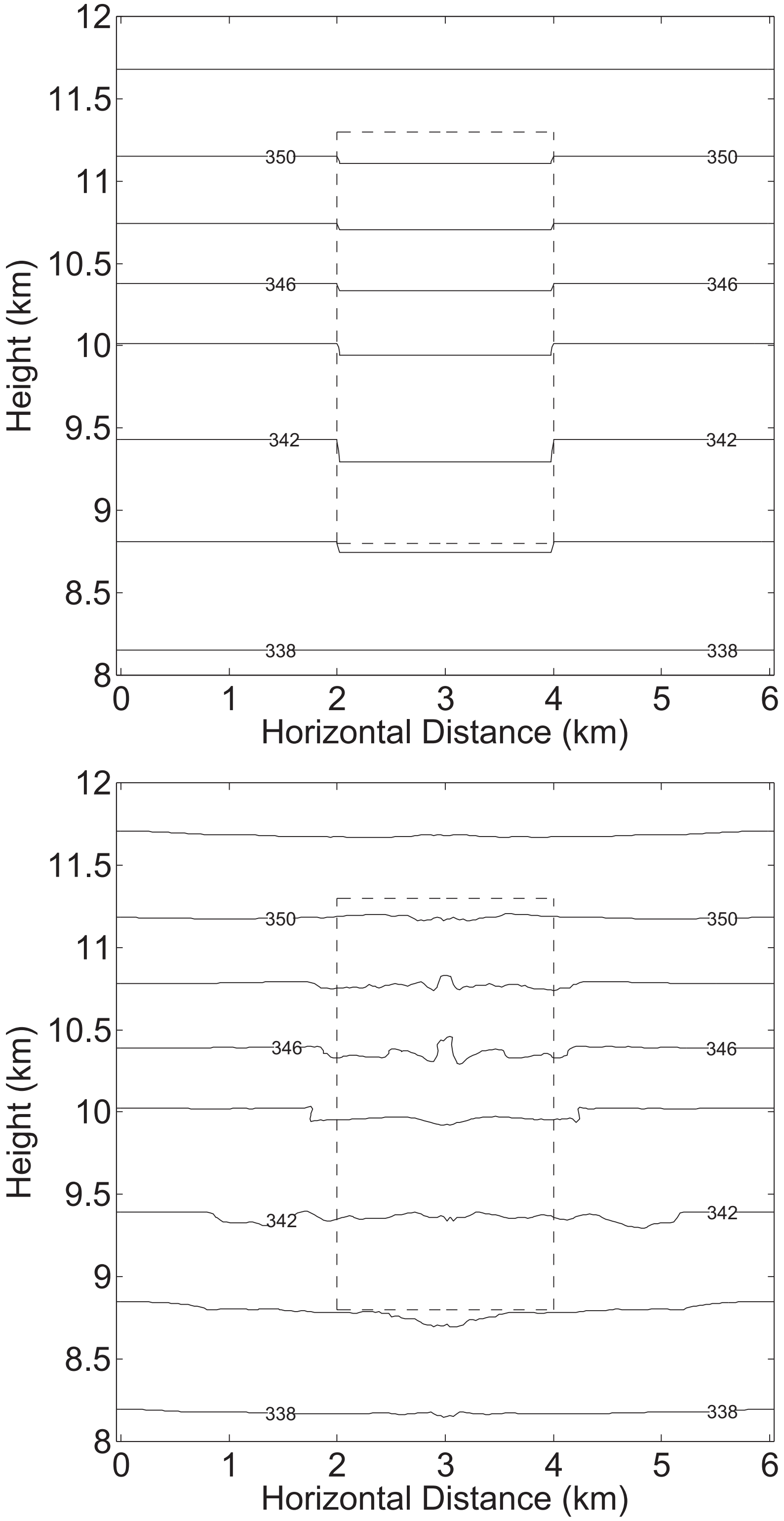

Figure 4.1: Cross section of θ_e contours through a cloud with L=1km and q_i=0.1 g kg^{-1} after 0 s and 3600 s of simulation

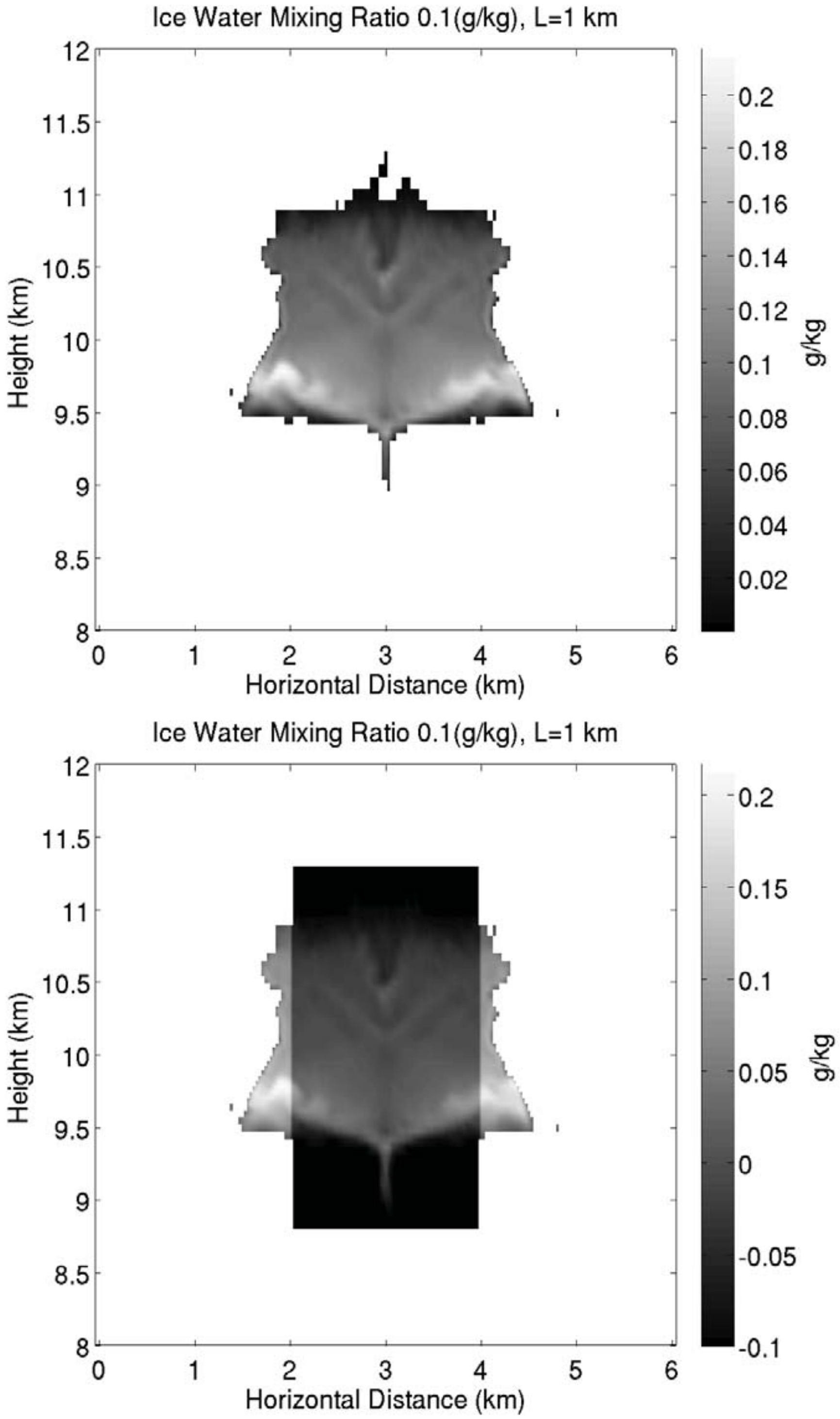

Figure 4.2: q_i cross section and differential q_i cross section of a cloud with L=1 km and q_i=0.1 g kg^{-1} after 3600 s of simulation

The plot of differential q_i cross section clearly shows cloud top descending, cloud base rising, and the cloud spreading horizontally.

4.2 Isentropic Adjustment and Mixing

Simulations with $S \sim 1$ will exhibit a mixture of both the spreading responses, isentropic adjustment and mixed-layer development. A good example of this behavior is the simulated cloud with $L = 10$ km and $q_i = 0.1$ g kg^{-1}. This case has a value of $S = 0.33$, placing the expected evolution behavior in the regime favoring isentropic adjustment. However, it is important to note that the "Spreading Number" S for this simulation, while less than one, is not significantly less than one. As seen in Figure 4.3, the isentropes (contours in θ_e) become more closely stacked in the vertical direction due to the circulations at cloud top and cloud base.

As expected, the simulated cloud undergoes rising at cloud base and sinking at cloud top, while spreading horizontally. This can be seen in Figure 4.4. The plot of differential q_i cross section clearly shows cloud top descending, cloud base rising, and the cloud spreading horizontally. The characteristic "bowl" shape of the horizontal spreading along isentropic surfaces can also be seen. This "bowl" shape develops as radiative heating at a given pressure level bends down isentropic surfaces.

Since the "Spreading Number" S for this simulation, while less than one, is not significantly less than one, there are indications of convective overturning at cloud base that are characteristic of a mixed-layer. With a value of $S = 0.33$, energy used for cloud evolution is partitioned in the ratio of S, meaning that for every 4 units of energy deposited into the cloud that are available to do work, 3 are used for spreading according to isentropic adjustment, while one is used for spreading according to the development of a mixed-layer. As such, a mixed-layer does develop at the cloud boundaries, as seen in Figure 4.5. However, the mixed-layer depth at cloud base is only ~ 300 m deep and elevated above initial cloud base. In cases with $S \gg 1$, discussed in section 4.3, the mixed-layer can be at least double

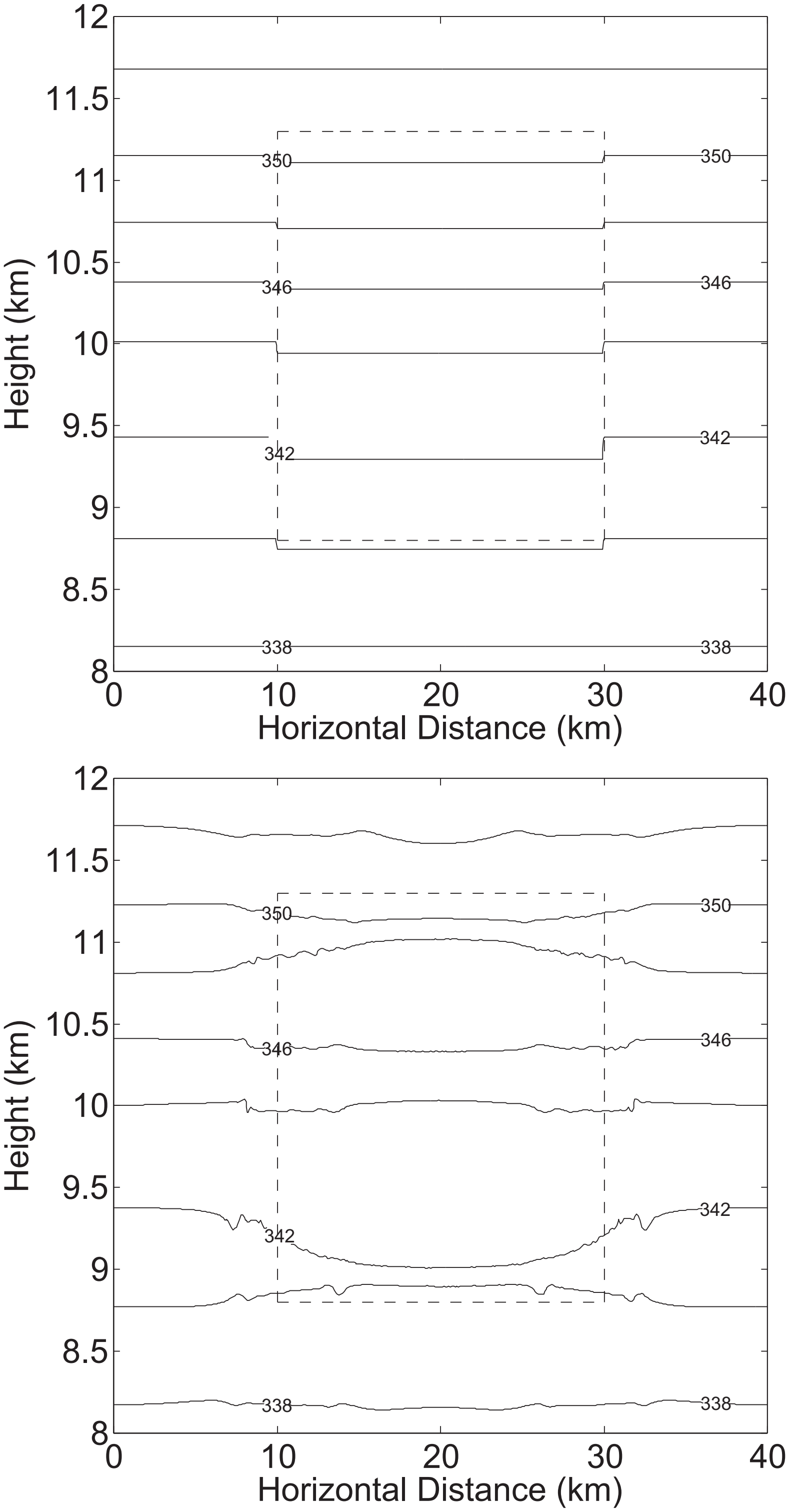

Figure 4.3: Cross section of θ_e contours through a cloud with L=10 km and q_i=0.1 g kg^{-1} after 0 s and 3600 s of simulation

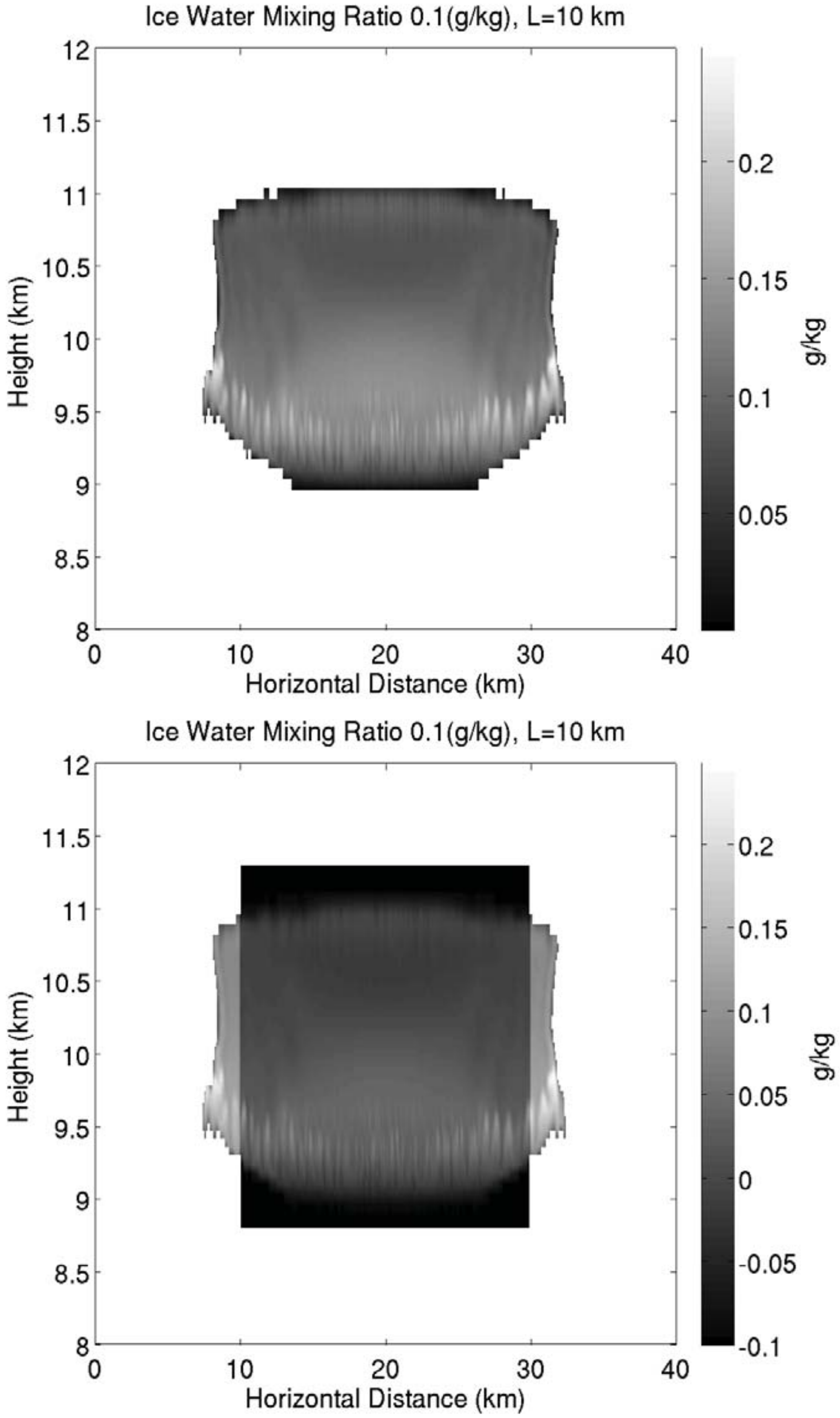

Figure 4.4: q_i cross section and differential q_i cross section of a cloud with L=10 km and q_i=0.1 g kg^{-1} after 3600 s of simulation

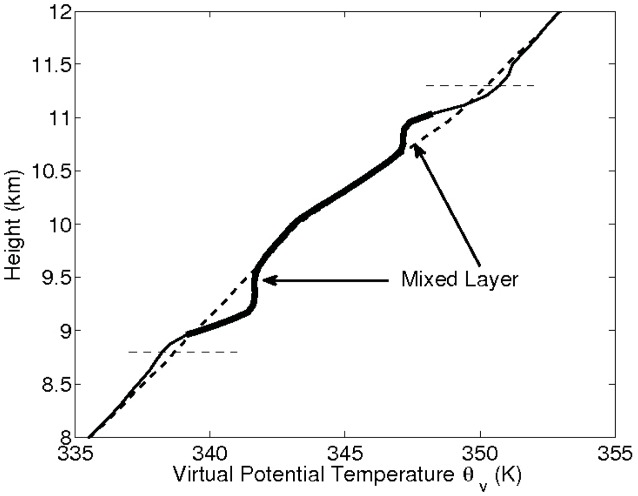

Figure 4.5: θ_v profile of a cloud with L=10 km and q_i=0.1 g kg^{-1} after 3600 s of simulation. The initial profile is plotted in a dashed line with horizontal dashed lines indicating initial cloud base and cloud top.

the depth seen here.

4.3 Mixing

Simulated clouds with values of $S > 1$ will not be associated with cloud base lifting in a laminar fashion. Instead, isentropic surfaces are bent downward by radiative heating sufficiently rapidly so as to create a local instability so that cloud base circulations act to create a mixed-layer at cloud base. The strong localized circulations may also drive evaporation or formation of new condensed water at cloud base through turbulent entrainment as below cloud air mixed into the cloud. This differs from the behavior for $S < 1$ in section 4.1 in that the updraft velocities are much larger in simulations with $S > 1$.

Even though the cloud base circulations are much smaller than the horizontal extent of cloud base, the cloud itself will spread due to these circulations. At the top of the mixed layer, the cloudy air is more dense than the surrounding air. Radiative heating and convective overturning at cloud base will drive vertical mixing, which results in the cloud spreading horizontally in density currents along isentropic surfaces.

This section will look at the simulated cloud with $L = 10$ km and $q_i = 1$ g kg^{-1}

($S = 1300$ and $E = 0.35$) as initial conditions. Based on the value of S, it is expected that the cloud evolves through the development and subsequent deepening of a mixed-layer. The mixed-layer can be seen in the θ_v profile plotted in Figure 4.6, showing the average cloud properties after 1 hour of model simulation. This profile is an average of all profiles within 90% of L from cloud center. Individual profiles may have either subadiabatic or superadiabatic lapse rates in the mixed-layer region due to the individual circulations, but on average the mixed-layer exhibits an adiabatic, or vertical, profile in θ_v. As seen in Figure 4.6, the mixed-layer at cloud base spans nearly 800 m. If the simulation were to continue past the 1 hour mark, the mixed layer should deepen even further.

The mixed-layer can also be seen in cross sectional plots of q_i. Figure 4.7 shows the mixed-layer at both cloud base and cloud top with the circulations indicated by the darker shading where drier air has been entrained from the surrounding region. Also visible on the differential q_i cross section is the fact that cloud base and cloud top remain at roughly the same elevations. This is due to the circulations in the mixed-layers helping to maintain the isentropic surfaces at both cloud base and cloud top.

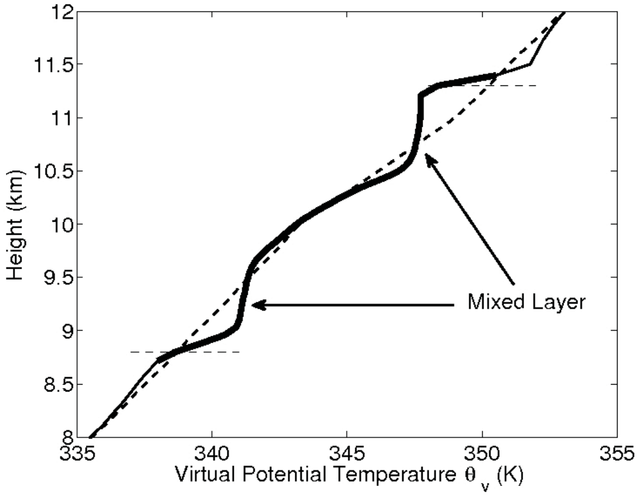

Figure 4.6: θ_v profile of a cloud with L=10 km and q_i=1 g kg^{-1} after 3600 s of simulation. The initial profile is plotted in a dashed line with horizontal dashed lines indicating initial cloud base and cloud top.

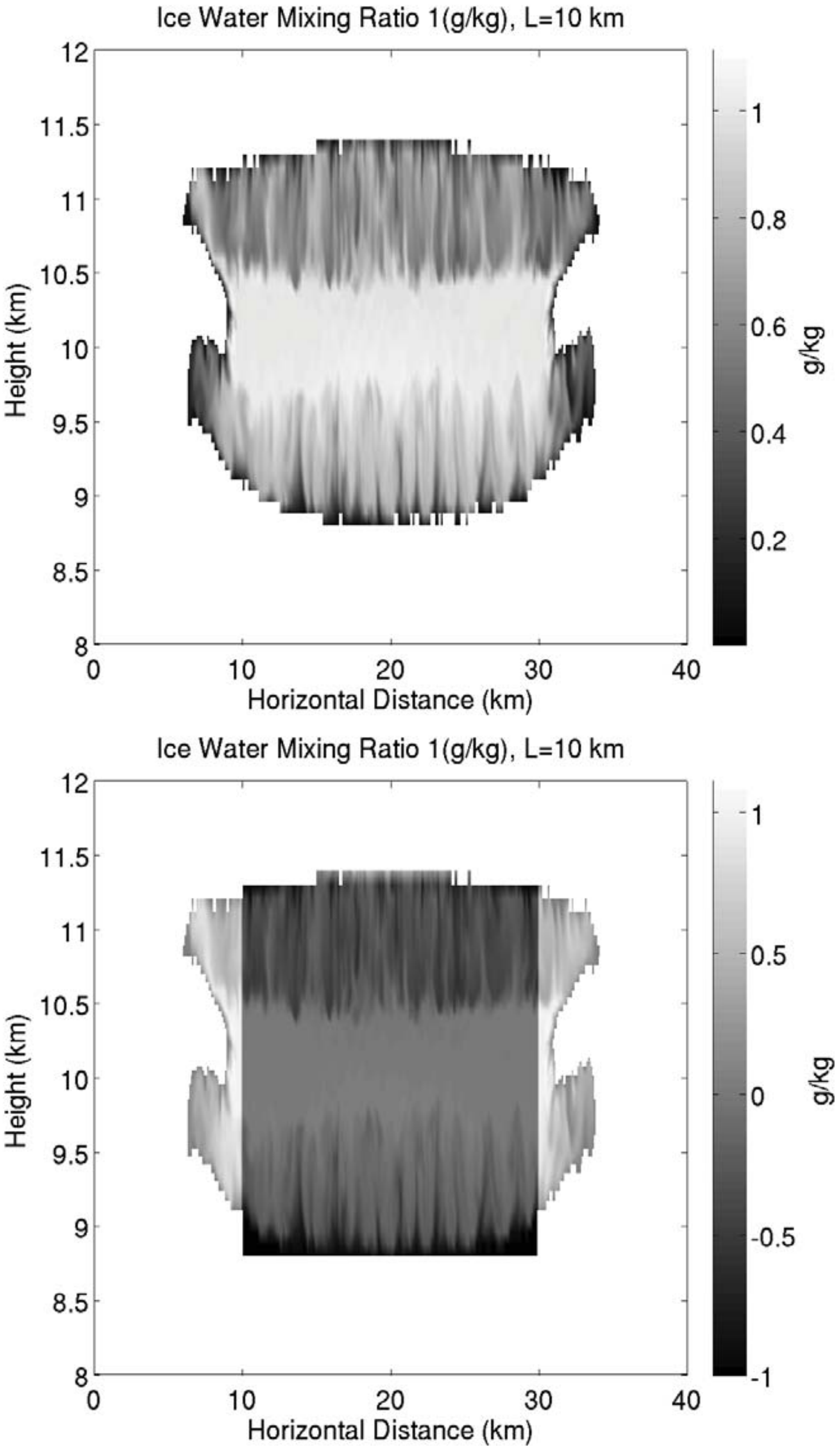

Figure 4.7: q_i cross section and differential q_i cross section of a cloud with L=10 km and q_i=1 g kg^{-1} after 3600 s of simulation

Previously, radiative flux divergence at cloud base and cloud top led to heating and cooling respectively, driving laminar vertical motions. With the mixed-layer circulations, this laminar vertical motion does not occur and the circulations produce significantly lessened or no vertical motions as the cloud spreads along isentropes (as seen in Figure 4.8), unlike in Figure 4.4 for a cloud with values of $S = 0.33$. This accounts for the sharp upward bend in "bowl" shaped spreading of the cloud seen in the q_i cross sections.

The curvature of the isentropes is caused by radiative flux divergence due to radiative interactions with condensed cloud matter. At cloud base, where there is cloudy air, the air is heated due to cloud ice absorbing longwave radiation, which moves the air to a higher isentropic surface, with the opposite occurring at cloud top. The horizontal motions driven by radiative heating will move outward along these newly defined isentropes.

The spreading and mixed-layer convection is also visible in the simulated 3D images of the cloud. Figure 4.9 shows the 0.1 g kg^{-1} isosurface of the cloud. The anvil outflows at cloud top and cloud base are clearly visible. The mixed-layer circulations at cloud base, particularly those along the outflow, have a mammatus-like quality to them. This case prompted further investigation into mammatus cloud formation, which will be discussed in Chapter 5.

4.4 Evaporation

Simulated clouds with $S < 1$ and $E > 1$ will evolve through evaporation. In these clouds, if only S were to be considered, it would be expected to undergo laminar lifting at cloud base. However, with $E > 1$, evaporation of condensed matter will be favored over the heating and rising of air at cloud base, where vertical laminar flows will be inhibited.

In this section, a cloud with $L = 1$ km and $q_i = 0.01$ g kg^{-1} ($S = 1.1 \times 10^{-3}$ and $E = 150$) will be considered. Based on these dimensionless numbers, the expected evolution of the cloud is to evaporate, rather than to develop a mixed-layer or undergo isentropic adjustment.

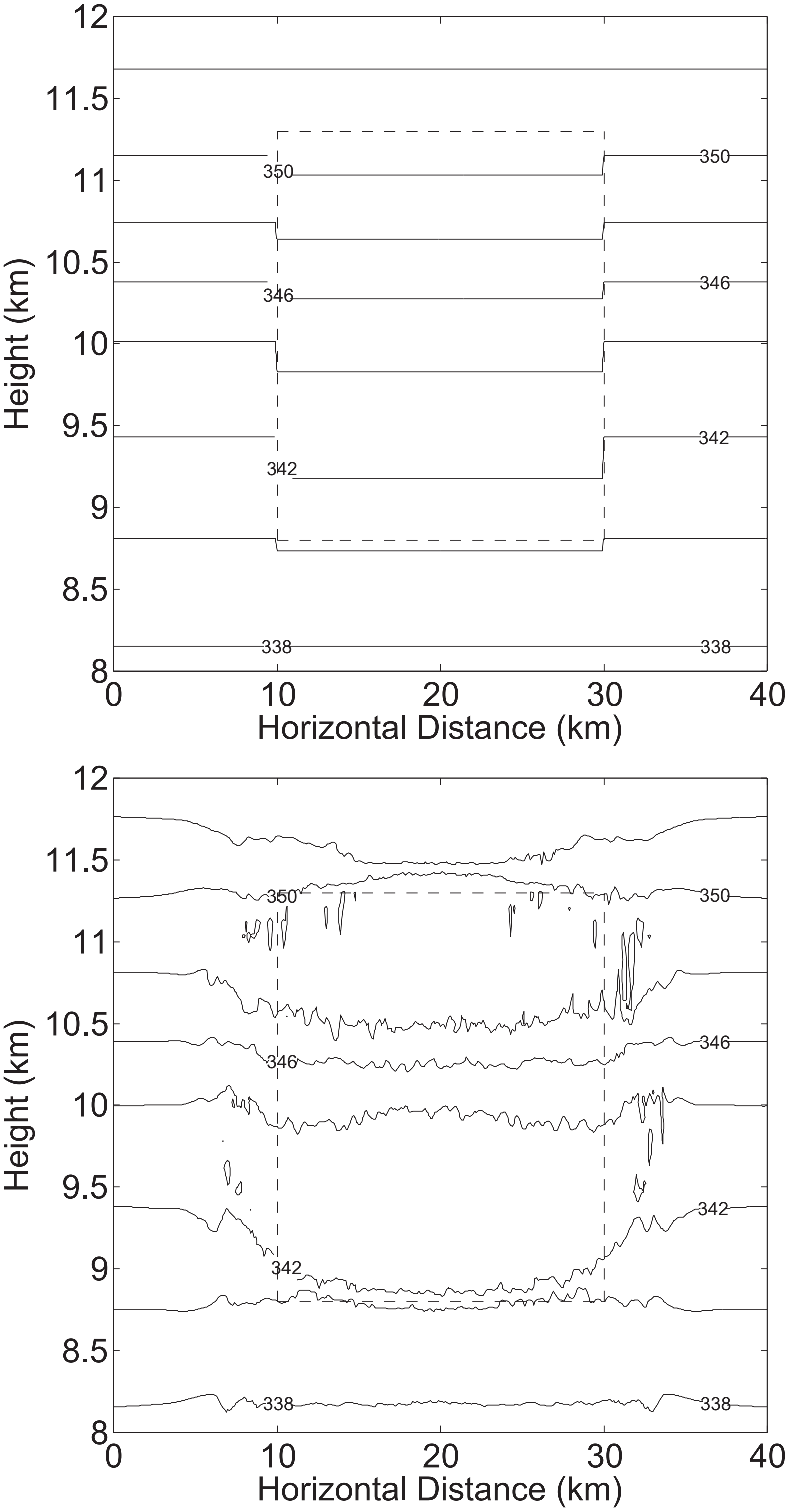

Figure 4.8: Cross section of θ_e contours through a cloud with L=10 km and q_i=1 g kg^{-1} after 0 s and 3600 s of simulation as well as the difference between the final and initial states

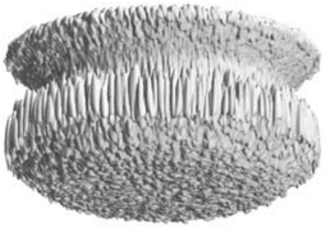

Figure 4.9: 3D surface of a cloud with L=10 km and q_i=1 g kg^{-1} after 3600 s of simulation

Table 4.1: Percent mass change of the simulated cloud over 1 hour

% mass change $\frac{m_f - m_i}{m_i}$	L=100 m	1 km	10 km
q_i=0.01 g kg^{-1}	-17.60	-7.23	-5.73
0.1 g kg^{-1}	21.14	24.51	24.14
1 g kg^{-1}	-6.38	7.78	9.08

Calculation of the simulated cloud mass at both the initial time and after 3600 s indicate that in this case, the cloud mass decreases by 7.23%. Values of cloud mass change are shown in Table 4.1. All clouds with $q_i = 0.01$ g kg^{-1} undergo evaporation. This is a result of all of these clouds having $S < 1$ and $E > 1$.

While percent mass change over the course of an hour may be a useful tool at evaluating evaporation in slowly evolving cases, useful insight may be lost to the coarse temporal resolution of this analysis in fast evolving cases. Another means to evaluate evaporation in cloud evolution is to look at the logarithmic change in condensed cloud water mass over time in a particular layer in the model. To evaluate this $d \ln m/dt$ was calculated over the first output model timestep only within the lower layer in which radiation from the surface is absorbed, h (Equation 2.13), rather than the entire cloud. The output model timestep is different from the timestep used for numerical calculations, which is 2 s. Model output timesteps occur at much larger intervals, in this case 180 s. The absorptive layers were taken to be 30 m, 300 m, and 1250 m for cloud ice water mixing ratios of 1, 0.1, and 0.01 g kg^{-1} respectively. The calculated values are shown in Table 4.2.

All values in table 4.2 are negative due to the evaluation of $d \ln m/dt$ at cloud base.

Table 4.2: Logarithmic mass change of the simulated cloud over 180 s in units of hr^{-1}, with a box around the entries with $S < 1$

$\frac{d\ln m}{dt}$	E=150	35	0.35
smaller S	-5.76	-0.79	-3.9
$\downarrow$	-3.96	-0.72	-1.29
larger S	-1.51	-0.68	-1.01

The table itself is arranged with columns having constant values of E and values of S increasing towards the bottom of the table. As expected, the highest values occur where E is maximized, and decrease with increasing S, perhaps because stronger mixing at cloud base replaces evaporated cloud condensate with newly formed cloud matter. As E decreases to a value of 35, values of mass change also decrease correspondingly, retaining the decrease with increasing S.

However, at values of E=0.35, the mass change jumps upward sharply. This is not a result of evolutionary behavior, but likely a consequence of model setup as well as the definition of how $d\ln m/dt$ is calculated.

The logarithmic mass change is calculated across the model layer in which radiative absorption occurs. Cases with values of E=0.35 all have an ice water mixing ratio of 1 g kg^{-1}. With this mixing ratio, radiation in the thermal spectrum is absorbed in the first 30 m into the cloud. With the prescribed model vertical resolution, this occurs in a layer that is one model grid point in depth. These cases also have the highest values of S, and as a result are in the mixing evolutionary regime. In this regime of S, cloud circulations carry condensed water upwards out of the very thin model layer in which the logarithmic mass change is calculated. Drier air from below cloud base mixes into this layer, resulting in the larger values of $d\ln m/dt$ shown in table 4.2.

The cloud with $S = 1.1 \times 10^{-3}$ and $E = 150$ experiences no spreading behavior, either through the development of a mixed-layer or through isentropic adjustment. The time scale for isentropic adjustment is long compared to simulation time, and does not occur by the end of the hour simulation. Simply, the cloud is slowly eroded through radiative flux convergence at cloud base and the resulting evaporation. This is evident in the differential q_i cross section plot in Figure 4.10. At cloud base, there is a section of cloud that is present in the initial cloud, but not in the final cloud. The cloud also remains within the bounds of the initial cloud after an hour of elapsed simulation, so no spreading is evident. Mass in the absorptive layer h decreases over time, as well as total mass of the cloud, indicating that cloud mass is decreasing due to radiative heating, rather than being moved to a different position in the cloud.

4.5 Nonevaporating Cases

Simulated clouds with both $S < 1$ and $E < 1$ will undergo laminar vertical rising of cloud base, with the corresponding return circulations. These are the simulated cases discussed in section 4.1. In these cases, isentropic adjustment is favored by both dimensionless numbers. For values of $S < 1$, isentropic adjustment is favored over mixing, and for $E < 1$, isentropic adjustment is favored over evaporation.

4.6 Unstable Cases

Several of the simulated cases evolve very rapidly and move toward dissipation of the cloud by the end of the hour of simulation. These cases shall be considered unstable in the sense that the cloud will not persist naturally. The clouds that exhibit this behavior are all in the L=100 m regime of the investigated parameter space. Clouds that persist in nature are unlikely to be narrow in horizontal extent and tall in the vertical extent (2500 m). The few clouds that do take this shape (i.e., convective towers) rapidly spread out into thin cirrus anvils and dissipate relatively quickly. This is analogous to the L=100 m q_i=1 g kg^{-1} case. The cloud in this simulation rapidly spreads out at cloud base and cloud top forming anvils, and by the end of the hour of simulation has almost completely dissipated as seen in the 3D simulations in Figure 4.11.

These 3D images tell an interesting story. In this cloud, the dimensionless numbers have values of $S = 13$ and $E = 0.35$, which are within an order of magnitude of each other.

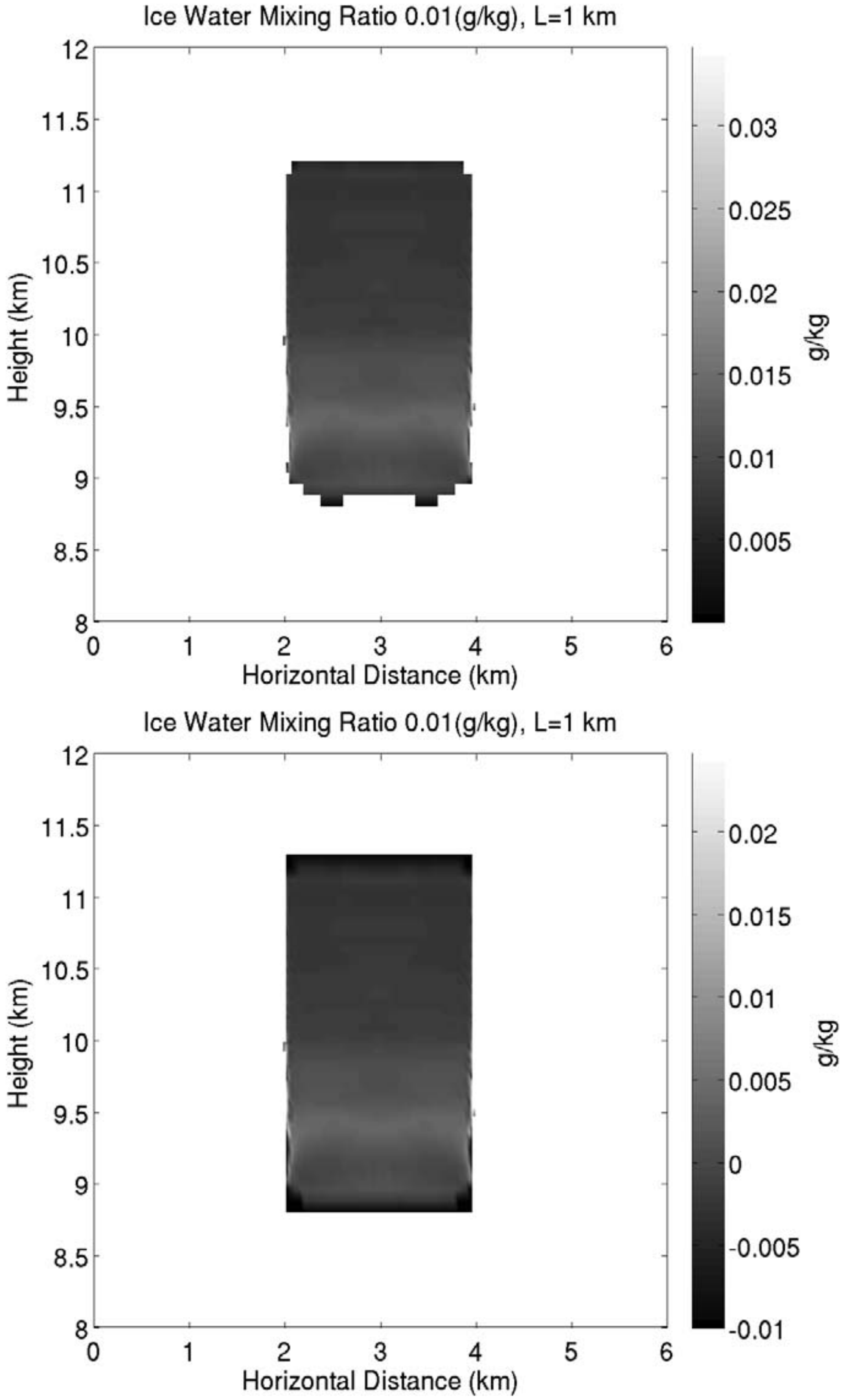

Figure 4.10: q_i cross section and differential q_i cross section surface of a cloud with L=1 km and q_i=0.01 g kg^{-1} after 3600 s of simulation

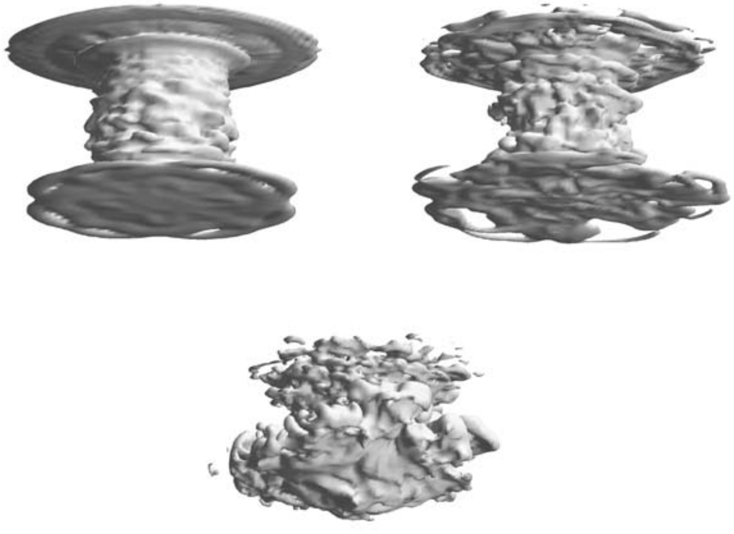

Figure 4.11: 3D surface of a cloud with L=100 m and q_i=1 g kg^{-1} after 900 s, 1800 s, and 3600 s of simulation

Initially, the "Spreading Number" dominates, as its value is greater than unity. As such, the cloud develops a mixed-layer and spreads horizontally. This mixed-layer develops rapidly with a mixed-layer depth of ~100 m depth forming after just 180 s. However, at some time after 900 s, the cloud moves from the "spreading" regime into the "evaporation" regime. After 1800 s, the evaporation of cloud base can clearly be seen, and after 3600 s, the cloud mass has decreased by over 6% from the original mass. This is in contrast to the other cases with $E = 0.35$ ($q_i = 1$ g kg^{-1}) where the cloud mass increases after an hour of evolution.

It is possible that as the cloud spreads rapidly in the initial time steps, as seen in Figure 4.11, the concentration of ice q_i decreases as the mass of ice is dispersed through a larger volume. This decrease in q_i would have the effect of increasing the "Evaporation Number" E. The spreading and subsequent decrease in q_i perhaps has negligible effect on the "Spreading Number" S through decreasing $\mathcal{H}$ while at the same time increasing L. These changes could shift the evolution of the cloud into a different regime. In Figure 4.11, the evolution seems to shift between the times that are plotted. Between 0 and 900 s, as well as between 900 and 1800 s, the cloud spreads, and between 1800 and 3600 s, the cloud seems to stop spreading and start to dissipate.

This shows the dynamic nature of these dimensionless numbers. It is important to note that although they provide predictive utility, they are time dependent. The dimensionless numbers listed in this work were all evaluated at 0 s at cloud base, but in a rapidly evolving cloud such as the one described here, the dimensionless numbers themselves can also rapidly evolve since the quantities that determine the dimensionless numbers are themselves time dependent (equations 2.57 and 2.62). The "Spreading Number" S is a function of L, θ, and q_i through the variables h and $\mathcal{H}$. As the cloud expands, L increases, increasing S. As q_i increases, $\mathcal{H}$ increases and h decreases, both having the effect of increasing S. The base of the cloud is heated over time through absorption of longwave radiation, increasing θ, and decreasing S. The "Evaporation Number" E is a function of θ and q_i. Increasing θ will increase E, and increasing q_i will lower E as well as decrease h, which in turn will decrease E. The combined effects of these changes determine how S and E will evolve over time and produce feedback effects. For example, in Figure 4.11 the cloud spreads due to a value of $S > 1$. This spreading in turn leads to a larger value of L, which is a feedback that increases S. These feedbacks will not be discussed here, and are left for the subject of future investigations.

CHAPTER 5

SENSITIVITY OF CLOUD BASE TURBULENCE TO ATMOSPHERIC RELATIVE HUMIDITY

The simulations from the simulated case with $S = 1300$ and $E = 0.35$ ($L = 10$ km and $q_i = 1$ g kg^{-1}) indicated large cellular structures that resemble mammatus-like formations. 3D plots of this simulations in Appendix B shows these mammatus-like formations. Here, several high-resolution simulations are performed to specifically investigate the formation of mammatus clouds. Otherwise, model initial conditions are identical, except that the relative humidity with respect to water in the lower troposphere layer was adjusted. In the previous model simulations, the relative humidity with respect to water in the layer between the surface and 1 km below cloud base was set to 50%. In these simulations relative humidity with respect to water in this layer is varied between 10% and 90%.

The reason for this experiment is that radiative energy is delivered to the cloud through thermal radiation emitted from the surface. The amount of energy delivered to cloud base via thermal emission from the surface is mediated by relative humidity in the air between the ground and the cloud, primarily in the lower troposphere layer. This is due to the way that water interacts with radiation as discussed in Chapter 2.

In the case of the UU LES model simulations discussed here, the relevant species in the layer of air below the cloud is water vapor. While other greenhouse gases are present in the below cloud layer, they are held constant between simulations. The amount of water vapor in the below cloud layer is varied through changing the relative humidity with respect to water in the lower troposphere layer. Relative humidity is affected by both amount of water vapor in the air as well as the temperature of the air. However, in the simulations, the temperature of the air is held constant, so the amount of water vapor in the lower troposphere air is directly changed by changing the relative humidity with respect to water in that layer. As the amount of water vapor goes up, the transmissivity goes down due to more matter in the path of the radiation to absorb the radiation (Salby, 1996).

Due to the size and density of the cloud in these cases, thermal radiation from the surface is readily absorbed in a thin layer at the base of the cloud. Convective overturning results from this intense heating of a thin layer at cloud base, forming the mammatus structures seen previously in the simulated cloud discussed previously in section 4.3. As more thermal spectrum radiative energy is available to the cloud due to the lessened lower troposphere relative humidity, the formation of these mammatus structures should be accentuated. With a high lower troposphere relative humidity, less radiative energy is available to the cloud and the formation of mammatus structures should be impeded.

To test the sensitivity of the formation of mammatus-like structures to the lower troposphere relative humidity, three cases were simulated. Identical homogeneous clouds were initialized at rest with either 10%, 50% or 90% relative humidity with respect to water in the lower troposphere layer. A diagram of the model domain is provided in Figure 5.1.

The lower troposphere layer extends in the model from the surface to 1 km below cloud base (7.8 km). Relative humidity in the lower troposphere layer, indicated in Figure 5.1 as RH_{LT}, will be referred to as the lower troposphere relative humidity, and will always be with respect to water. Above that layer, the relative humidity, indicated in Figure 5.1 as RH_{BC}, is considered with respect to ice was set to a constant 50%. This model layer will be referred to as the air immediately below the cloud or the cloud layer. When the cloud was initialized in the model, the relative humidity with respect to ice was automatically set at 100% where there was cloud. The cloud in these simulations was initialized with a radius L=10 km and a ice-water mixing ratio q_i=1 g kg^{-1}. This is identical to the simulation discussed previously in section 4.3, with the exception that the horizontal resolution was

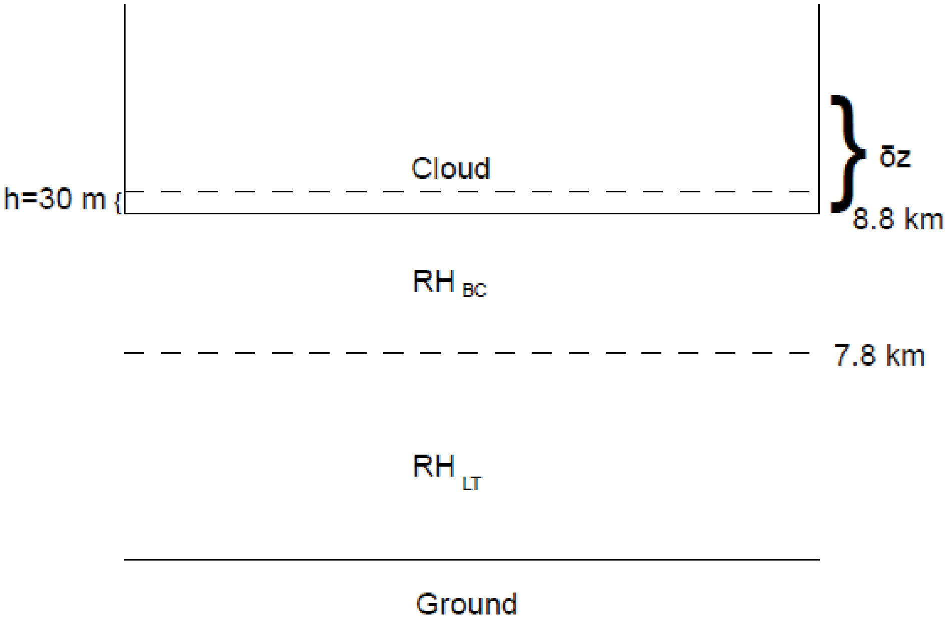

Figure 5.1: Diagram of the structure of the model domain

increased. Instead of the 100 m horizontal grid point spacing used previously, the mammatus simulations all used a 30 m horizontal grid point spacing. This was done so that the horizontal resolution matched the vertical resolution and so that the horizontal features produced in the model could be better resolved.

As seen in Figure 5.2, the heating rate at the base of the cloud in the mammatus simulations varies according to the lower troposphere relative humidity. With higher relative humidity, the radiation of the warm ground interacts more with the water vapor in the intervening atmosphere. Less of the initially emitted radiation reaches cloud base and while the water vapor re-emits the radiation that it absorbs, the water vapor emits at a colder temperature than the ground, reducing the intensity of thermal radiation incident upon the base of the cloud, resulting in a roughly 30% decrease in heating rate for the 90% case when compared to the 10% case. The reason is not linear with respect to relative humidity is that, as discussed in Chapter 2, strong line absorption by water vapor varies approximately as the square root of the humidity.

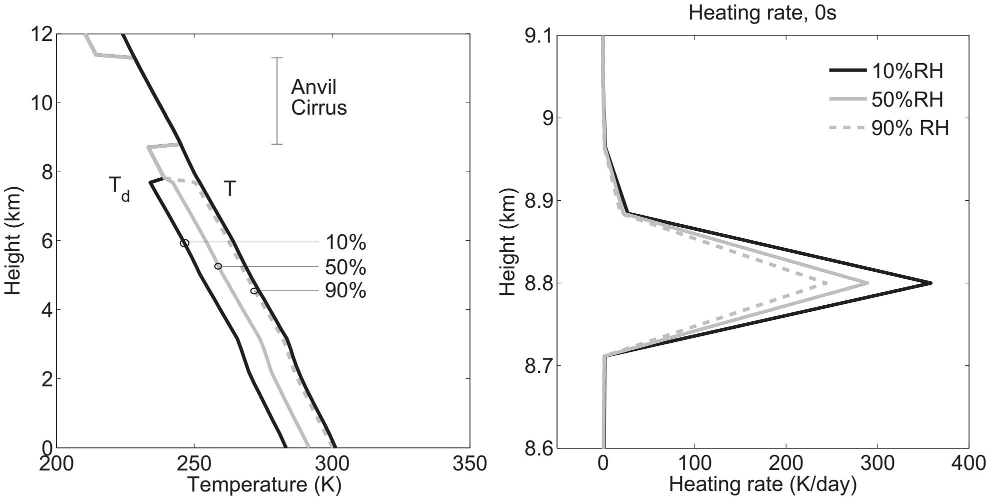

Figure 5.2: Initial temperature and dew point profiles and cloud base heating profiles for mammatus simulations

5.1 Cloud Ice Particles

Several measures can be used to determine the effect of RH_{LT} on mammatus formation. Figure 5.3 shows a 3D surface of the clouds simulated in the 10% and 90% RH_{LT} cases with a large portion of the cloud cut away such that the detail of the cloud structure can be seen more easily. The 10% case shows significantly larger lobes below the cloud than the 90% case. The increased thermal energy supplied to the cloud in the 10% case is the only difference between the two clouds in the simulation; therefore it must be responsible for the substantial difference in lobe size.

The 3D plots of the cloud in upper plots of Figure 5.3 show a 3D surface of the cloud along a constant value of cloud ice-water mixing ratio, q_i. When viewing the cloud, this is not the surface that would be seen. There is cloudy air below the surfaces plotted in Figure 5.3. This cloudy air would have the effect of smoothing out the features seen in the 3D plots. There is also the phenomenon known as radiative smoothing. This phenomenon was discovered when looking at Land Resource Satellite System (LandSat) images of stratocumulus (Davis et al., 1997). At small scales, the radiative transfer from the clouds no longer obeyed a $-\frac{5}{3}$ power law, rather it appeared far smoother at scales less than ~200-400 m. The key physical basis for radiative smoothing seems to be that the extinction function for

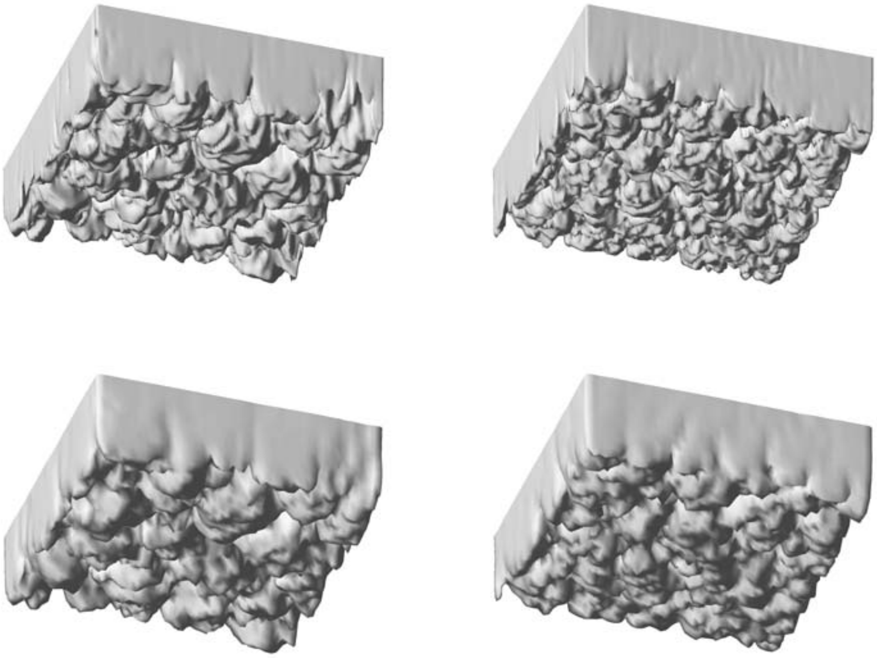

Figure 5.3: 3D surface of q_i=0.1 g kg^{-1} for mammatus simulations of 10% RH_{LT}, 90% RH_{LT}, 10% RH_{LT} smoothed, 90% RH_{LT} smoothed

radiation passing through a cloud is insensitive to variability in cloud at scales less than a critical value. For stratocumulus (Davis et al., 1997), that scale was between 200 and 400 meters.

In order to simulate this in the 3D plots, a new matrix of q_i data was created using only every third data point in a horizontal plane from the original matrix of q_i data, creating a spatial resolution of 180m, rather than the initial 60m, similar to the critical scale (Davis et al., 1997). This "sampling smoothing" method is plotted in the lower plots in Figure 5.3. When comparing the upper plots in Figure 5.3 with the lower plots, it can be noted that by using this smoothing method, the large structure is maintained while many of the fine details are lost. The net effect, however, is the production of a smoothed 3D cloud plot. A more rigorous approach to this "sampling smoothing" would be to average each data point with the surrounding data points. However, the "sampling smoothing" was done merely as a proof of concept. Rather than extend this sampling method, perhaps a better approach is to pass the results through a 3D radiative transfer solver.

There are several radiative transfer models that simulate the actual physics of radiation interaction with the atmosphere. These models can produce representations of what the simulated clouds produced with the UU LES would look like to the human eye, including the “radiative smoothing” effect described above. This differs from the 3D plots previously shown in the fact that the previous plots are solid surfaces along a constant value of ice water mixing ration. Rather than producing a solid surface, the radiative transfer models produce a image of the cloud based on its transmission and scattering of visible light. The radiative transfer model SHDOM (Evans, 1998) was used by Céline Cornet at the University of Lille in France to produce visible images of 1/4 the domain of the modeled clouds. These images are shown in Figure 5.4 as well as a photo of actual mammatus clouds for comparison. The bright spots in the lower right portion of the simulated images in Figure 5.4 are due to the fact that only a portion of the domain is used.

The image output from SHDOM indicate that the UU LES model can create realistic mammatus structures similar to those observed in a real environment. In addition, the SHDOM simulated images also indicate that the mammatus-like structures in the lower RH_{LT} case are larger than those of the high RH_{LT} case, and that the differences between the two are evident to the human eye. This is an important point as the definition of a mammatus lobe is primarily based on its visible appearance.

Cross-section plots of ice-water mixing ratios are also useful in comparing the size of mammatus lobes formed in the simulated cases. Since the mammatus features are seen primarily near the outer boundary of the cylindrical cloud base, radial plots will be used to investigate the mammatus lobes. The plots shown in Figure 5.5 show the physical shape of the mammatus lobes as described by the presence of ice. The cross-sections shown are taken across the same radial cross section of r=8500 m for all three cases. The plot is centered on the same angular arc on that cross section and zoomed in to show detail. The x-axis in Figure 5.5 spans one eighth the radial cross section, or approximately 6.7 km.

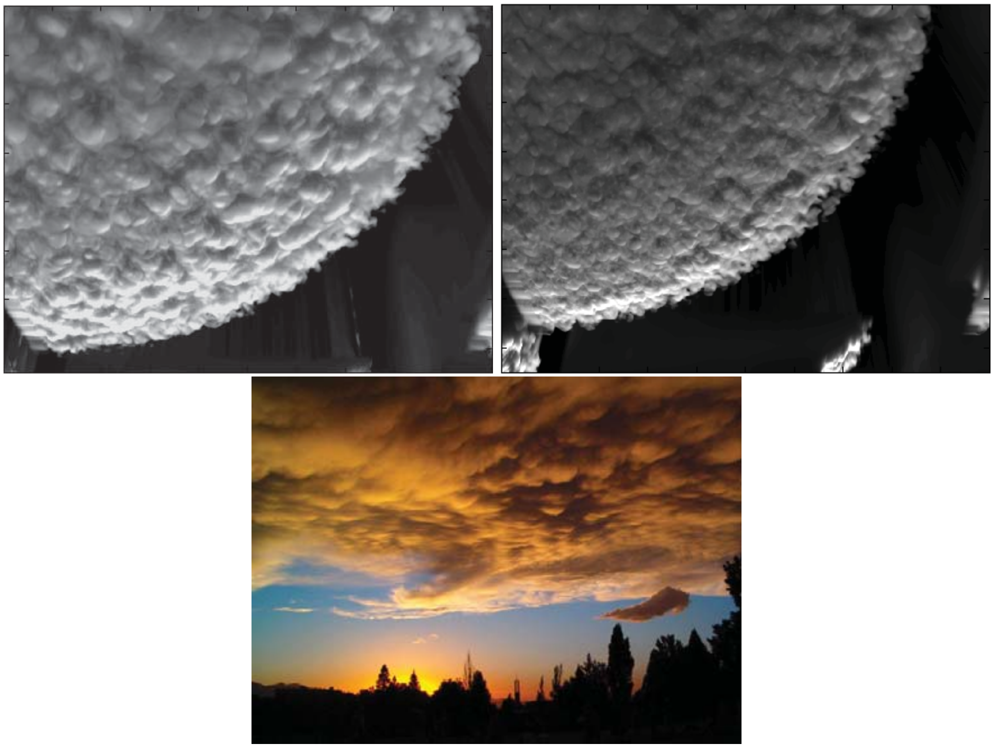

Figure 5.4: Visible spectrum images of the 1/4 the domain for simulated clouds at 3600 s for 10% RH_{LT}, 90% RH_{LT}, and a photograph of mammatus clouds taken in Salt Lake City on September 8th, 2005 (Courtesy of Lis Cohen)

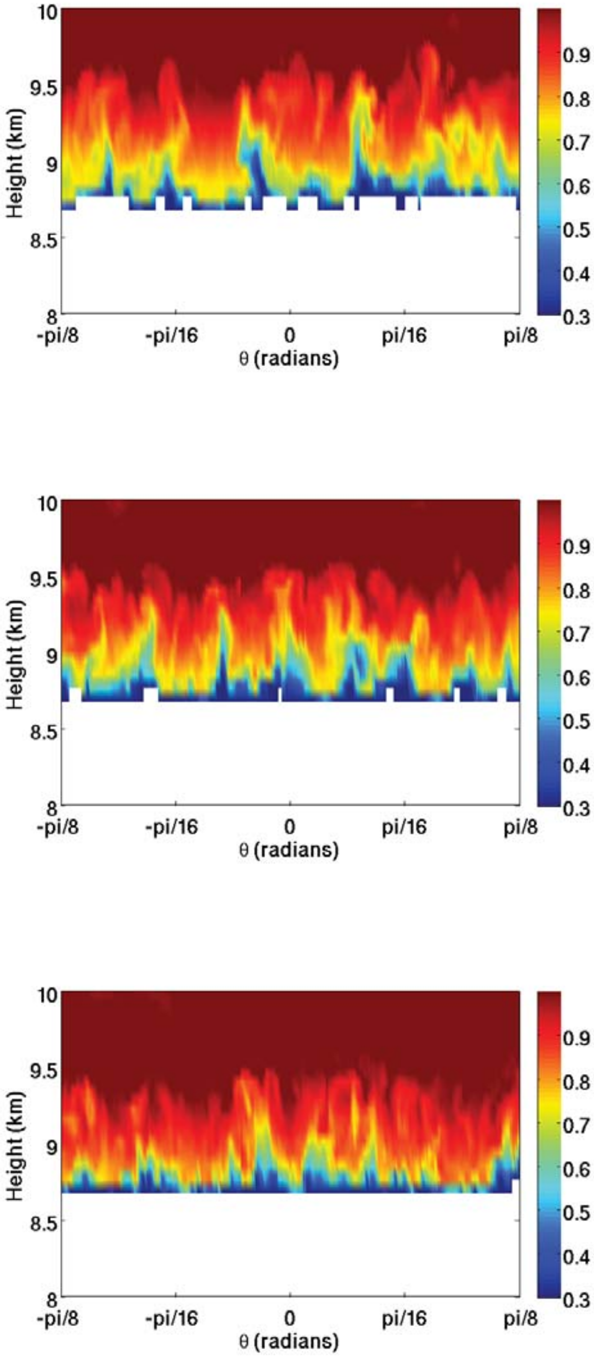

Figure 5.5: Cross-sections of ice-water mixing ratio at cloud base after 3600s of simulation for 10% RH_{LT}, 50% RH_{LT}, and 90% RH_{LT}

Larger lobes are seen in the lower RH_{LT} cases than in the cases with higher RH_{LT}. In the 10% RH_{LT} case, the largest lobe seen is approximately 800 to 1000 m in width. The 50% RH_{LT} case produces a largest lobe of approximately 500 m in width. The 90% RH_{LT} case produces a largest lobe of only 200 to 300 m in width.

5.2 Equivalent Potential Temperature

The mixed-layer in equivalent potential temperature, θ_e, that forms at the base of the cloud can be used as a measure of mammatus formation. More intense convective overturning due to stronger heating at cloud base leads to a deeper mixed-layer forming. Figure 5.6 shows the depth of the mixed-layer at the base of the cloud for all three simulated cases. The θ_e profiles plotted in Figure 5.6 are made by horizontally averaging a core from the center of the cloud. The mixed-layer in this case was taken to be the vertical layer with the steepest slope at the bottom of the cloud (another mixed-layer forms at the top of the cloud due to strong radiative cooling). The 10% RH_{LT} simulation formed a mixed-layer of approximately 750 m in depth, while the 90% RH_{LT} simulation formed a mixed-layer of approximately 500 m in depth.

5.3 Turbulence

Turbulent eddies can occur at all spatial scales that are resolved in the UU LESM model (Stull, 2009). In reality, turbulent eddies exist from the largest spatial scales down to about 1mm, where viscous dissipation of energy becomes dominant rather than turbulent dissipation. In the boundary layer, turbulence exists from the length scale of the depth of the boundary layer (as large as 4 km) down to viscous scales on the order of millimeters. The largest turbulent eddies have the greatest amount of kinetic energy while the smaller eddies have the least amount of kinetic energy. However, there are fewer large eddies and an abundance of small eddies. This is constrained by the equipartition theory (Kittel and Kroemer, 1998) in statistical mechanics which requires that the energy distribution be such that the energy density of the distribution remains equal across all modes.

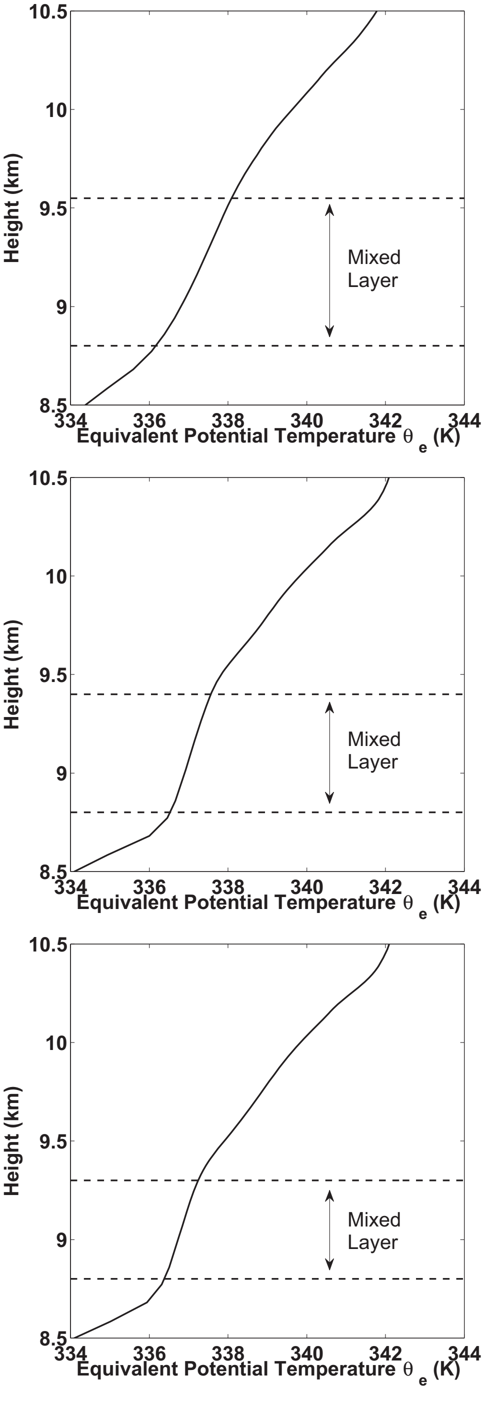

Figure 5.6: Temperature profiles of cloud base after 3600 s of simulation for 10% RH_{LT}, 50% RH_{LT}, and 90% RH_{LT} with a dashed line to indicate the boundaries of the mixed-layer.

Energy is transferred from larger spatial scales to smaller spatial scales through a turbulent energy cascade. The largest turbulent eddies can create wind-shear regions, which in turn generate smaller eddies. This progresses down the spatial scale until the scale of the turbulent eddies is small enough that viscous diffusion of energy can occur. The energy is then dissipated into heat through friction due to viscosity of the air. The characteristic slope of a turbulent energy cascade is -5/3 on a log-log plot of energy versus space.

The characteristic -5/3 slope of the turbulent energy cascade can be derived through dimensional analysis. Energy is dissipated on a length scale of

$$\kappa = \frac{2\pi}{\lambda}$$

where λ is the scale of viscous friction. In eddies, $\lambda < l$, where l is the size of the largest eddy. So, using dimensional analysis,

$$\frac{dE}{d\kappa} \sim u^2 l \tag{5.1}$$

However, we know that

$$\frac{dE_{TKE}}{dt} = -\overline{u'w'} - \overline{v'w'} + \frac{g}{\theta}\overline{u'\theta'} - \epsilon \tag{5.2}$$

where the first and second term produce turbulent kinetic energy (TKE) through shear, the third term produces TKE through buoyancy, and the fourth term is the dissipation term. Using dimensional analysis on equation 5.2, ϵ has units of

$$\frac{m^2}{s^3} \sim \frac{u^3}{l}$$

Knowing this, it is possible to rewrite equation 5.1 in terms of ϵ and κ, showing the -5/3 power relationship between the turbulent kinetic energy of an eddy and its scale.

$$\frac{dE}{d\kappa} \sim \epsilon^{\frac{2}{3}} l^{\frac{5}{3}} \sim \epsilon^{\frac{2}{3}} \kappa^{-\frac{5}{3}} \tag{5.3}$$

5.3.1 Cloud Base Height

A spectral analysis of the cloud base height, can provide insight into the size of the mammatus lobes and turbulent energy cascade. In the cases with more energy supplied to the ground through thermal radiation, there will be a stronger heating at the base of the cloud resulting in stronger convective overturning currents. Figure 5.7 shows a spatial power spectrum for cloud base height for each case simulated.

Figure 5.7 is made from the lowest height at which condensed ice-water is present in the model for 50 consecutive circular transects of the cloud, approximately 1500 m in width, in the region of mammatus formation. The transects were taken in the region of the cloud that is between 7000 m and 10,000 m from cloud center as shown in Figure 5.8.

A fourier transform (FT) is then performed on the data, and the domain is converted from wave-number space to a spatial domain. The FT calculated for each transect is the averaged with the rest of the transects to create a FT plot that is representative of the mammatus formation region. The variance of the transect data, calculated by taking the square of the absolute value of the FT and dividing by the length of the transect squared (Middleton, 2000), is plotted on the y-axis. The power plotted in Figure 5.7 corresponds to the amount of energy contained in the cloud at a particular spatial scale. The x-axis shows the spatial scale over which the plotted signal is observed in the model. Due to the model's 30 m grid spacing, the smallest features that can be discerned are given by the Nyquist frequency (James, 1999). In the case of spatial resolution however, the Nyquist frequency needs to be expressed in the spatial resolution of the sample. In order to resolve a signal, a minimum of three points are needed in the sample. In the model, this corresponds to a distance of 60m across the domain. In this sense, the model's Nyquist "frequency" is 60m, which is the smallest feature a FT can pick out in the model.

As seen in Figure 5.7, the 10% RH_{LT} and 50% RH_{LT} cases exhibit the characteristic -5/3 power law of turbulent energy cascades at smaller scales. The 90% RH_{LT} case, however, does not.

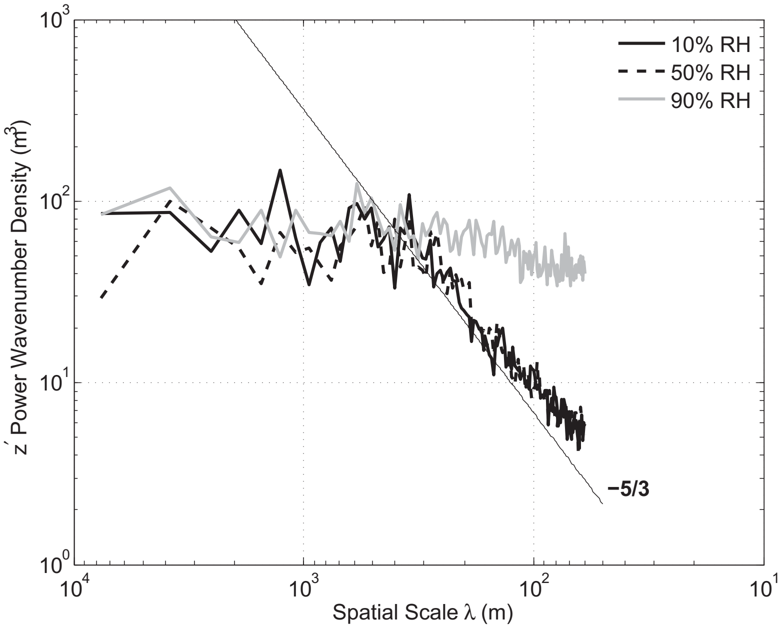

Figure 5.7: Power spectra for cloud base height at 3600 s of simulation

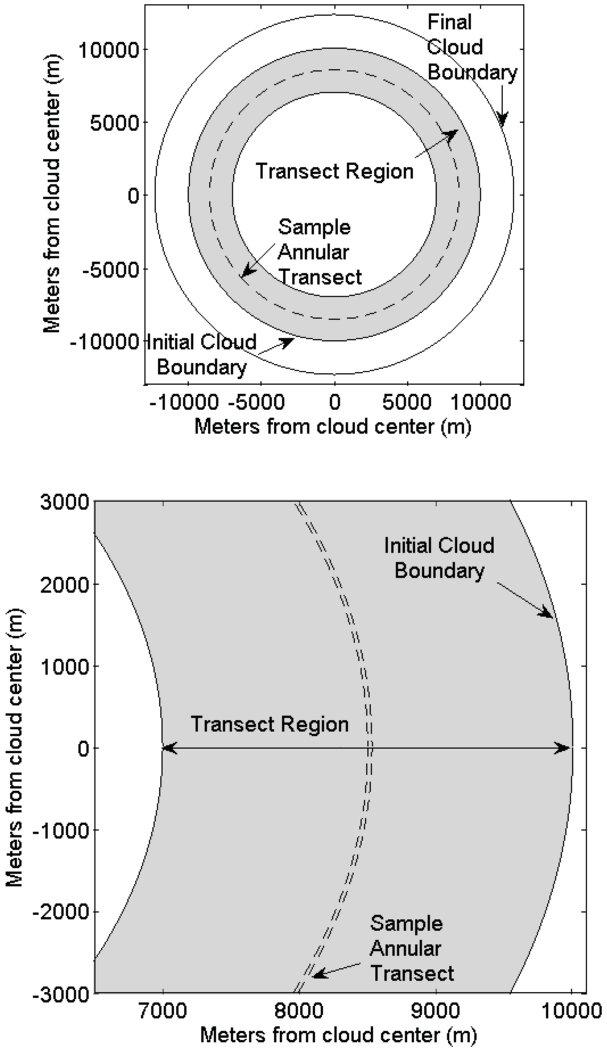

Figure 5.8: Diagram of cloud transect region for FT calculations and close up detail

The 90% RH_{LT} case shows significantly more variance at smaller spatial scales than the other two cases. This indicates that the convective motion at the base of the cloud, which is influenced directly by the cloud base heating, is significantly lessened in its size of overturning currents, i.e., the size of the mammatus-like lobes, in the 90% RH_{LT} case as compared to the 10% or 50% RH_{LT} cases. The higher variance of cloud base height at the smaller scales in the 90% RH_{LT} case indicates that the convective motions are small in size, rather than the larger cells of convective overturning seen in the 10% RH_{LT} case that forms mammatus-like features as seen previously in Figures 5.3 and 5.5. The cloud base in the 90% RH_{LT} case, according to the FT plot of cloud base variance seen in Figure 5.7, is smoother than the -5/3 slope of turbulent energy dissipation. The variance is greater in much smaller scales than turbulent energy dissipation, indicating that the convective motions at cloud base are not energetic enough to obey the characteristic -5/3 slope of turbulent energy dissipation. As such, the mammatus-like lobes that form in the 90% RH_{LT} case are significantly smaller than in the other cases.

Cloud base height, however, is only a passive tracer for the energy contained in convection. The mammatus-like lobes are only the visible portion of the downdraft in which they lie. These downdrafts continue downward past where the cloud condensate evaporates. Observations of clouds via aircraft measurements (Squires, 1958), show that these negatively buoyant plumes, referred to as penetrative downdrafts in the paper by Squires, occur and are of significant magnitude.

The source of these downdrafts is not certain however. The most commonly held theory is that mammatus clouds arise from cloud base detrainment instability (CDBI) (Emanuel, 1981), where instability at cloud base is enhanced by evaporative cooling of hydrometeors through entrainment of dry air as the thermal propagates downward. This work suggests that an alternative mechanism for mammatus formation is the radiatively generated instability at cloud base forms circulations in a mixed-layer. The mammatus lobes are the downward branch of these circulations. Evaporative cooling of the downward air parcel through entrainment of dry air may have a role in enhancing mammatus cloud lobes.

5.3.2 Dynamics

Since the thermal plume can extend below cloud base, the analysis of cloud base height could be improved upon by using a similar analysis of the dynamics of the cloud. Figures 5.9, 5.10, and 5.11 show the spectral analysis of the horizontal winds, u and v, as well as the vertical wind, w, of the three simulated mammatus cases. The same transect region previously show in Figure 5.8 used to perform the spectral analysis of the model winds. The transects, however, were taken on a constant 8.8 km height horizontal plane, just below cloud base. This height was chosen so that the horizontal plane of the FT transects would intersect with the negatively buoyant thermal plumes.

Figures 5.9, 5.10, and 5.11 show the power spectra for all the modes of motion in the model. In all directions of motion, the energy at all spatial scales is greatest in the 10% RH_{LT} case, descending according to increasing relative humidity. This shows that the dynamics of the model at cloud base are directly affected by the lower tropospheric relative humidity. Since radiative heating drives the motion of the cloud, a mitigation of the heating supplied to cloud base would lead to decreased motion in the cloud. This is supported by the plots in Figures 5.9, 5.10, and 5.11. All three modes of motion exhibit the characteristic -5/3 power law that is associated with turbulent mixing. At larger spatial scales, the power spectra fall off below the -5/3 slope. This is due to energy constraints. As the spatial scales be come larger, more and more energy is needed to maintain the -5/3 slope. As energy is only supplied to the cloud through thermal radiation, there is not enough energy available to extend the -5/3 slope to the largest spatial scales. The vertical motion falls off of the -5/3 slope slightly faster than the horizontal motions due to the natural stability of the atmosphere.

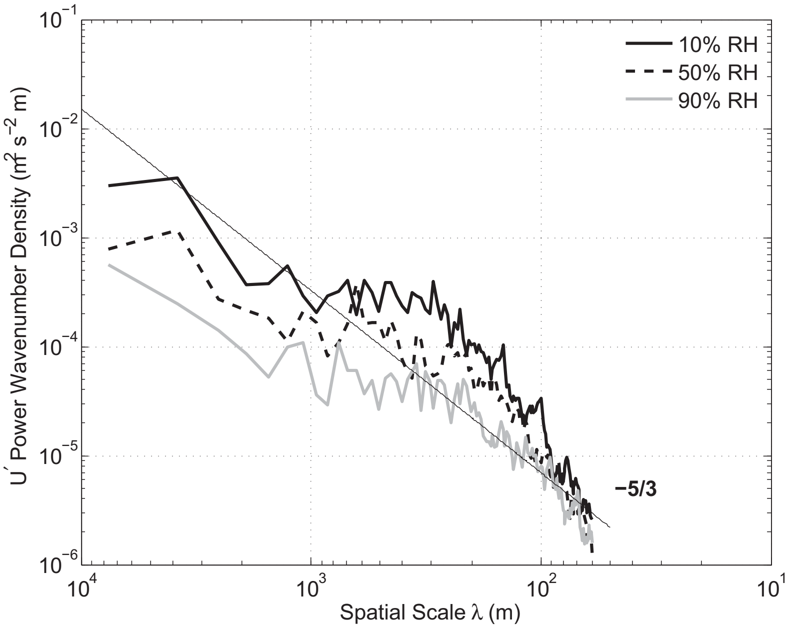

Figure 5.9: Power spectra for model dynamics at 3600 s of simulation for zonal wind u

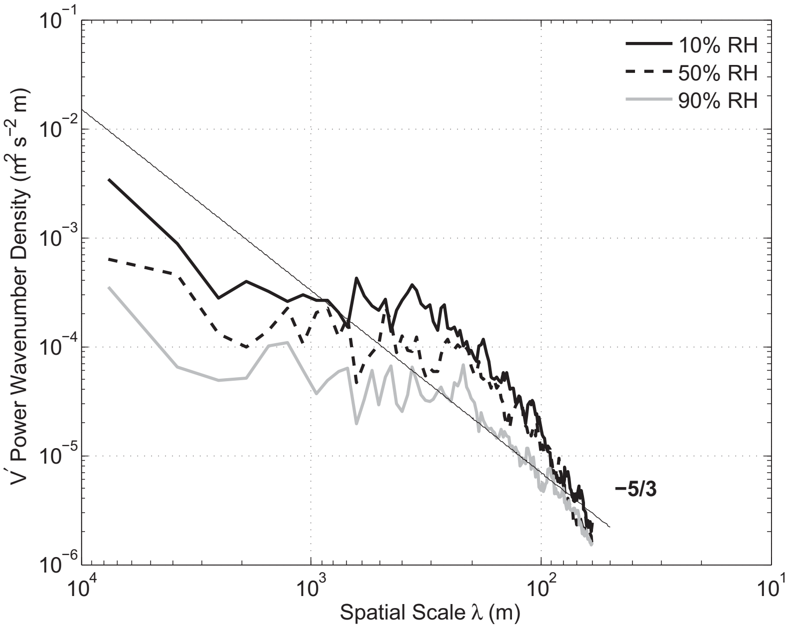

Figure 5.10: Power spectra for model dynamics at 3600 s of simulation for meridional wind w

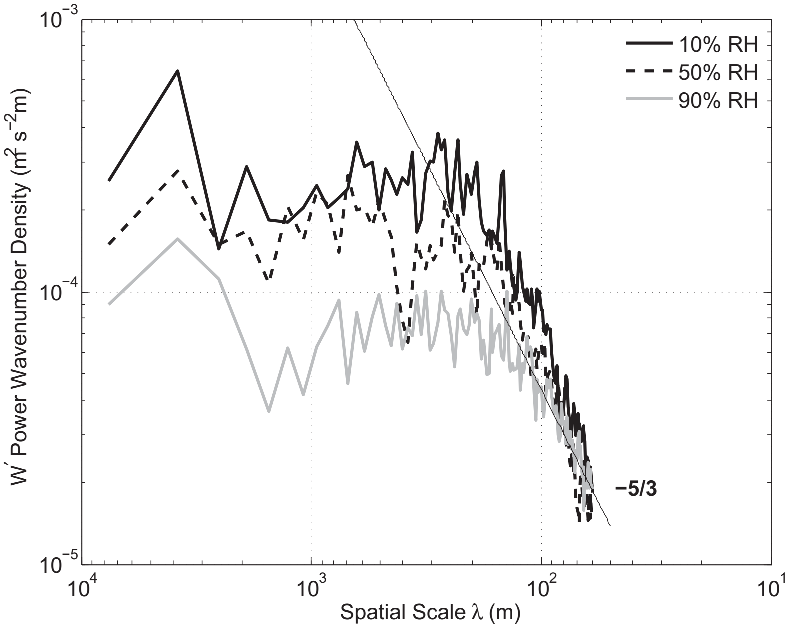

Figure 5.11: Power spectra for model dynamics at 3600 s of simulation for vertical wind w

The stability of the atmosphere acts to dampen vertical motions, thus requiring greater radiative flux convergence to overcome the local static stability. As such, the supplied energy is insufficient to maintain the -5/3 slope in the vertical wind to the same spatial scales as the horizontal wind.

5.3.3 Ice Water Mixing Ratio

Another method of examining the turbulence at cloud base is to examine the concentration of q_i at a particular vertical layer. In areas of updrafts, there will be a lower for ice-water mixing ratio, q_i. This is due to the entrainment of sub-saturated air from the below cloud layer into the cloud through turbulent mixing. Areas where downdrafts occur, relatively higher values of q_i will be present as the unmodified air from the interior of the cloud is advected downward towards cloud base. It should be noted, however, that this air parcel that is advected downward towards the cloud base will also be modified through turbulent entrainment as well. The downward moving air parcel will entrain the lower values of q_i in the surrounding cloud layer, but as it started from a high value, the depression of q_i will be less than in the updraft due to the mixing with saturated, cloudy air parcels, rather than the subsaturated below cloud air.

Figure 5.12 shows a power spectrum of q_i values at a particular vertical level. As in previous sections, the transects used to make the power spectrum plot for q_i are circular, in a radial band between 7000 m and 10,000 m from cloud center. However, the vertical level used in the calculations for Figure 5.12 is at an elevation of 9247 m above the model surface. The vertical level needed to be increased due to the shape of the cloud. the bottom edge of the cloud is, on average, a flat surface for most of its extent. However, at the radial edge of the cloud, the base curves upward (see 3D figures in Appendix B). In order for the radial transects to all be on the same vertical level and all stay inside the cloud where the values of q_i are nonzero, it was necessary to take the transects at a higher elevation than the previous power spectra plots.

The power spectra in Figure 5.12 shows the characteristic -5/3 power law of all turbulent cascades up to spatial scales on the order of 200m. In general, the 10% RH_{LT} case has more variance at a given spatial scale than the 50% RH_{LT} case, which has more variance at a given spatial scale than the 90% RH_{LT} case. This is a reflection of the greater energy

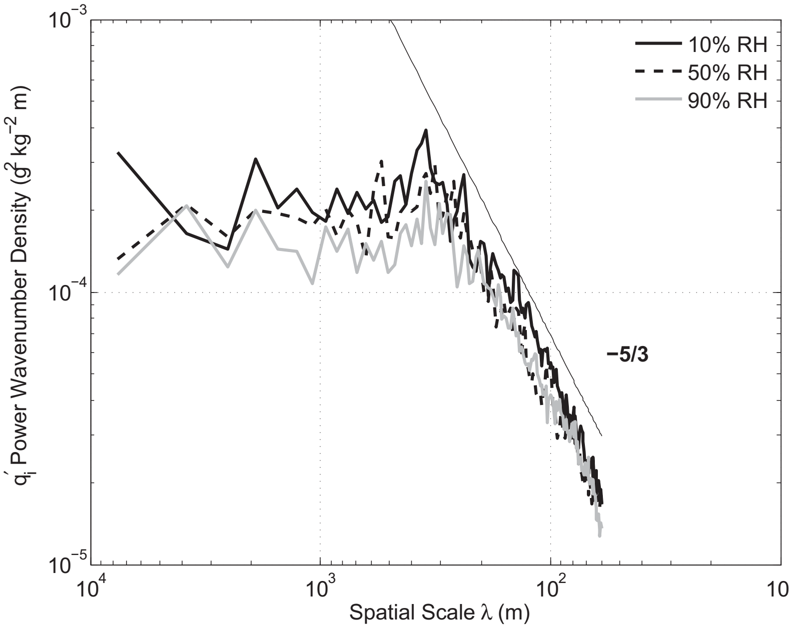

Figure 5.12: Power spectra for ice water mixing ratio q_i at $z = 9,246.6$ m at 3600 s of simulation

deposition in the lower relative humidity cases. On scales larger than 200 m, the power spectrum is, on average, maintained at a constant level. There is, however, a peak in the plot at roughly 300-400 m. This feature can be seen in all three cases, but is most easily picked out in the 10% RH_{LT} case. This indicates that there are structures in the cloud that have a rough characteristic scale of 300-400 m in size.

According to similarity theory (Morton et al., 1956), the radius of the plume is related to the height of the plume according to the relation

$$r \sim \alpha h \tag{5.4}$$

where α is factor that is dependent on the type of plume. In a negatively buoyant thermal, such as those that form mammatus clouds, $\alpha \sim 0.25$ (Morton et al., 1956). Based on the characteristic horizontal scale of the mammatus lobes determined from the peak in the power spectra in Figure 5.12, $r \sim 200$ m. From here, the vertical depth of the plume that created the mammatus lobes can be calculated to be roughly 800 m. These lobe sizes and mixed-layer depths agree with the observed lobe sizes (125 m - 4 km) and mixed-layer depths (~1-3 km) reported in observational studies (Schultz et al., 2006).

The negatively buoyant plumes create turbulent mixing, resulting in a well mixed-layer at cloud base. The calculated scale of the plume extent agrees within an order of magnitude with the scale of the mixed-layer plotted in Figure 5.6. The peak in Figure 5.12 separates two regions of the plot. At scales smaller than the peak, the variance in q_i follows the -5/3 power law closely. This can be attributed to the nature of the mammatus-like features of the cloud. These features are formed through negatively buoyant thermal plumes. Inside plumes, the -5/3 power law of turbulent energy dissipation dominates. At scales larger than the peak, the variance in q_i indicates that the cloud is rougher than the -5/3 turbulent energy dissipation curve, indicating that the thermals themselves are not created by turbulent mixing.

5.4 Cloud Layer Relative Humidity

The analysis of turbulence and formation of mammatus-like structures discussed in previous sections in this chapter led to the hypothesis that the formation of mammatus-like structures in the negatively buoyant thermal plumes might be sensitive to the relative humidity in the layer of the model in which the cloud resides. As discussed at the beginning of this chapter, the relative humidity with respect to ice in the model layer that contains the cloud (a layer between 7.8 km and the top of the model domain labeled RH_{BC} in Figure 5.1) was set to 50% for noncloudy air. During the analysis of the three initial cases, it became clear that this low relative humidity air in the 1km just below the cloud was rapidly evaporating cloud condensate that entered this layer as part of negatively buoyant thermal plumes. Turbulent entrainment of the significantly dryer air from the 1km just below the cloud mixed with the cloudy air from the negatively buoyant thermal plume reducing the relative humidity of the cloudy air to below supersaturation. Once the air drops below supersaturation, the model instantaneously adjusts the cloud condensate to restore saturation by evaporating cloud condensate (Zulauf, 2001). If there is not enough cloud condensate to restore saturation, the model instantaneously evaporates all the cloud at that grid-point.

In reality, it is unlikely that there would be a cloud contained in such dry air. Aircraft measurements of relative humidity with respect to ice have found that in the clear air near cirrus clouds, while widely variable, relative humidity with respect to ice regularly exceeds the 50% value used in the previous simulations and can even exceed saturation (Ovarlez et al., 2002). Given this, another set of model simulations was conducted to examine the sensitivity of the formation of the mammatus-like lobes to the relative humidity with respect to ice in the air just below cloud base. These simulations set RH_{LT} to either 10% or 90% (matching the 10% and 90% RH_{LT} cases discussed previously), and the relative humidity with respect to ice in the layer surrounding the cloud, RH_{BC}, was set to 90%. All other model settings and parameters were kept identical. The 50% RH_{LT} case was not rerun with the higher RH_{BC} as it's response would be expected to still fall between the 10% and 90% RH_{LT} cases as seen previously in the analysis of cloud base turbulence.

5.4.1 3D Surfaces

Figure 5.13 shows the 3D surfaces of the simulated cloud with 10% RH_{LT} for both the 50% RH_{BC} case and the 90% RH_{BC} case. The 3D surface for the higher RH_{BC} case shows larger mammatus-like features than the previous, lower RH_{BC} simulation. This is likely due to the decreased evaporation of the lobe in the air immediately surrounding the cloud as is moves below cloud base in the negatively buoyant thermal.

5.4.2 Ice Water Spectra

When comparing the low RH_{BC} case with the high RH_{BC} case, looking at a spectral plot of ice water mixing ratio is useful. The ice water mixing ratio field is particularly useful to examine due to the theoretical effect of the relative humidity with respect to ice. That is, with higher RH_{BC}, a negatively buoyant air parcel will maintain cloud condensate longer than it will in a dryer layer. This should have the effect of making the mammatus-like lobes more pronounced as they do not evaporate as quickly.

Figure 5.14 shows a comparison of the spectral plot of q_i across spatial scales for the 10% RH_{LT} cases. The plot in this figure was generated as discussed previously. The

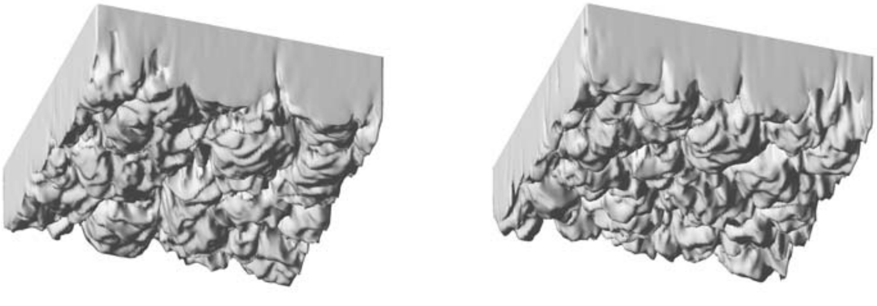

Figure 5.13: 3D plot of simulated cloud with 10% RH_{LT} for 90% RH_{BC} and 10% RH_{BC} at 3600 s

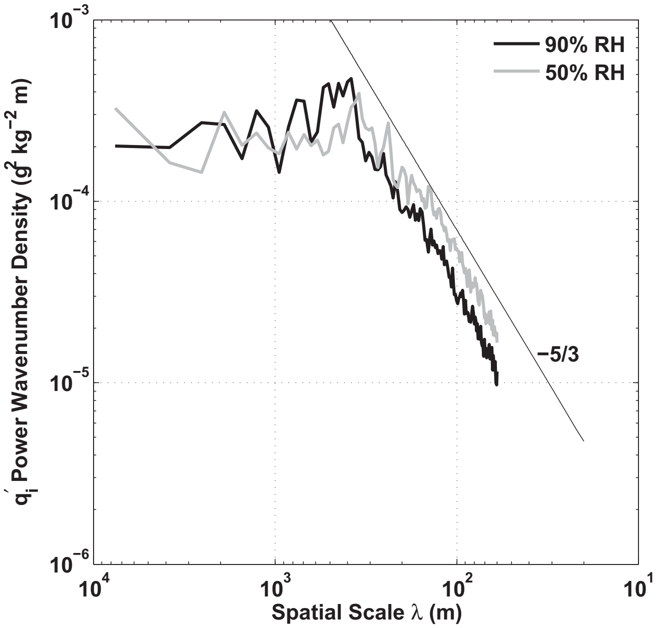

Figure 5.14: Power spectra for ice water mixing ratio q_i at $z = 9,246.6$ m at 3600 s of simulation for 10% RH_{LT} in both cases and 50% or 90% RH_{BC}

characteristic -5/3 power relation is present in both spectral plots, as well as the the same general shape of the plot. There is more variance in the 50% RH_{BC} case at smaller scales than in the 90% RH_{BC} case, as expected. With the lower relative humidity with respect to ice, the downward plumes of the mammatus lobes are eroded more quickly, leading to more variance in spatial scale of the lobes. At scales of approximately 400m there is a sharp increase in variance for the 90% RH_{BC} case. This corresponds to the scale of mammatus-like features seen in the 3D plots. This peak in variance reaches a slightly higher of spatial scale and spans a wider spatial range than in the 50% RH_{BC} case.

The overall response to a change in the cloud layer relative humidity with respect to ice is fairly minimal. The biggest determination in the formation and size of mammatus-like lobes in the simulations seem to be the mitigation of radiative heating at cloud base due to lower troposphere relative humidity with respect to water. However, there are a few considerations regarding this conclusion. It is possible that there is an optimal RH_{BC} that falls between the two scenarios examined in this study. A more thorough sampling of this parameter space would be needed in order to make the determination of what this optimal value might be, if it exists. The second consideration to account for is the fact that due to the nature of the grid spacing and placement of the minimum spacing point, the vertical resolution of the model at cloud base significantly exceeds 30 m. As such, it is possible that the details of the cloud needed to see a difference in mammatus formation due to RH_{BC} are being lost due to the resolution of the model grid spacing.

CHAPTER 6

CONCLUSIONS

The role of radiation in the thermal spectrum in driving cloud evolution has been examined in this work. It has been shown that heating of the cloud base and cooling of the cloud top through radiative processes create temperature gradients that drive cloud motion. These cloud motions form an important part of the evolutionary path of clouds over their lifetime. Through consideration of the dynamics of cloud processes as well as radiative transfer, several rates of cloud evolution modes have been proposed. These evolutionary rates, particularly their dimensionless ratios, can be used to determine how a cloud will evolve over the course of its lifetime.

The numerical simulations conducted in this study attempted to probe the robustness of the derived dimensionless numbers. Through a wide range of cloud size and density, the evolution of the clouds were modeled and compared to the theoretical predictions of the dimensionless numbers for each scenario. The simulated clouds were found to evolve in a manner that was consistent to the expected behaviors based on the dimensionless numbers. The formation of convective mixed-layers and spreading into anvils, laminar vertical motions, and evaporation were all observed in the simulated clouds where predicted by the dimensionless numbers. Clouds that are unstable in nature (tall, narrow clouds with high concentrations of condensed ice) were found to not last long in the numerical simulations as well, validating the model behavior.

The evaluation of the dimensionless numbers through simulation of cloud evolution also provided insight into a particular cloud type. Simulations of large extent and high ice concentration clouds led to the development of mammatus-like features in the simulated cloud. This indicated that mammatus formation can occur solely through radiative processes and can develop from a homogeneous initial cloud, contrary to previous theories (Kanak et al., 2006; Emanuel, 1981; Schultz et al., 2006). Previous theories required either inhomogeneous initialized clouds or precipitation to form the lobes of the mammatus clouds. The mammatus formations seen in this study had neither. This led to the formulation of a theory on mammatus formation that depends purely on radiative processes. The theory that below-cloud relative humidity can mediate the cloud base radiative heating from the surface was tested by using identically initialized clouds and varying the relative humidity in the model's lower troposphere. The resulting simulations produced mammatus-like formations in low-relative-humidity environments and suppressed the formation of mammatus-like structures in high-relative-humidity environments. Radiative transfer models produced visible spectrum images of the mammatus-like clouds and the resulting images match well with visual observations of mammatus clouds.

Analysis of cloud base turbulence shows that in the low-below-cloud-base relative humidity cases, there is an increase in turbulent mixing. Cloud base structures are larger, as well as structures in the q_i and wind fields. These structures followed a characteristic -5/3 power law in the size of turbulent eddies indicative of turbulent energy cascades. These energy cascades are the means through which turbulent energy is transferred to smaller scales to the point at which the energy can be dissipated through viscous drag on the flow. The cloud base structure seen in mammatus clouds is a result of this turbulent energy cascades. The negatively buoyant thermal plumes that form mammatus clouds exhibit a particular shape that relates the vertical extent of the plume to the width of the plume. When comparing the depth of the mixed-layer in the model that produces the negatively buoyant thermal plumes to the horizontal size of the mammatus-like features, the ratio of depth to width matches that of observations of mammatus clouds. As a result, it can be stated that the numerical modeling of homogeneous clouds without precipitation can produce mammatus clouds through purely radiatively driven motions.

This work is limited by the simplifications taken. No precipitation was allowed in the simulations. This allowed the cloud to persist longer than normal in situations where precipitation would have been formed. As a sink for cloud mass, precipitation would act to dissipate the cloud. In these simulations, this was not allowed. All simulations were conducted at night. This had the effect of limiting the radiation that the cloud is exposed to to the longwave spectrum. Solar radiation would have the effect of decreasing longwave radiative flux divergence at cloud top by introducing heating. It would also change the geometry of the heating of the cloud. The solar radiation would change direction of incidence as the day progressed, rather than having a constant perpendicular angle of incidence as was in the discussed simulations. No synoptic scale forcings were included in the model for the discussed simulations. As a result, the cloud began its simulation at rest with no vertical motion. This allowed a diagnosis of convective motion that is caused by radiative effects. However, in reality, there are likely background updrafts in the vicinity of clouds. Not accounting for these updrafts would affect the evolution of the clouds in a real environment. Also excluded from this work are areas of vertical wind shear. Wind shear would act to move the cloud top such that it would no longer be co-located with the base of the cloud. This would have the effect of creating a larger surface of the cloud exposed to heating by thermal radiation from the surface, as well as exposing the lower, warmer parts of the cloud to space, allowing for more intense radiative cooling. All of these factors that are not included in the discussed simulations could have significant effects on the evolutionary path of clouds, all of which could be as important as longwave radiation. However, the scope of this work is focused on examining the effects of radiative forcing in the longwave spectrum on cirrus clouds and its role in determining the evolutionary path of the cirrus cloud.

A next step for simulations of this type would be to remove any one of the aforementioned simplifications in order to test the relative magnitude of the radiative effects. To include updrafts or solar spectrum radiation as well as the thermal spectrum radiation would allow a comparison to the effectiveness of each influence on the evolution of the cloud. It would be necessary to include only one at a time in order to attribute any differences in cloud evolution to the inclusion of the particular influence. Once the influence of each particular factor is known, however, it would be possible to combine multiple influences on cloud evolution and determine any possible positive or negative feedbacks on the cloud's evolution.

Other possibilities of continuation of this work include remote sensing of clouds and their environment and subsequent observation in order to determine if they obey the theoretical evolutionary modes described by the dimensionless numbers calculated from the retrieved parameters. This would likely be done through use of one or more of the NASA A-train of satellites currently in orbit. Ideally, a geostationary satellite would be used in order to provide at least semicontinuous observation of a particular cloud. However, retrieval via a geostationary satellite of all of the parameters required to calculate the dimensionless numbers could pose a significant challenge in and of itself.

The recent field campaign, SPartICuS (Small Particles in Cirrus) could provide a means to validate the results presented here. The combined aircraft measurements and ground based measurements of cirrus clouds could provide a sufficient data set to evaluate the results of this thesis in the context of real cirrus clouds.

Another aspect of this thesis that would merit further investigation is the time dependence of S and E as described in Equations 2.57 and 2.62. Tracking these dimensionless numbers as they evolve compared to how the clouds are evolving could provide useful insight. This could also lead to the identification of feedback effects in the evolution of S and E.

APPENDIX A

DIMENSIONLESS NUMBERS

Table A.1: Spreading number S

$S = \frac{\alpha_{strat}}{\alpha_{mix}} = \frac{\mathcal{H}gL}{\theta N^3 h}$	L=100m	1km	10km
q_i=0.01g/kg	1.1×10^{-4}	1.1×10^{-3}	0.011
0.1g/kg	3.3×10^{-3}	0.033	0.33
1g/kg	13	130	1300

Table A.2: Evaporation number E

$E = \frac{\alpha_{evap}}{\alpha_{strat}} = \frac{c_p \theta N^2 h}{g L_s q_i}$	L=100m	1km	10km
q_i=0.01g/kg	150	150	150
0.1g/kg	35	35	35
1g/kg	0.35	0.35	0.35

APPENDIX B

3D FIGURES

This appendix contains 3D plots of all simulated clouds. The figures were made using the Matlab function "isosurface()". Input into this function was the model output ice-water mixing ratio q_i. The function "isosurface()" creates a visualization of a surface of constant value from the input data. In this case the function created surfaces of constant mixing ratio, set to a value of 10% of the value at cloud initialization.

In this appendix, as well as subsequent appendices, the figures corresponding to the simulations with a domain of 100km have been omitted. The values of S for the remaining cases already span a wide range. With the decreased horizontal resolution for the L =100km simulations required for computational speed, these simulations provide no additional insight to the evolution of cirrus clouds. The figures are presented in order of increasing values of S.

B.1 Case 1: $S = 1.1 \times 10^{-4}$, $E = 150$

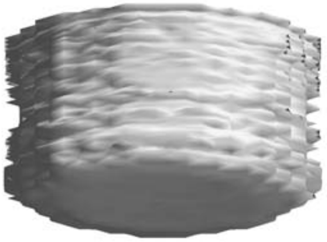

Figure B.1: 3D surface of a cloud with L=100 m and q_i=0.01 g kg^{-1} after 3600 s of simulation

B.2 Case 2: $S = 1.1 \times 10^{-3}$, $E = 150$

Figure B.2: 3D surface of a cloud with L=1 km and q_i=0.01 g kg^{-1} after 3600 s of simulation

B.3 Case 3: $S = 3.3 \times 10^{-3}$, $E = 35$

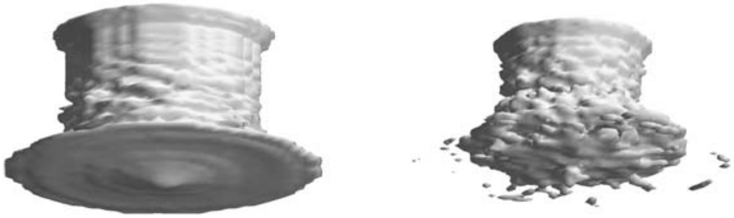

Figure B.3: 3D surface of a cloud with L=100 m and q_i=0.1 g kg^{-1} after 1800 s and 3600 s of simulation

B.4 Case 4: $S = 0.011$, $E = 150$

Figure B.4: 3D surface of a cloud with L=10 km and q_i=0.01 g kg^{-1} after 3600 s of simulation

B.5 Case 5: $S = 0.033$, $E = 35$

Figure B.5: 3D surface of a cloud with L=1 km and q_i=0.1 g kg^{-1} after 3600 s of simulation

B.6 Case 6: $S = 0.33$, $E = 35$

Figure B.6: 3D surface of a cloud with L=10 km and q_i=0.1 g kg^{-1} after 3600 s of simulation

B.7 Case 7: $S = 13$, $E = 0.35$

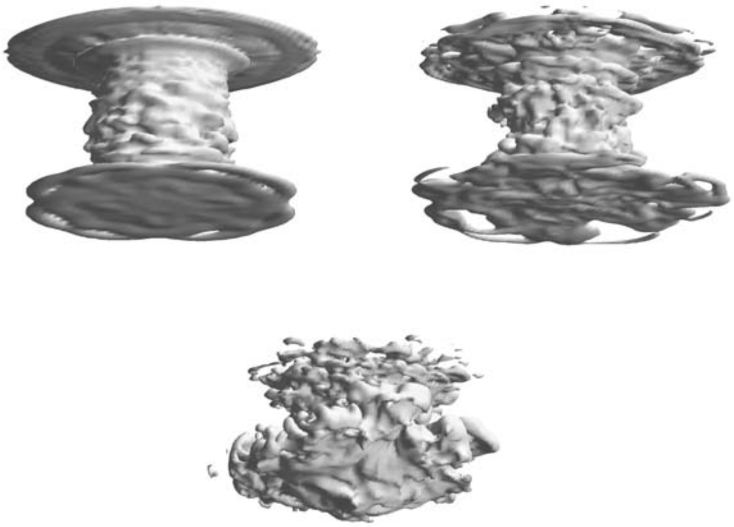

Figure B.7: 3D surface of a cloud with L=100 m and q_i=1 g kg^{-1} after 900 s, 1800 s, and 3600 s of simulation

B.8 Case 8: $S = 130$, $E = 0.35$

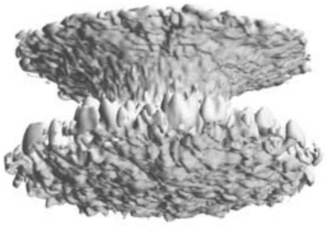

Figure B.8: 3D surface of a cloud with L=1 km and q_i=1 g kg^{-1} after 3600 s of simulation

B.9 **Case 9:** $S = 1300$, $E = 0.35$

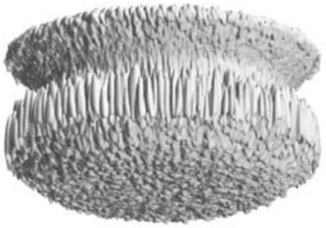

Figure B.9: 3D surface of a cloud with L=10 km and q_i=1 g kg^{-1} after 3600 s of simulation

APPENDIX C

ICE WATER MIXING RATIO CROSS SECTIONS

This appendix contains cross section plots of ice water mixing ratio q_i for all simulated cases. These plots were made by taking a x-z cross section through the exact center of the y-axis of the model output ice water mixing ratio. The value of the mixing ratio is given by the shading of the plot. Areas where no cloud ice was present were set to a value of NaN(not a number) which is plotted as white. Also plotted is the change in ice water mixing ratio over the course of the model simulation. This was calculated by subtracting the initial q_i field from the final, such that $\Delta q_i = q_{i_{final}} - q_{i_{inital}}$

C.1 Case 1: $S = 1.1 \times 10^{-4}$, $E = 150$

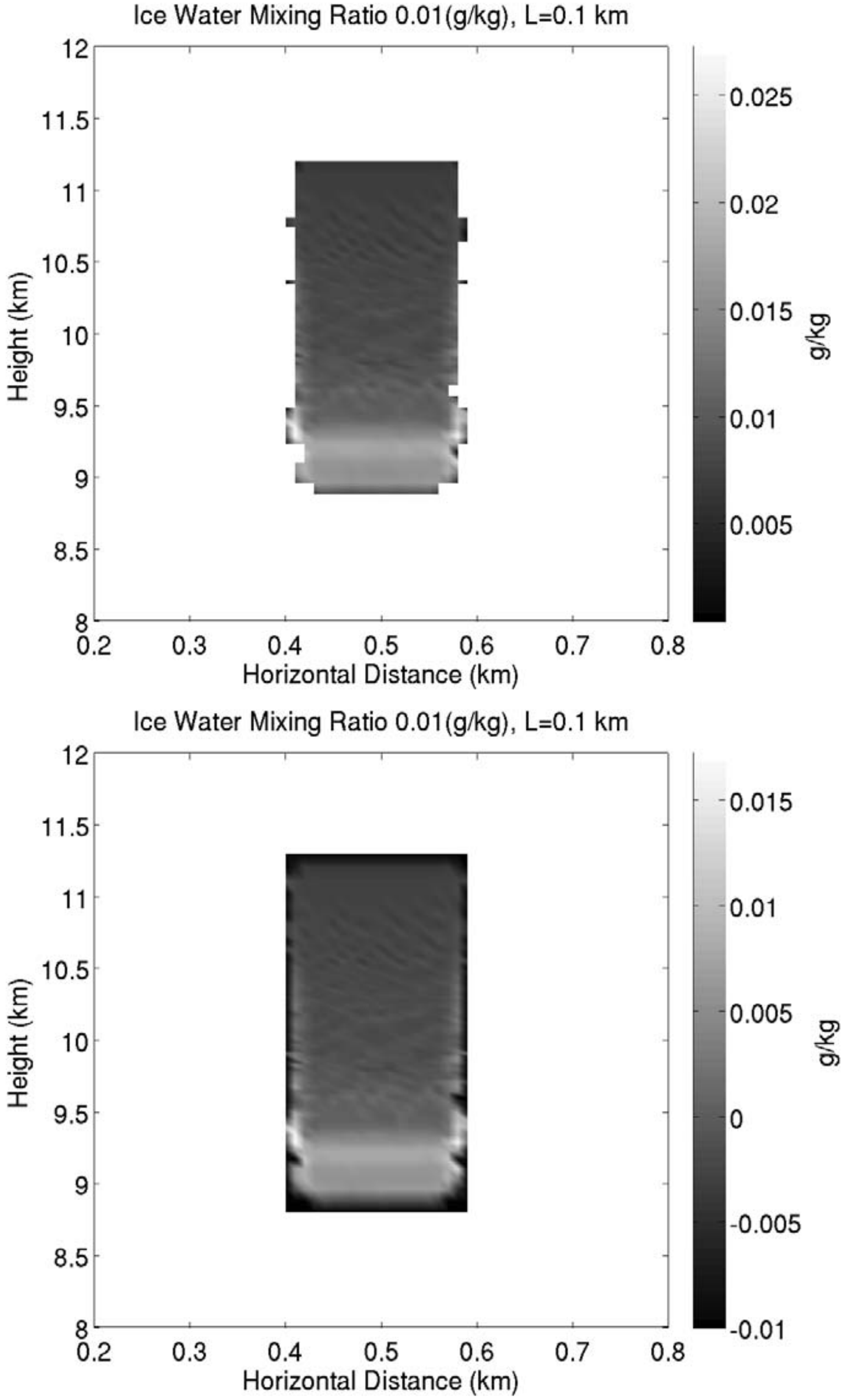

Figure C.1: q_i cross section and differential q_i cross section of a cloud with L=100 m and q_i=0.01 g kg^{-1} after 3600 s of simulation

C.2 Case 2: $S = 1.1 \times 10^{-3}$, $E = 150$

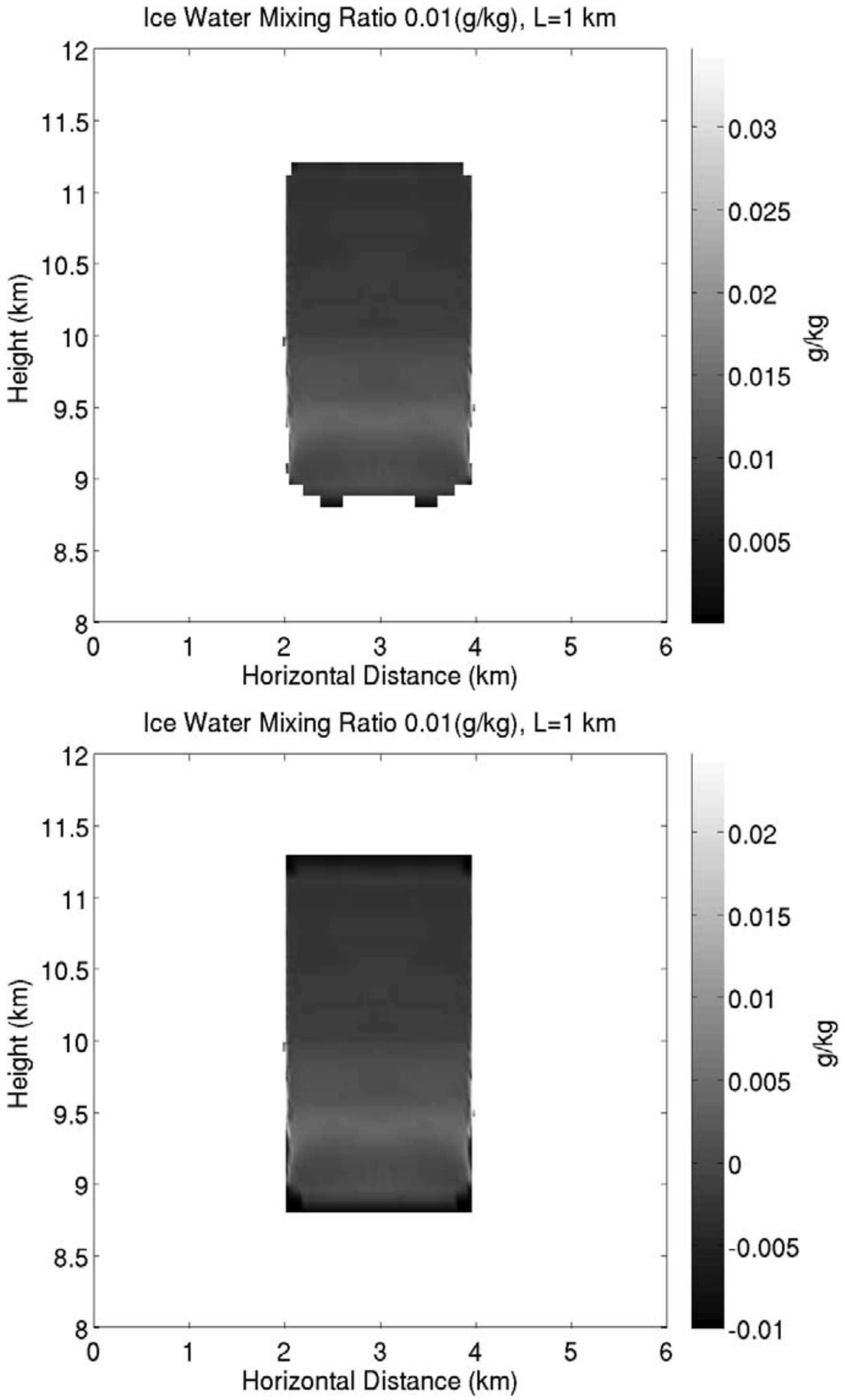

Figure C.2: q_i cross section and differential q_i cross section surface of a cloud with L=1 km and q_i=0.01 g kg^{-1} after 3600 s of simulation

C.3 Case 3: $S = 3.3 \times 10^{-3}$, $E = 35$

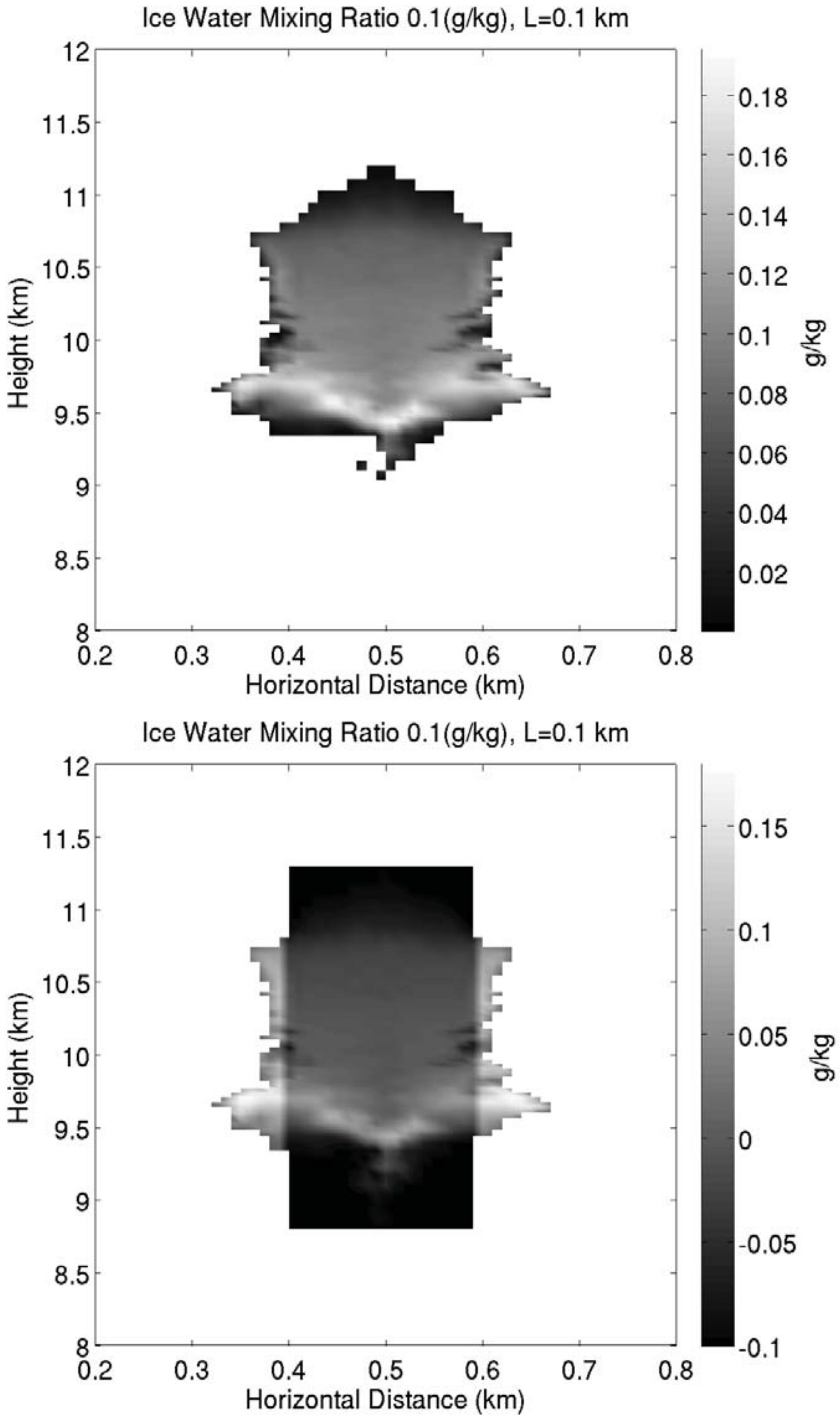

Figure C.3: q_i cross section and differential q_i cross section of a cloud with L=100 m and q_i=0.1 g kg^{-1} after 3600 s of simulation

C.4 Case 4: $S = 0.011$, $E = 150$

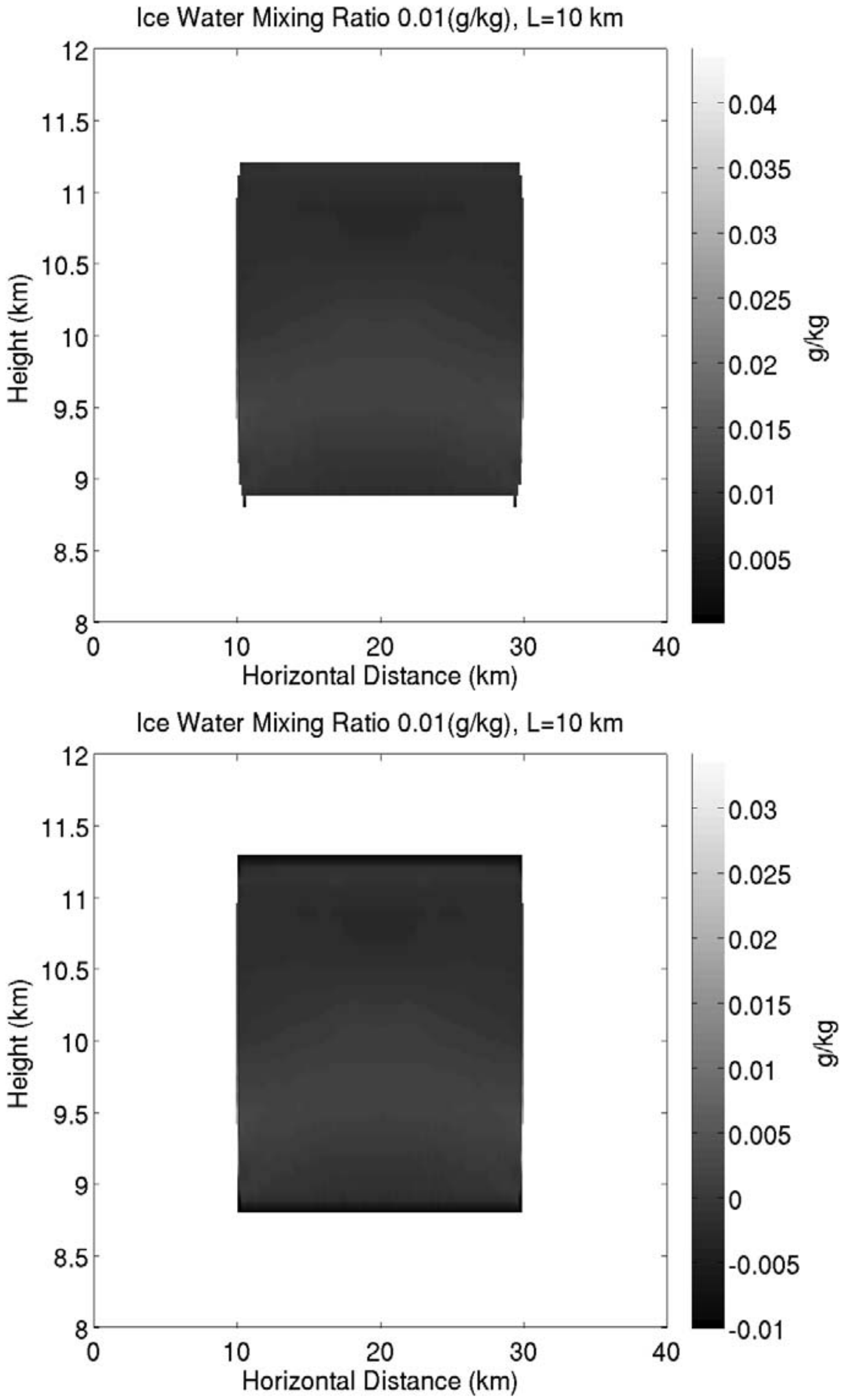

Figure C.4: q_i cross section and differential q_i cross section of a cloud with L=10 km and q_i=0.01 g kg^{-1} after 3600 s of simulation

C.5 Case 5: $S = 0.033$, $E = 35$

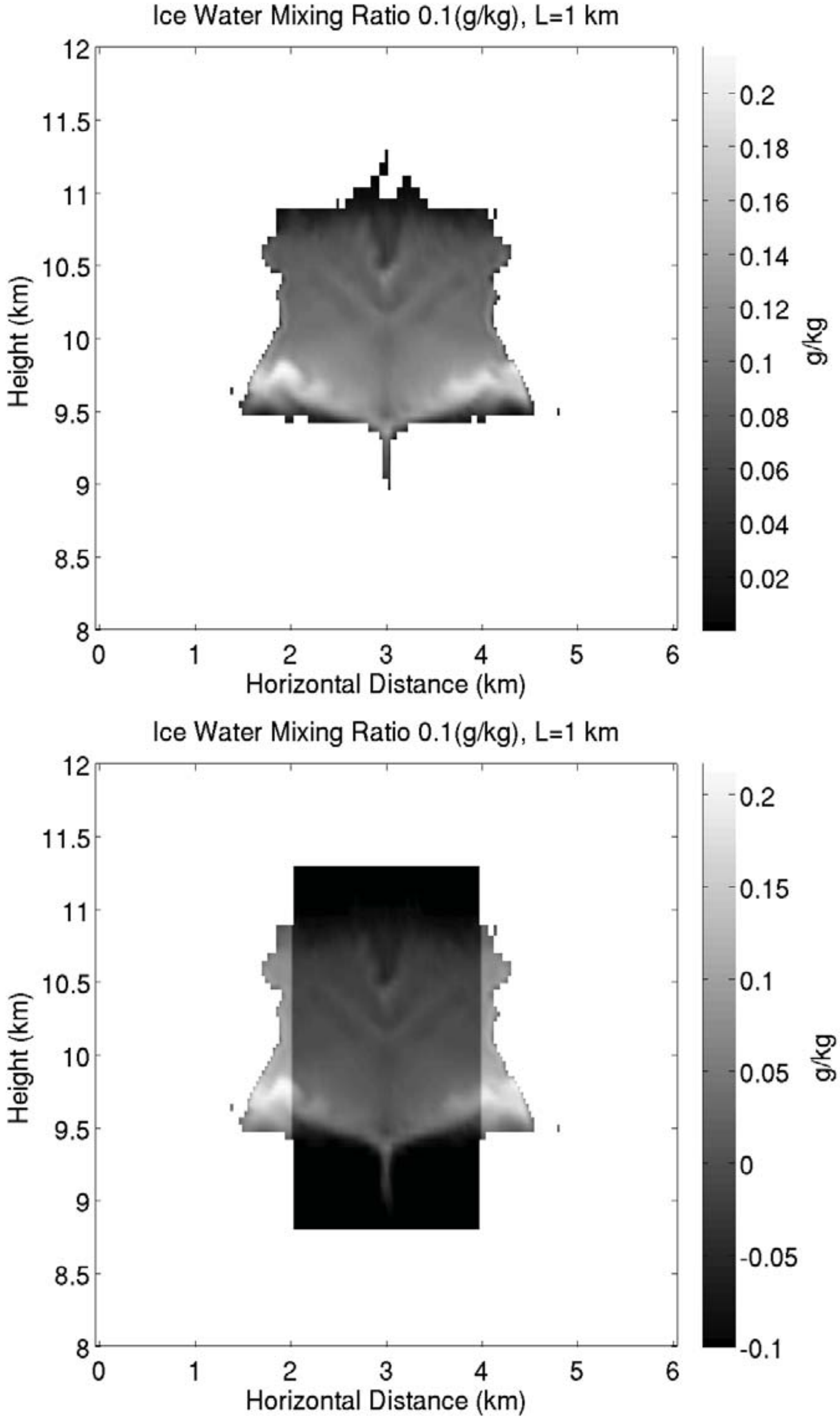

Figure C.5: q_i cross section and differential q_i cross section of a cloud with L=1 km and q_i=0.1 g kg^{-1} after 3600 s of simulation

C.6 Case 6: $S = 0.33$, $E = 35$

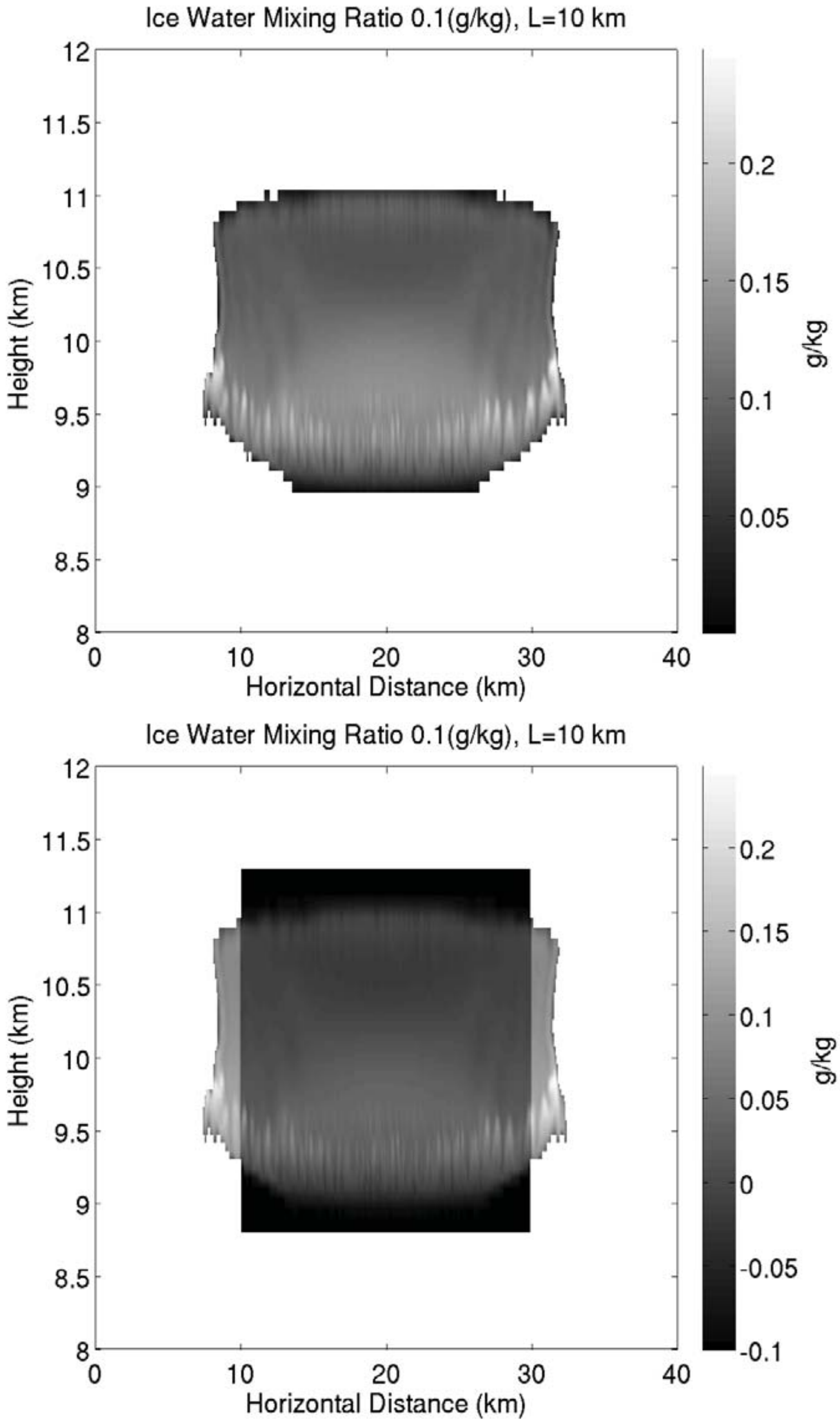

Figure C.6: q_i cross section and differential q_i cross section of a cloud with L=10 km and q_i=0.1 g kg^{-1} after 3600 s of simulation

C.7 Case 7: $S = 13$, $E = 0.35$

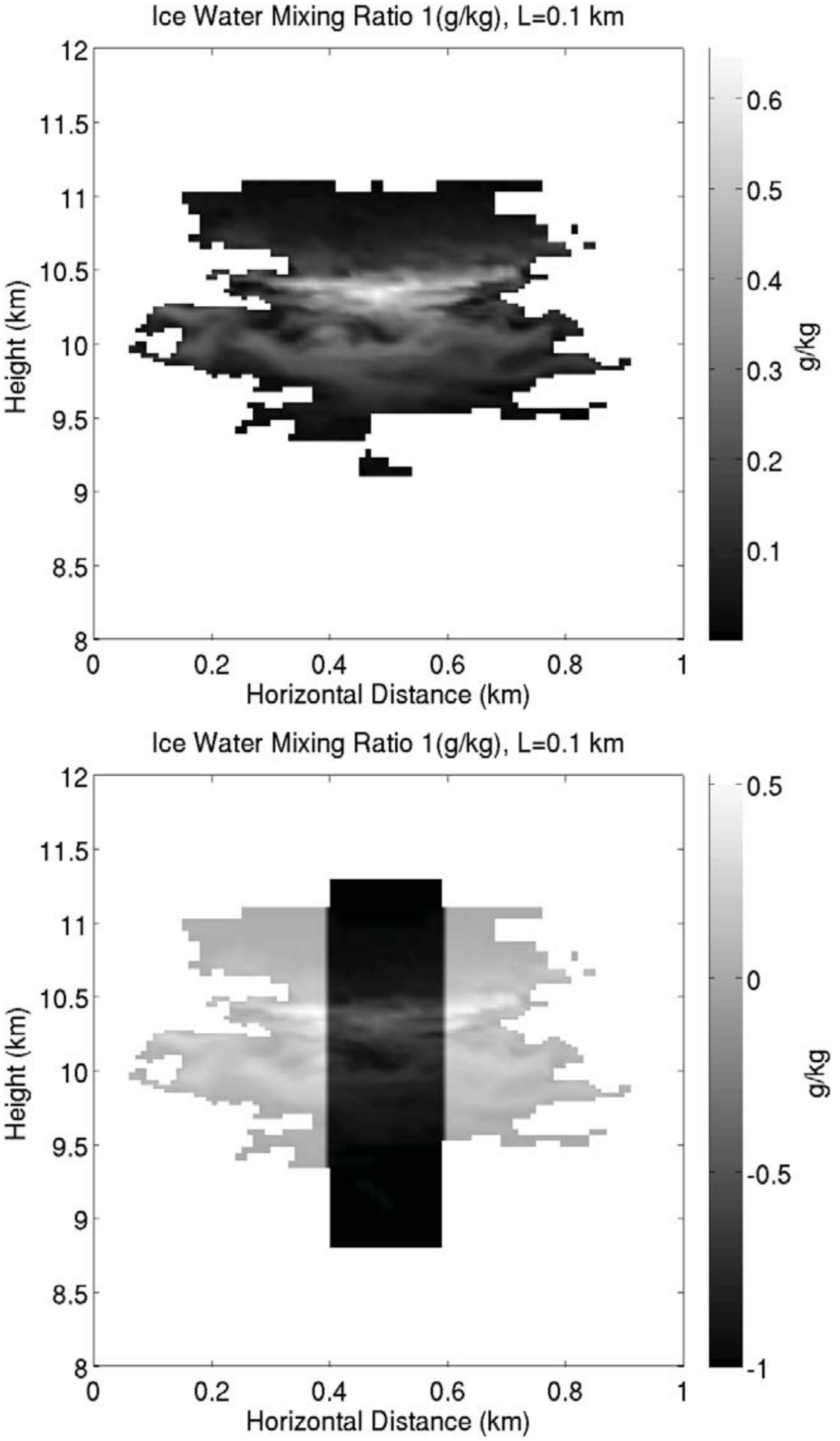

Figure C.7: q_i cross section and differential q_i cross section of a cloud with L=100 m and q_i=1 g kg^{-1} after 3600 s of simulation

C.8 Case 8: $S = 130$, $E = 0.35$

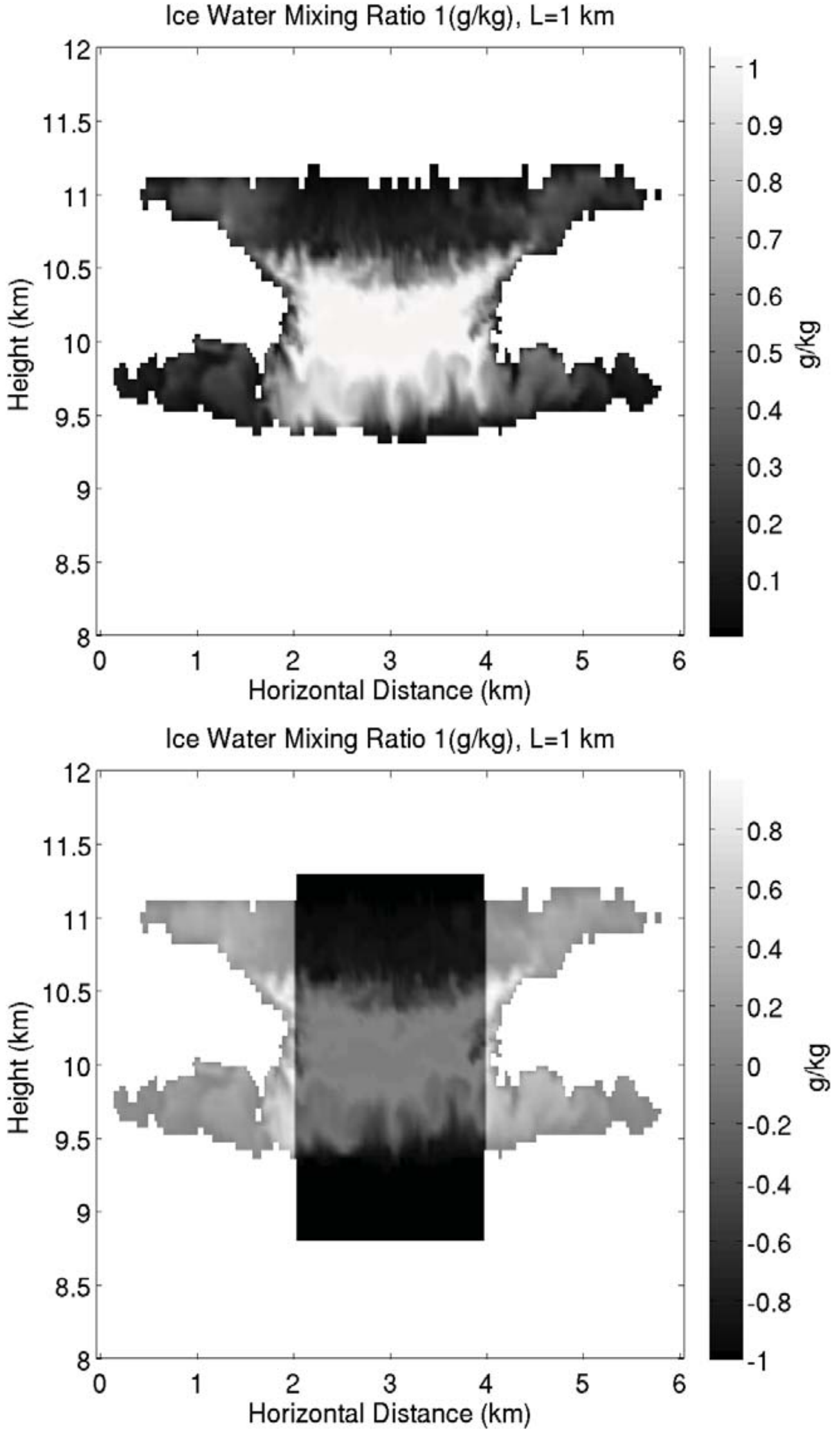

Figure C.8: q_i cross section and differential q_i cross section of a cloud with L=1 km and q_i=1 g kg^{-1} after 3600 s of simulation

C.9 Case 9: $S = 1300$, $E = 0.35$

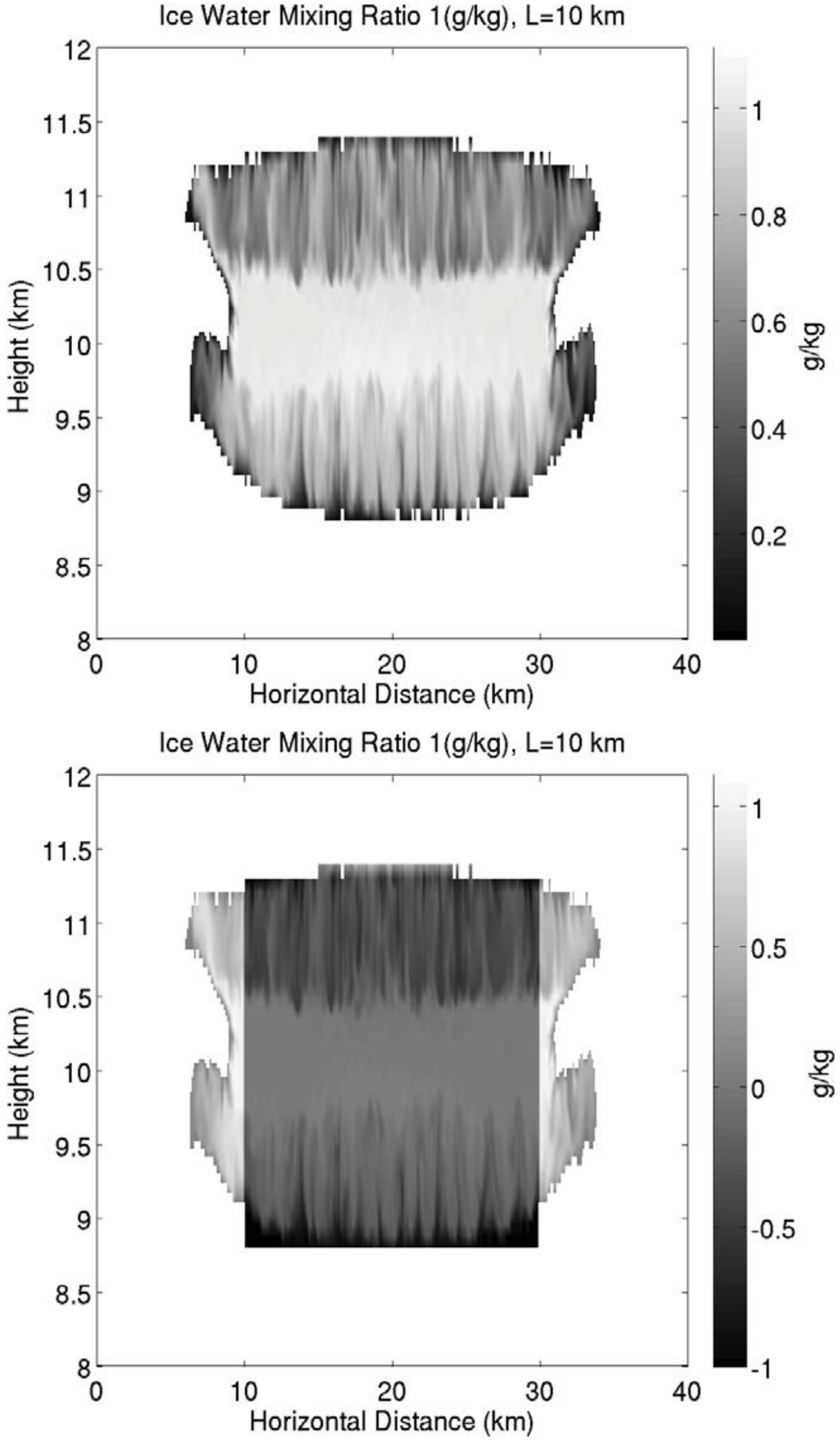

Figure C.9: q_i cross section and differential q_i cross section of a cloud with L=10 km and q_i=1 g kg^{-1} after 3600 s of simulation

APPENDIX D

VIRTUAL POTENTIAL TEMPERATURE VERTICAL PROFILES

Vertical profiles of θ_v can be used to show well mixed-layers. If mixing occurs, the profile of θ_v will remain relatively constant with height, resulting in a layer of neutral buoyancy. If there is no mixing, the θ_v profile will increase with height. The figures in this appendix show the θ_v profile from just below cloud base to just above cloud top for all simulated clouds. The θ_v profile is calculated by calculating θ_v at all grid points and then horizontally averaging all grid points within a certain radius of cloud center at every vertical level. For most cases, this was taken as 90% of L for that case. For cases where L=100km, the number of grid points became so large as to be computationally slow to find all the grid points within 90% of L. For speed of computation, cases where L=100k, only grid points within 50% of L from cloud center were used in the averaging.

For all plots, the initial θ_v profile is plotted in a dashed line. The cloud position after 3600s is indicated on the θ_v profile by the thicker line.

D.1 Case 1: $S = 1.1 \times 10^{-4}$, $E = 150$

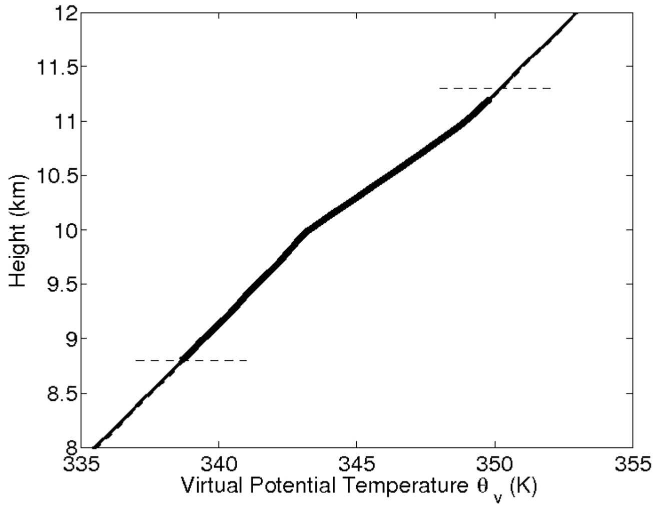

Figure D.1: θ_v profile of a cloud with L=100 m and q_i=0.01 g kg^{-1} after 3600 s of simulation

D.2 Case 2: $S = 1.1 \times 10^{-3}$, $E = 150$

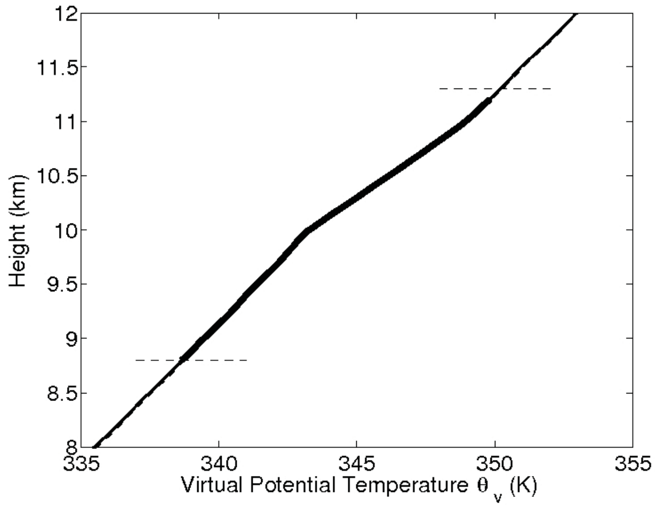

Figure D.2: θ_v profile of a cloud with L=1 km and q_i=0.01 g kg^{-1} after 3600 s of simulation

D.3 Case 3: $S = 3.3 \times 10^{-3}$, $E = 35$

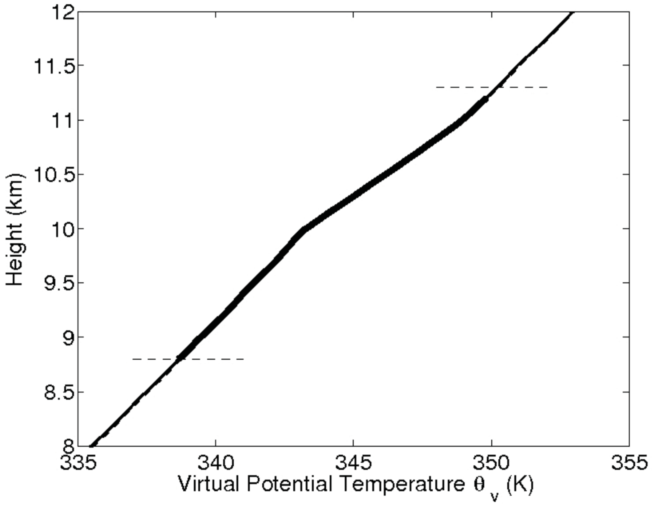

Figure D.3: θ_v profile of a cloud with L=100 m and q_i=0.1 g kg^{-1} after 3600 s of simulation

D.4 Case 4: $S = 0.011$, $E = 150$

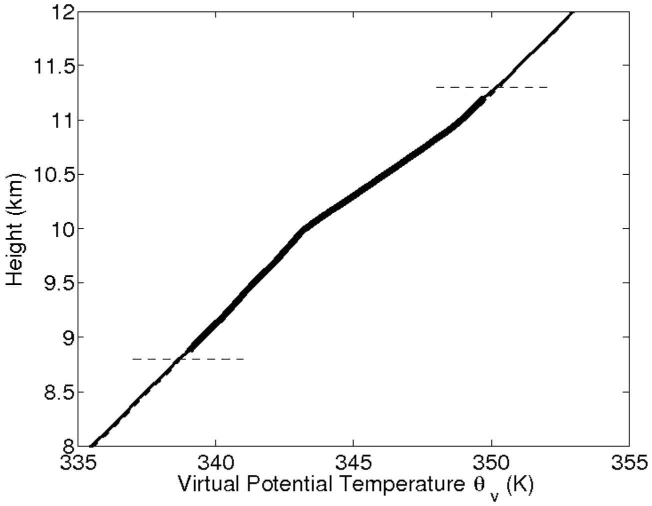

Figure D.4: θ_v profile of a cloud with L=10 km and q_i=0.01 g kg^{-1} after 3600 s of simulation

D.5 Case 5: $S = 0.033$, $E = 35$

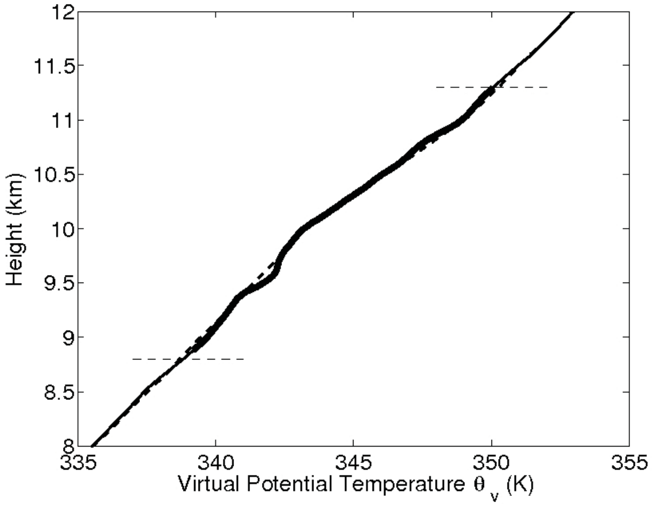

Figure D.5: θ_v profile of a cloud with L=1 km and q_i=0.1 g kg^{-1} after 3600 s of simulation

Although most of the cloud base rises, there is still a narrow central portion of the cloud extending down to near initial cloud base, as seen in the q_i plot for this simulation in Figure C.5.

D.6 Case 6: $S = 0.33$, $E = 35$

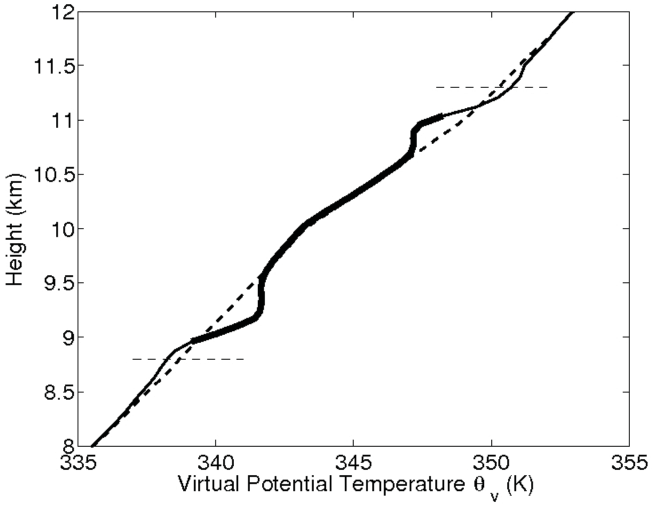

Figure D.6: θ_v profile of a cloud with L=10 km and q_i=0.1 g kg^{-1} after 3600 s of simulation

D.7 Case 7: $S = 13$, $E = 0.35$

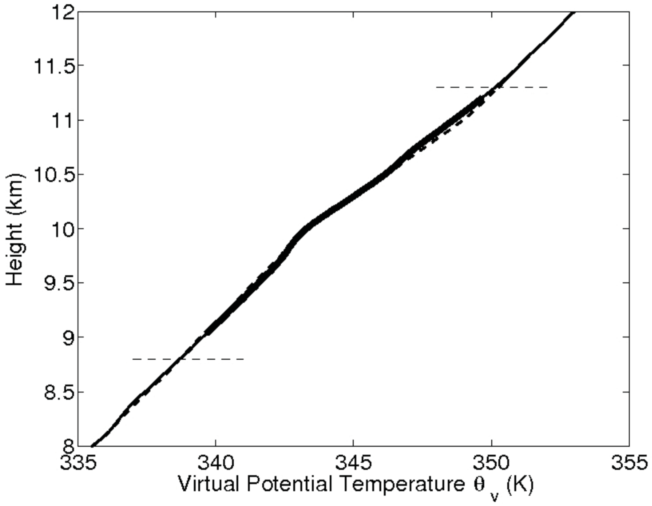

Figure D.7: θ_v profile of a cloud with L=100 m and q_i=1 g kg^{-1} after 3600 s of simulation

D.8 Case 8: $S = 130$, $E = 0.35$

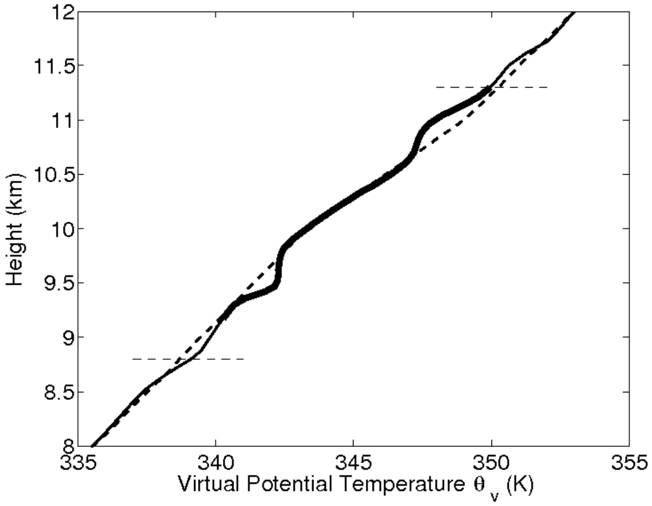

Figure D.8: θ_v profile of a cloud with L=1 km and q_i=1 g kg^{-1} after 3600 s of simulation

D.9 Case 9: $S = 1300$, $E = 0.35$

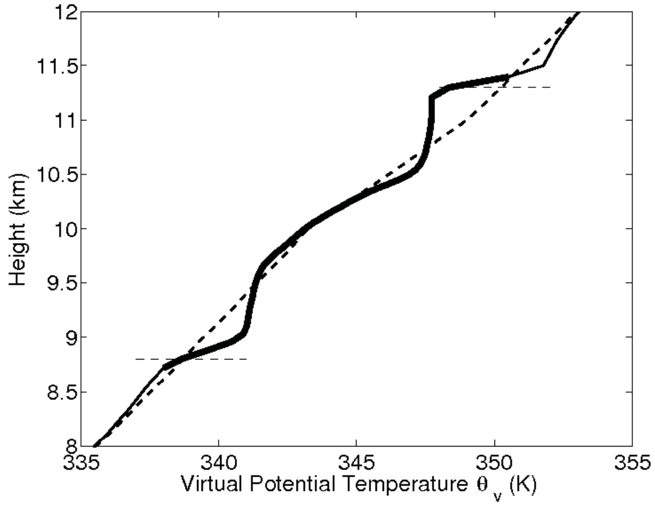

Figure D.9: θ_v profile of a cloud with L=10 km and q_i=1 g kg^{-1} after 3600 s of simulation

APPENDIX E

EQUIVALENT POTENTIAL TEMPERATURE CONTOURS

This appendix contains x-z cross section contours of θ_e taken through the exact middle of the y-axis. θ_e is calculated according to

$$\theta_e = \theta(1 + \frac{L_s q_v}{c_p T}) \tag{E.1}$$

where L_s is the latent heat of sublimation, q_v is the water vapor mixing ratio, and c_p is the specific hear capacity of dry air at constant pressure. The value of latent heat used, L_s, is chosen due to the model constraint that all condensed water present must be in ice form.

It is important to note that in the initial $t = 0s$ plots, the θ_e contours are not horizontal. As the value of q_i increases, the θ_e contours depart farther and farther from horizontal. This is done in the initialization of the model so that the cloudy air maintains neutral buoyancy in the surrounding air. The differential between initial and final states in θ_e is also plotted, defined as $\Delta\theta_e = \theta_{e_{final}} - \theta_{e_{initial}}$. On all plots, the initial cloud boundaries are plotted as a dashed line.

E.1 Case 1: $S = 1.1 \times 10^{-4}$, $E = 150$

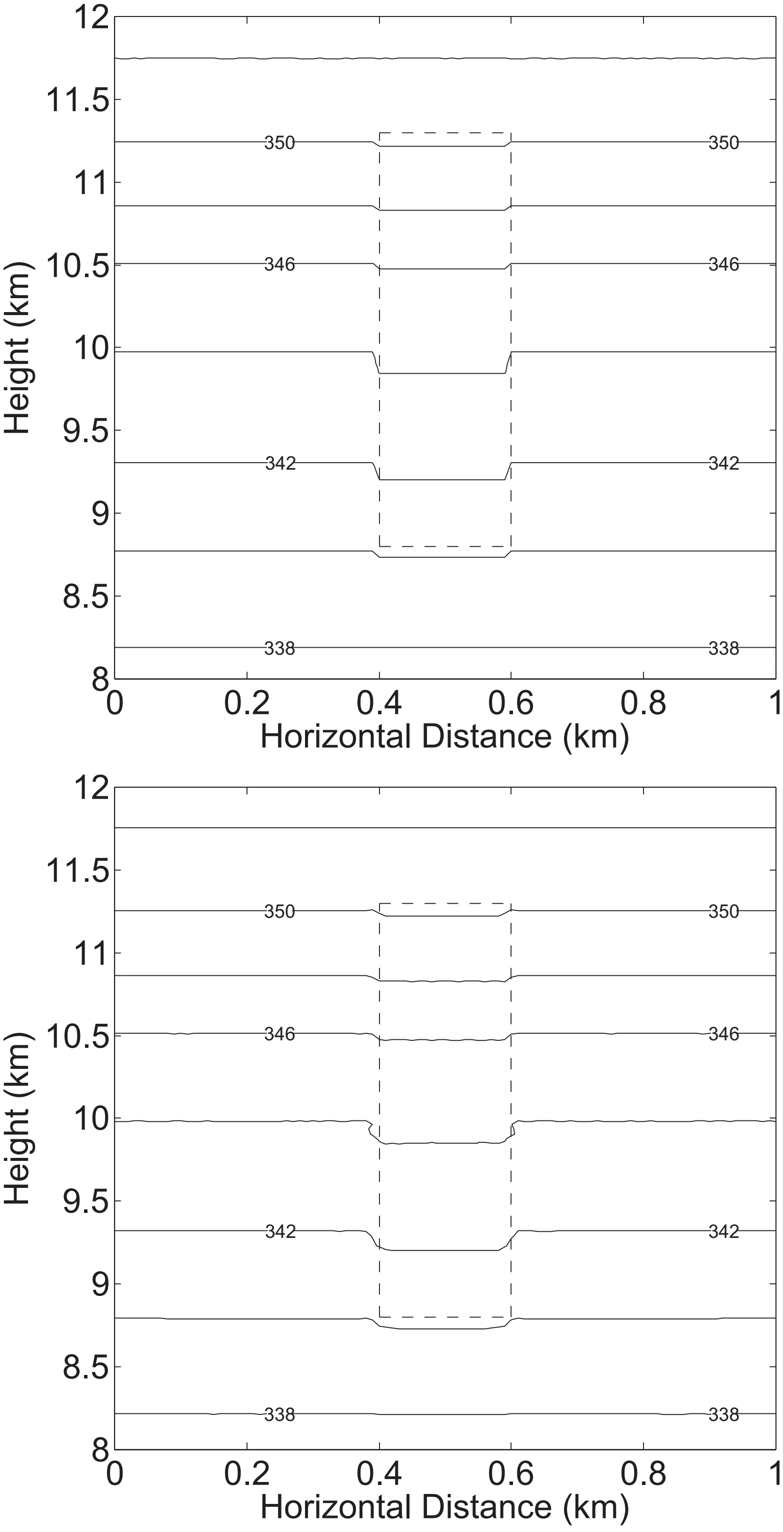

Figure E.1: Cross section of θ_e contours through a cloud with L=100 m and q_i=0.01 g kg^{-1} after 0 s and 3600 s of simulation

E.2 Case 2: $S = 1.1 \times 10^{-3}$, $E = 150$

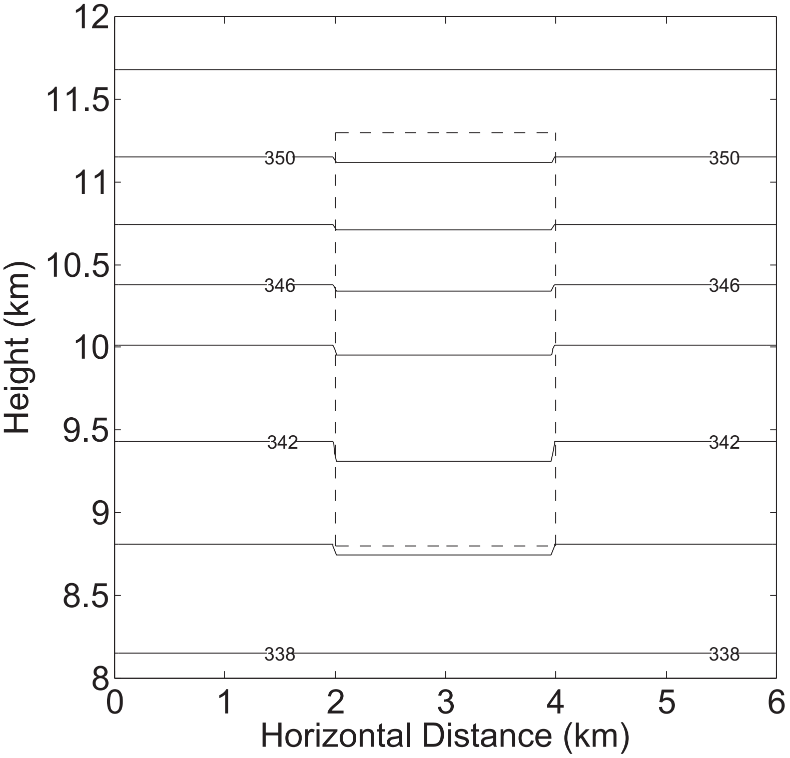

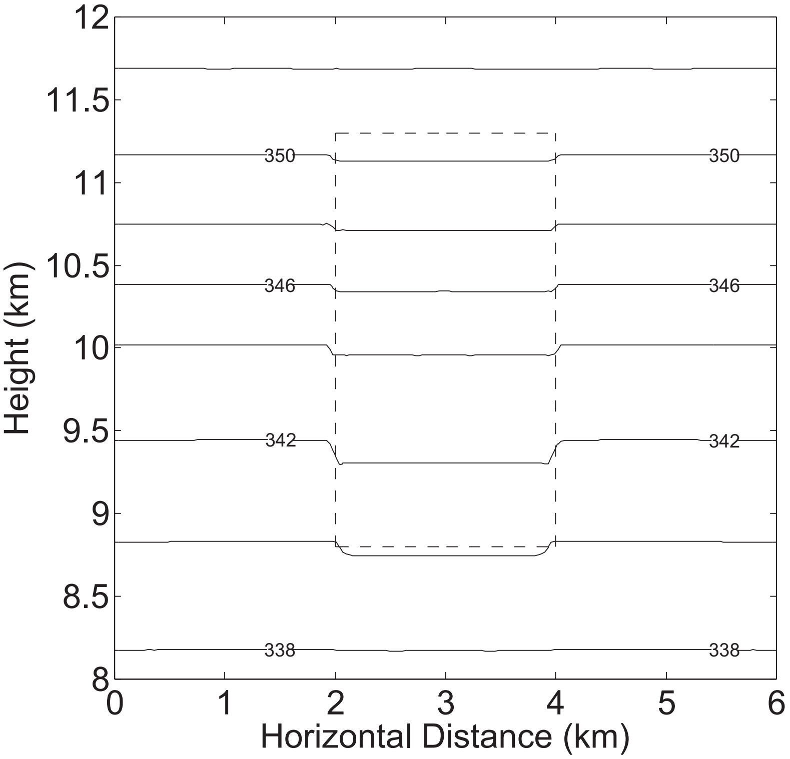

Figure E.2: Cross section of θ_e contours through a cloud with L=1 km and q_i=0.01 g kg^{-1} after 0 s and 3600 s of simulation

E.3 Case 3: $S = 3.3 \times 10^{-3}$, $E = 35$

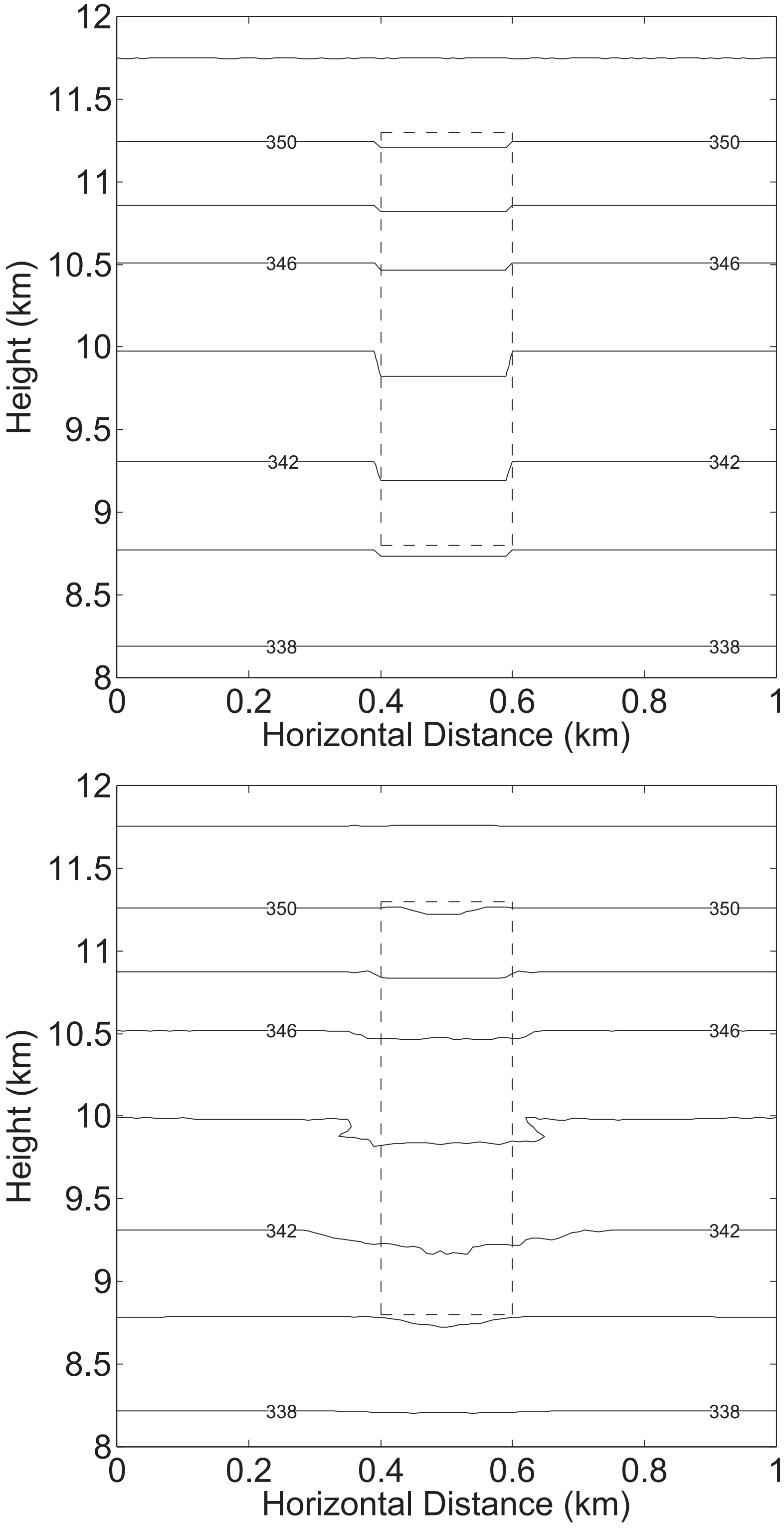

Figure E.3: Cross section of θ_e contours through a cloud with L=100 m and q_i=0.1 g kg^{-1} after 0 s and 3600 s of simulation

E.4 Case 4: $S = 0.011$, $E = 150$

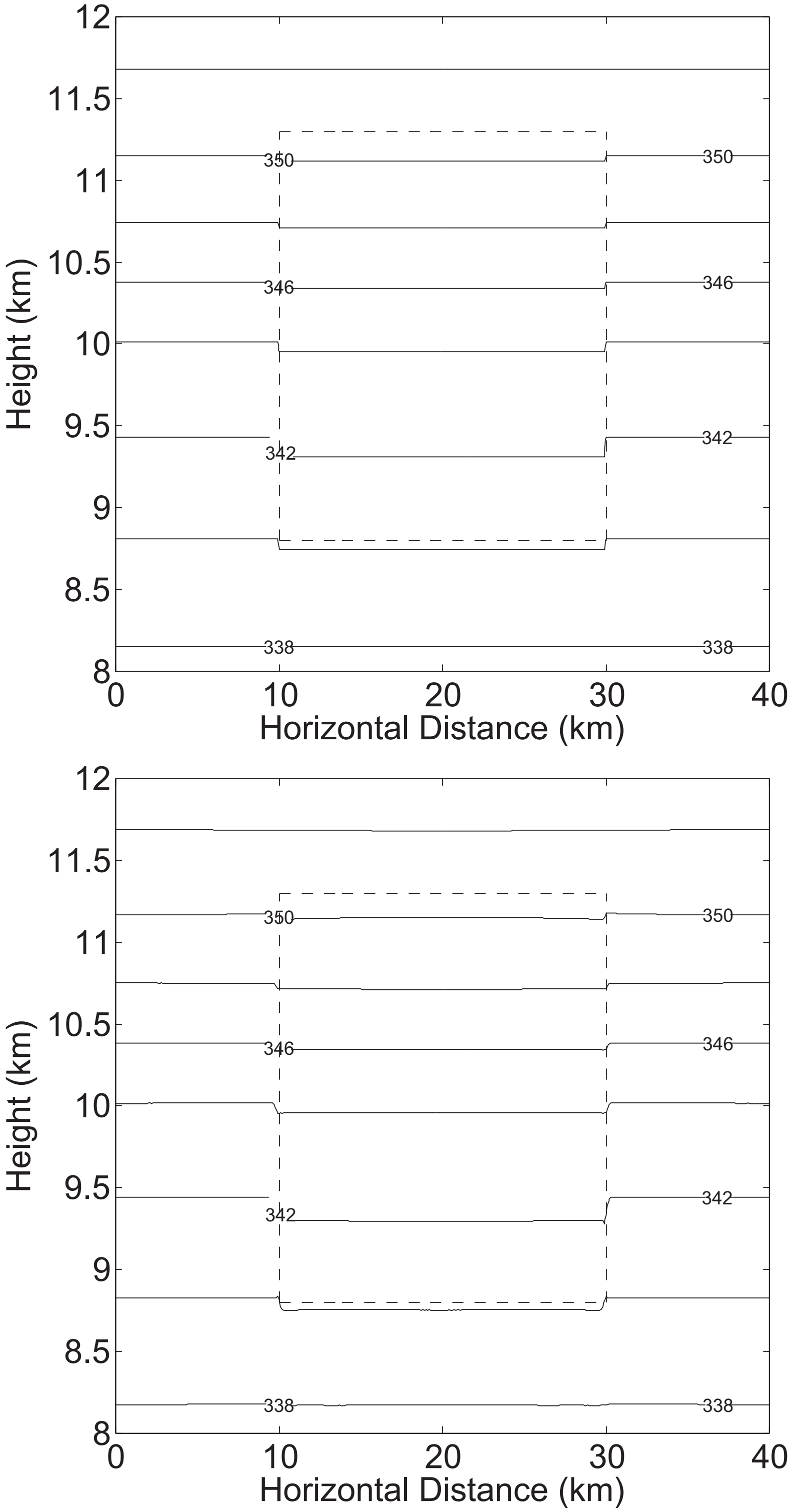

Figure E.4: Cross section of θ_e contours through a cloud with L=10 km and q_i=0.01 g kg^{-1} after 0 s and 3600 s of simulation

E.5 Case 5: $S = 0.033$, $E = 35$

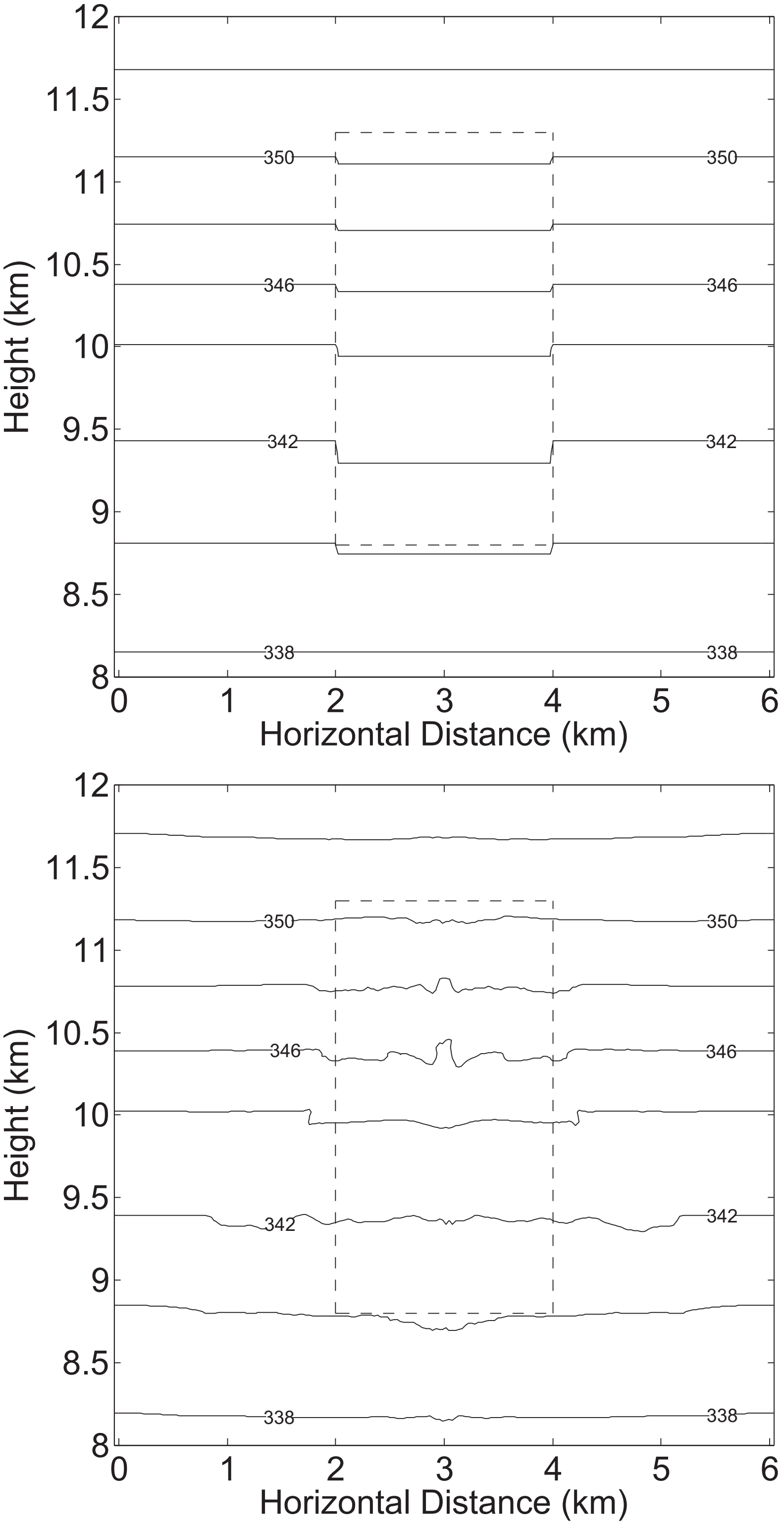

Figure E.5: Cross section of θ_e contours through a cloud with L=1 km and q_i=0.1 g kg^{-1} after 0 s and 3600 s of simulation

E.6 Case 6: $S = 0.33$, $E = 35$

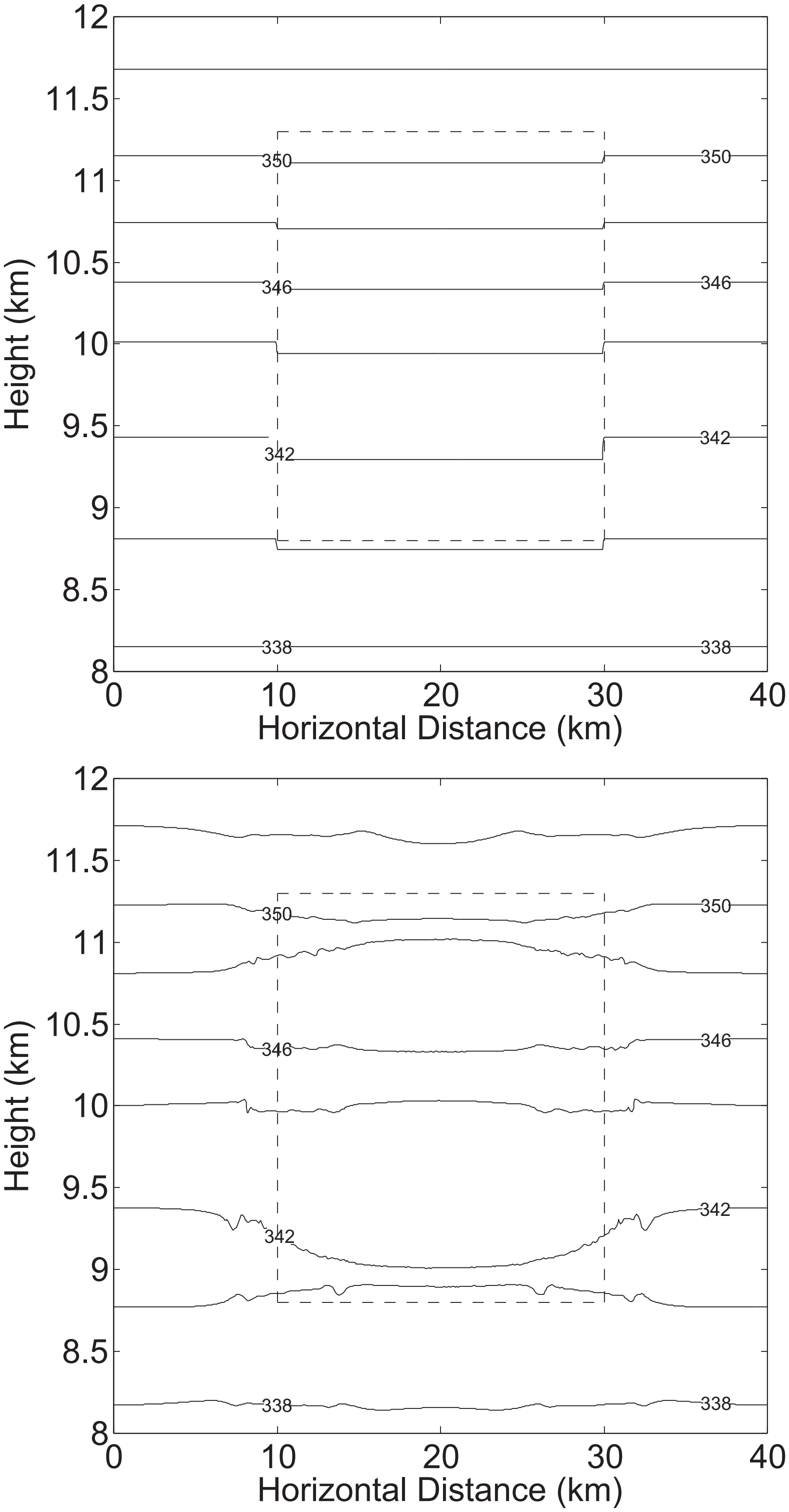

Figure E.6: Cross section of θ_e contours through a cloud with L=10 km and q_i=0.1 g kg^{-1} after 0 s and 3600 s of simulation

E.7 Case 7: $S = 13$, $E = 0.35$

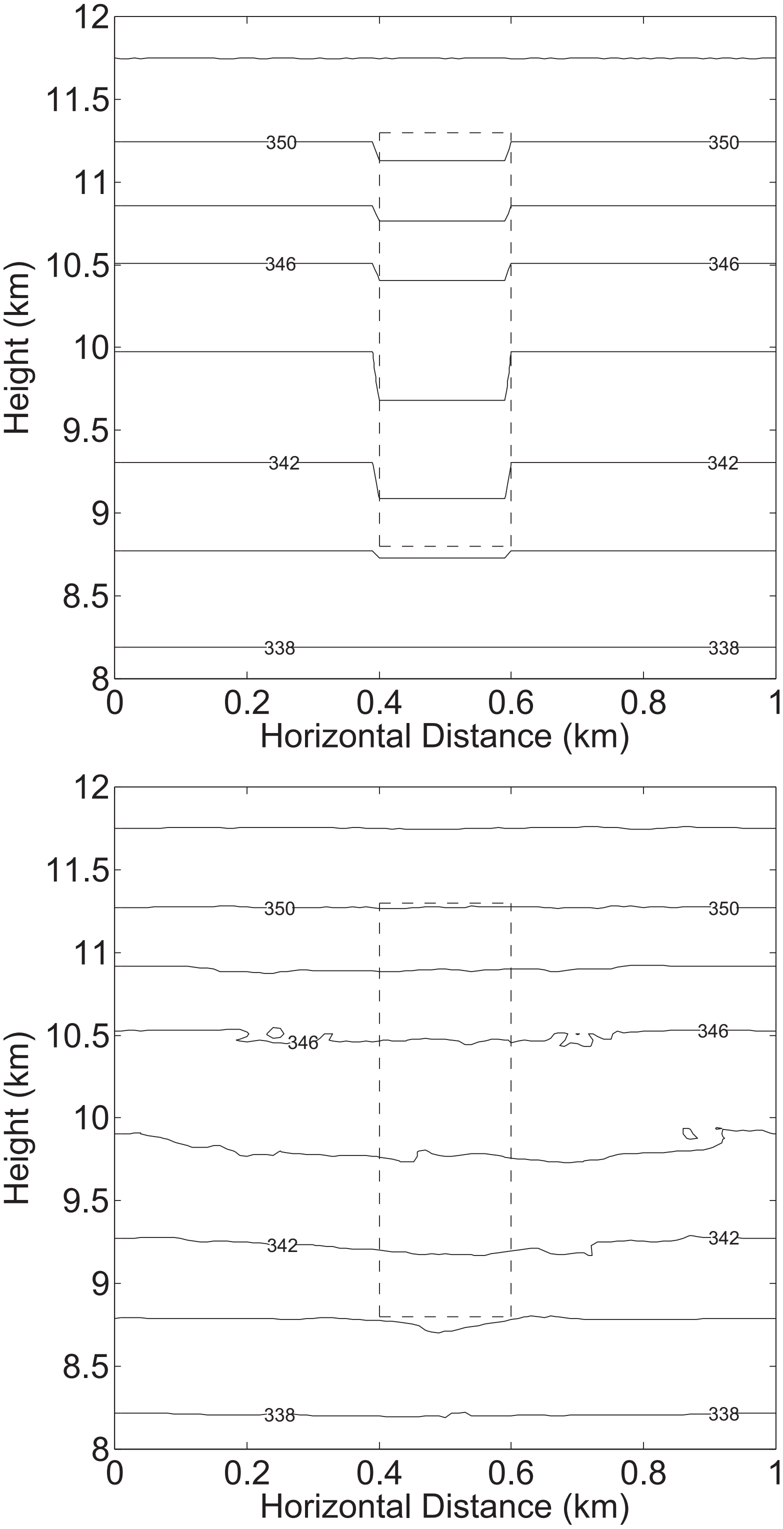

Figure E.7: Cross section of θ_e contours through a cloud with L=100 m and q_i=1 g kg^{-1} after 0 s and 3600 s of simulation

E.8 Case 8: $S = 130$, $E = 0.35$

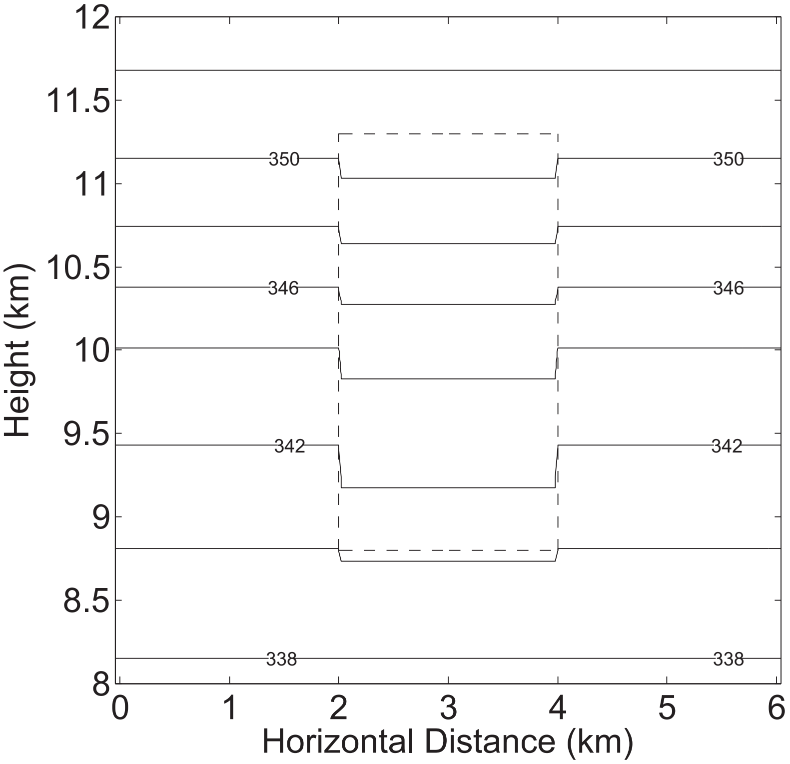

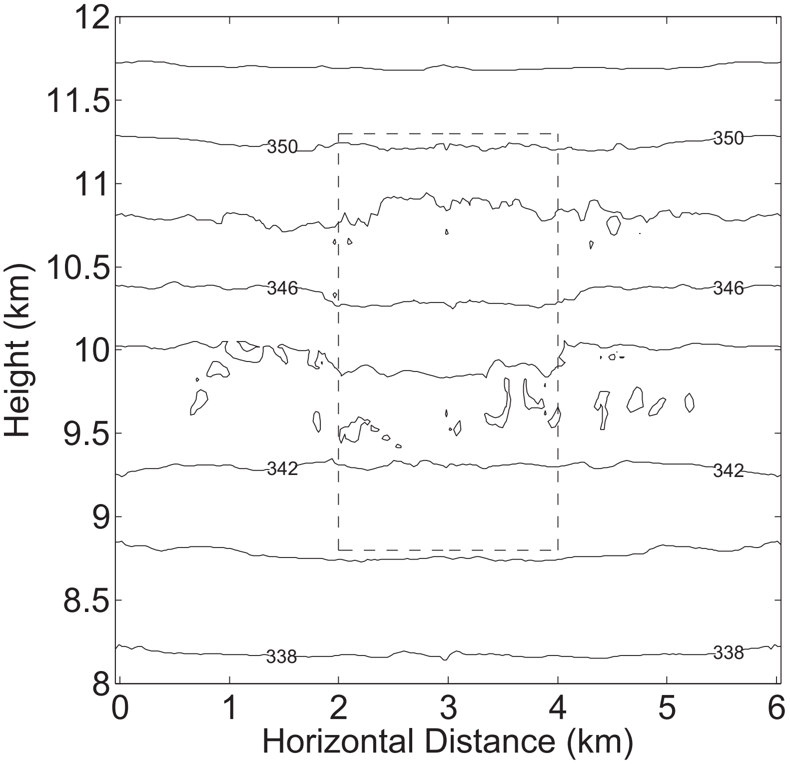

Figure E.8: Cross section of θ_e contours through a cloud with L=1 km and q_i=1 g kg^{-1} after 0 s and 3600 s of simulation

E.9 Case 9: $S = 1300$, $E = 0.35$

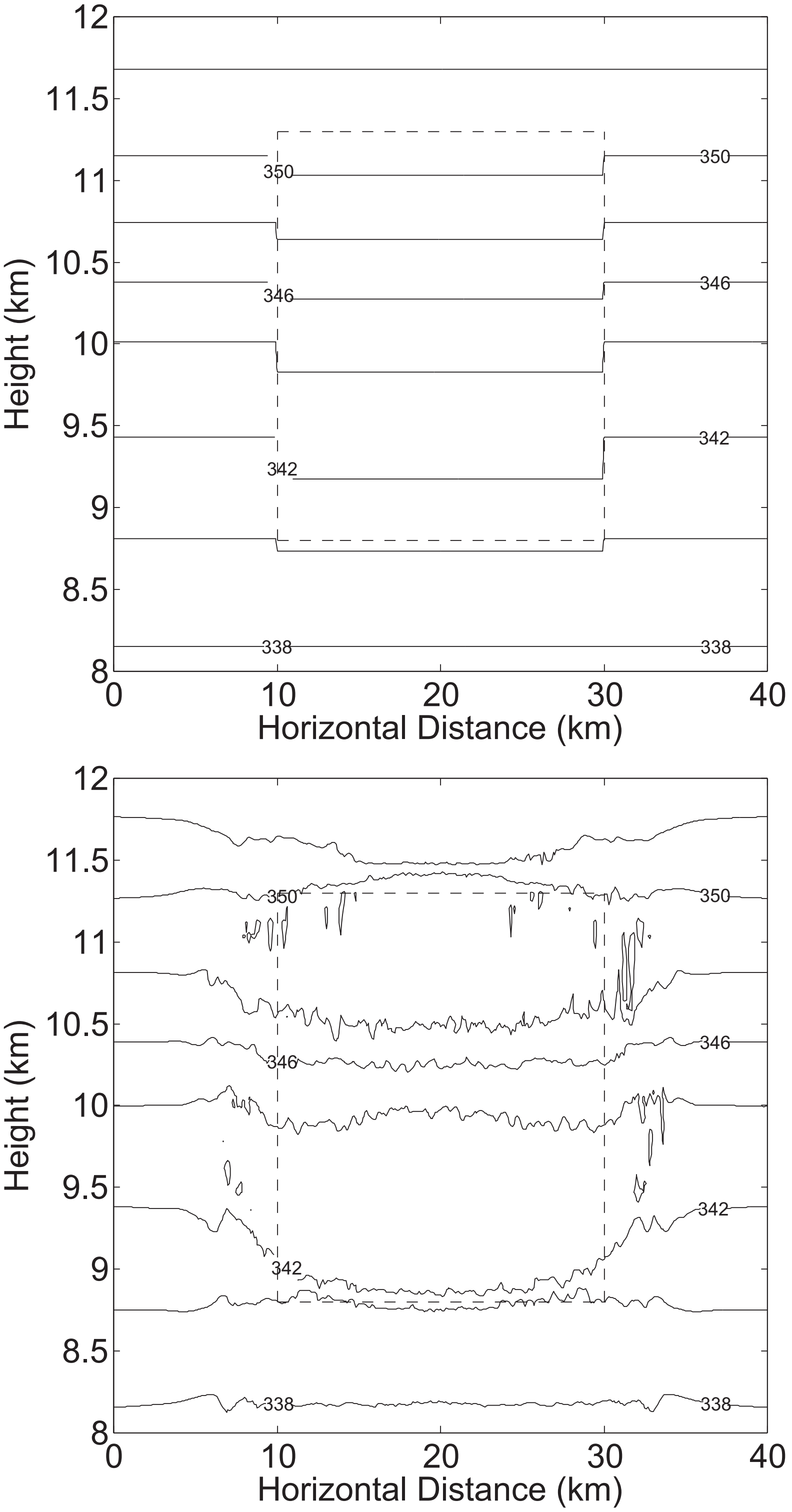

Figure E.9: Cross section of θ_e contours through a cloud with L=10 km and q_i=1 g kg^{-1} after 0 s and 3600 s of simulation

APPENDIX F

VIRTUAL POTENTIAL TEMPERATURE CONTOURS

This appendix contains x-z cross section contours of θ_v taken through the exact middle of the y-axis. θ_v is calculated according to

$$\theta_v = \theta(1 + 0.61q_v - q_i) \tag{F.1}$$

where q_i is the ice water mixing ratio and q_v is the water vapor mixing ratio

It is important to note that in the initial $t = 0s$ plots, the θ_v contours are horizontal for all values of q_i This is done in the initialization of the model so that the cloudy air maintains neutral buoyancy in the surrounding air. The differential between initial and final states in θ_v is also plotted, defined as $\Delta\theta_v = \theta_{v_{final}} - \theta_{v_{initial}}$. The initial cloud boundaries are plotted in dashed lines.

F.1 Initial state

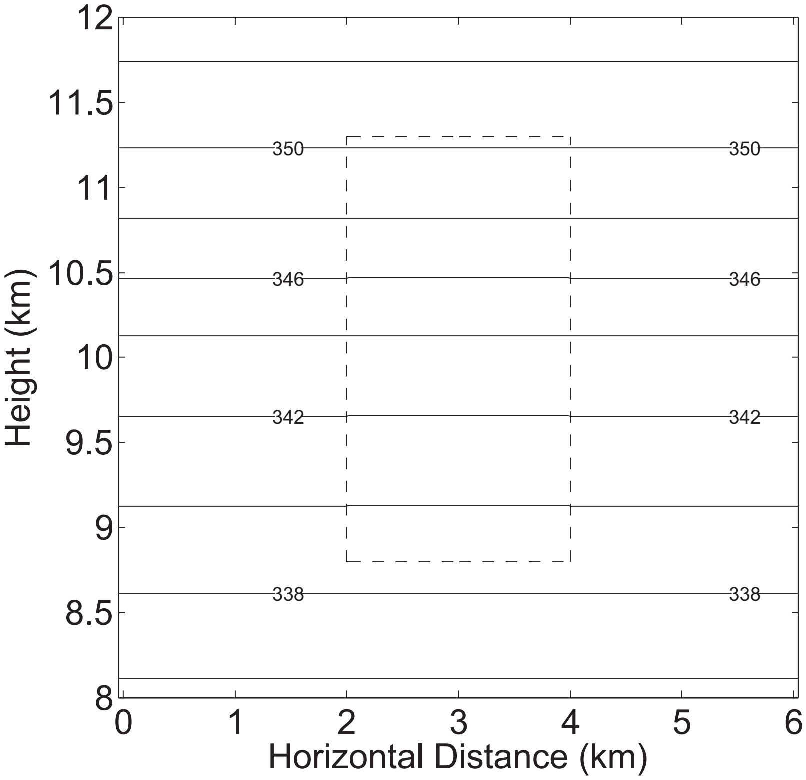

Figure F.1: Cross section of θ_v contours through a cloud at 0 s. In the case shown, the cloud has L=1 km and q_i=1 g kg^{-1}. However, it is representative of all clouds, regardless of L or q_i

F.2 Case 1: $S = 1.1 \times 10^{-4}$, $E = 150$

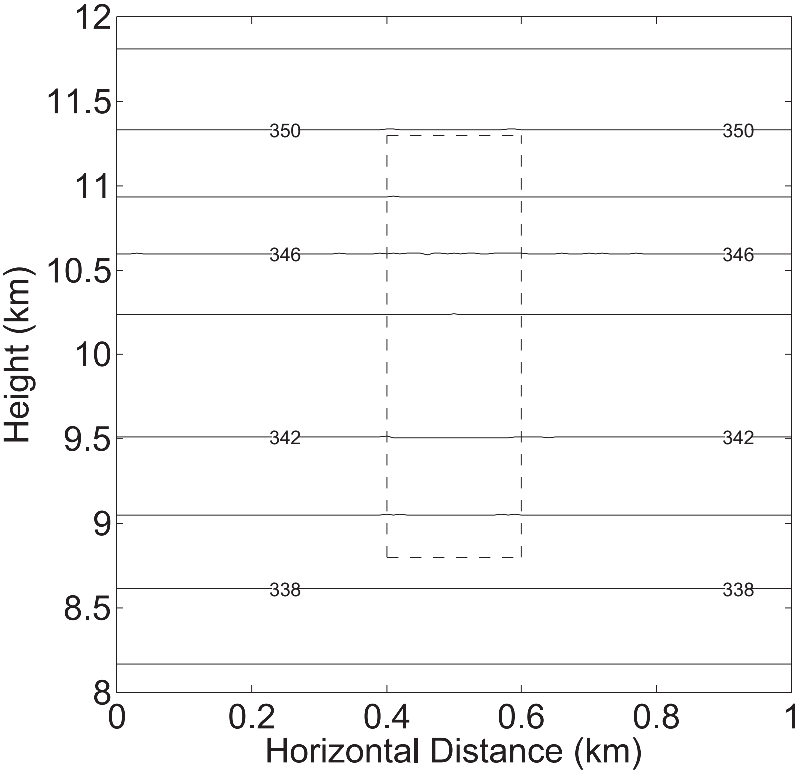

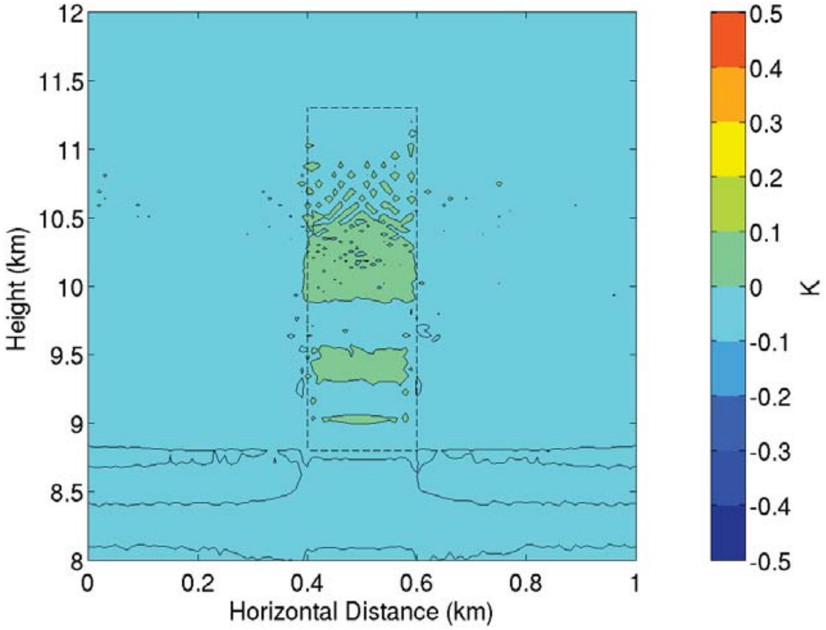

Figure F.2: Cross section of θ_v contours through a cloud with L=100 m and q_i=0.01 g kg^{-1} after 3600 s of simulation as well as the difference between the final and initial states

F.3 Case 2: $S = 1.1 \times 10^{-3}$, $E = 150$

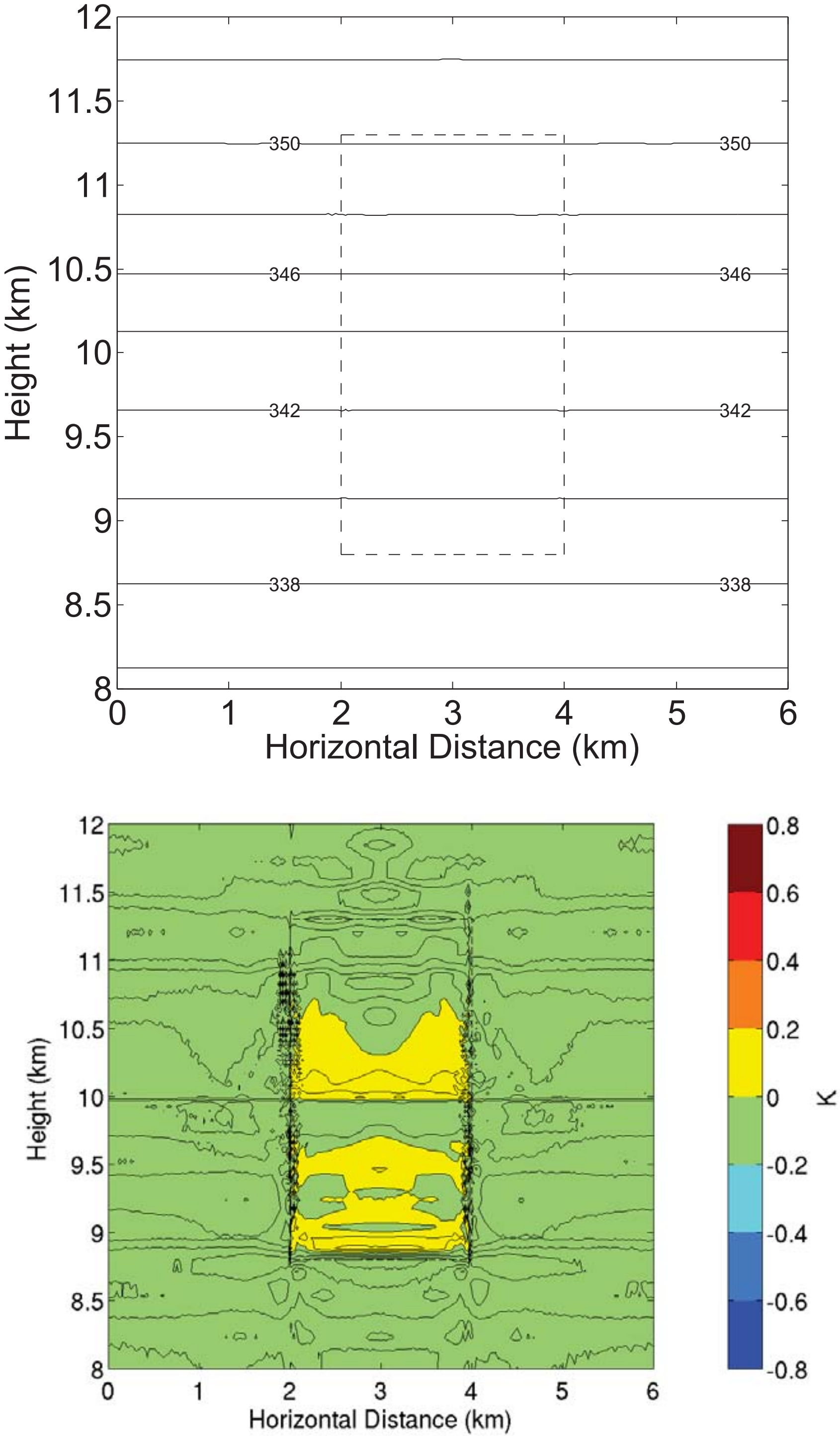

Figure F.3: Cross section of θ_v contours through a cloud with L=1 km and q_i=0.01 g kg^{-1} after 3600 s of simulation as well as the difference between the final and initial states

F.4 Case 3: $S = 3.3 \times 10^{-3}$, $E = 35$

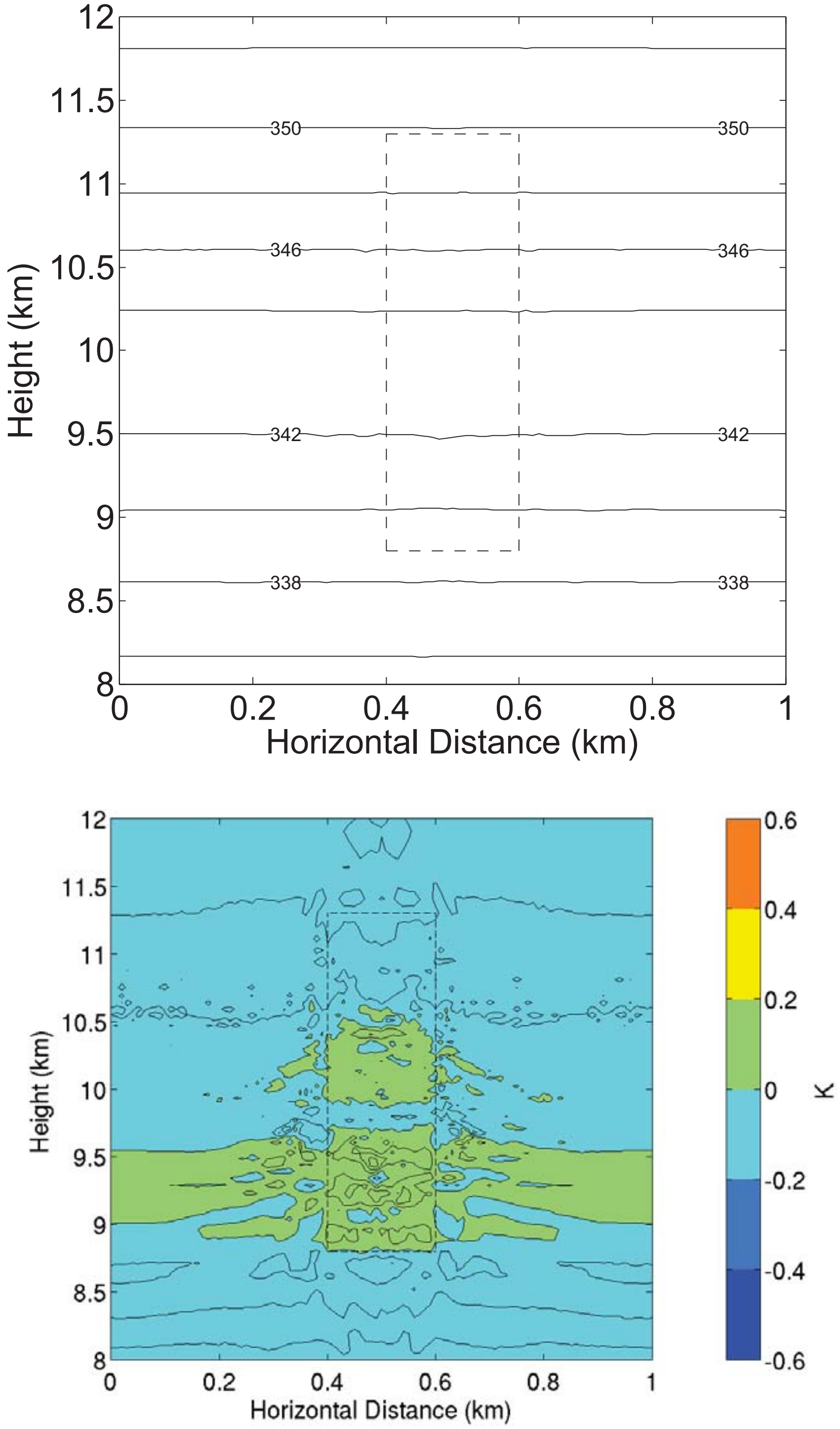

Figure F.4: Cross section of θ_v contours through a cloud with L=100 m and q_i=0.1 g kg^{-1} after 3600 s of simulation as well as the difference between the final and initial states

F.5 Case 4: $S = 0.011$, $E = 150$

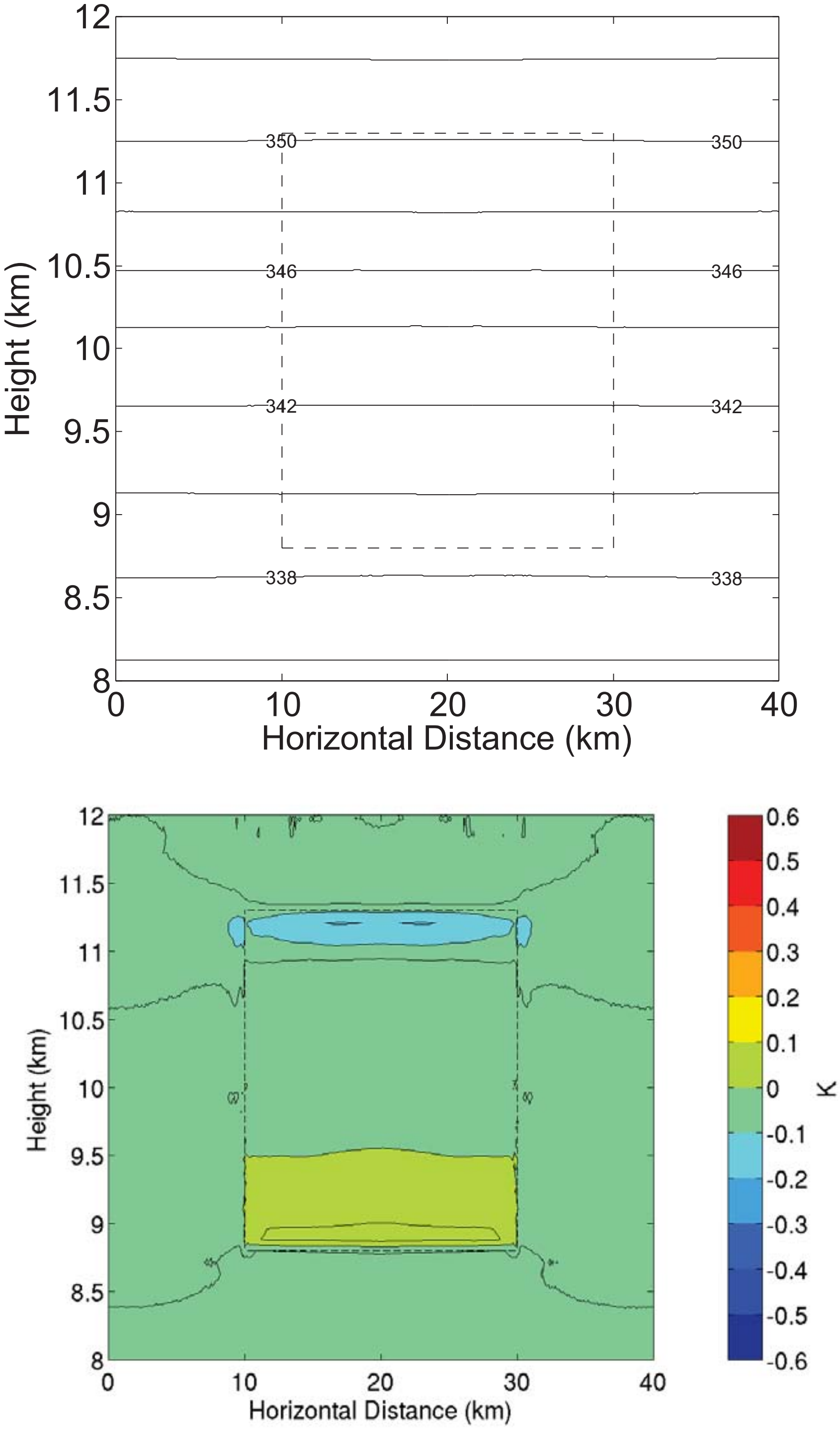

Figure F.5: Cross section of θ_v contours through a cloud with L=10 km and q_i=0.01 g kg^{-1} after 3600 s of simulation as well as the difference between the final and initial states

F.6 Case 5: $S = 0.033$, $E = 35$

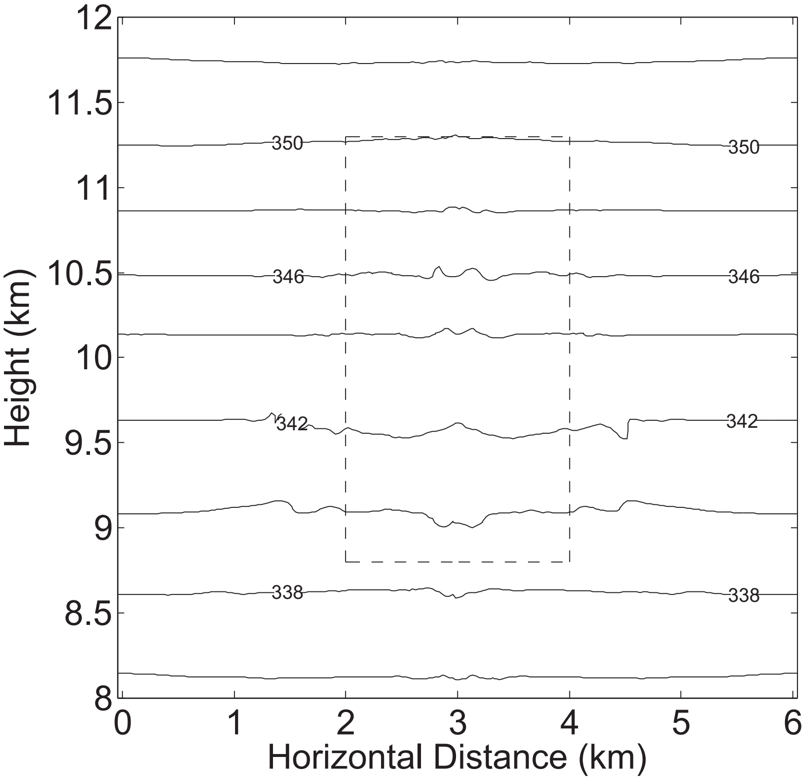

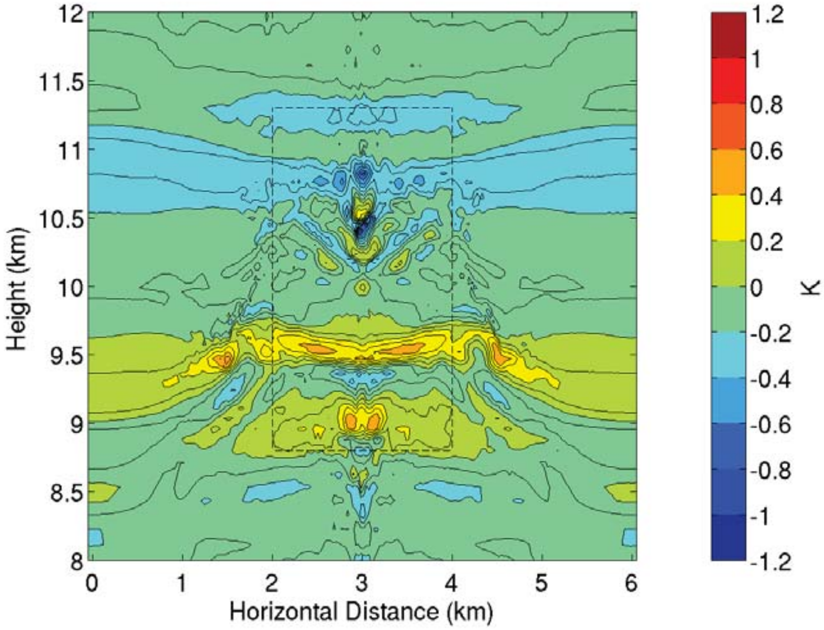

Figure F.6: Cross section of θ_v contours through a cloud with L=1 km and q_i=0.1 g kg^{-1} after 3600 s of simulation as well as the difference between the final and initial states

F.7 Case 6: $S = 0.33$, $E = 35$

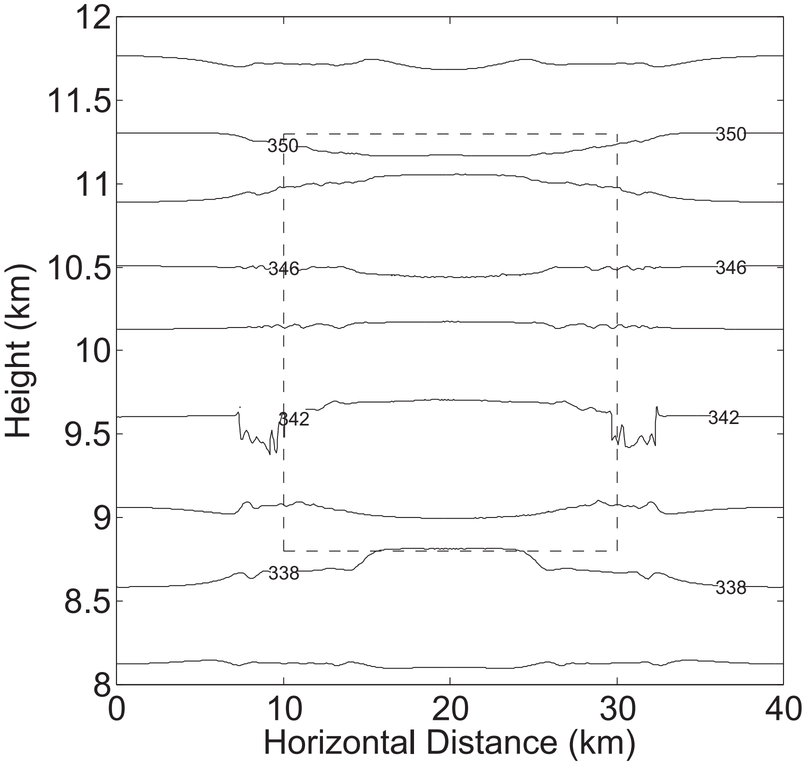

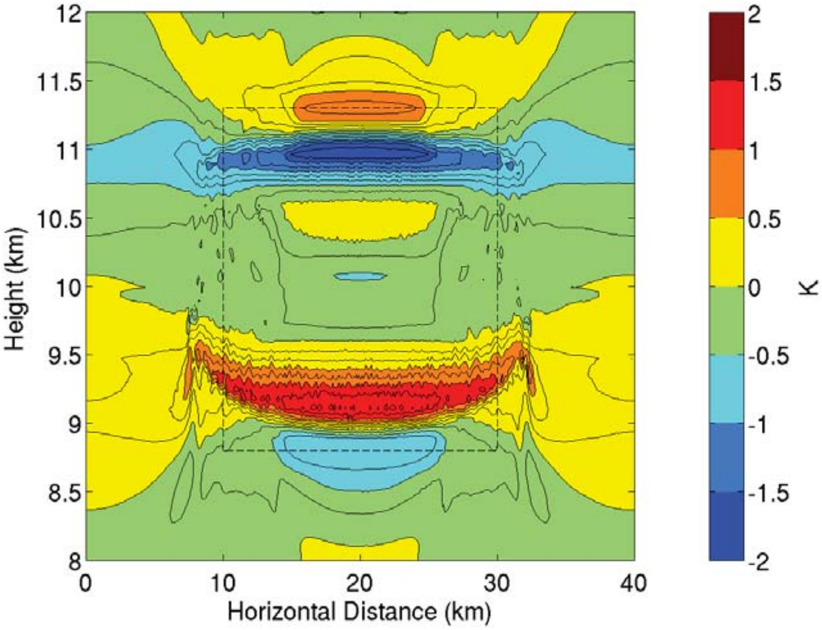

Figure F.7: Cross section of θ_v contours through a cloud with L=10 km and q_i=0.1 g kg^{-1} after 3600 s of simulation as well as the difference between the final and initial states

F.8 Case 7: $S = 13$, $E = 0.35$

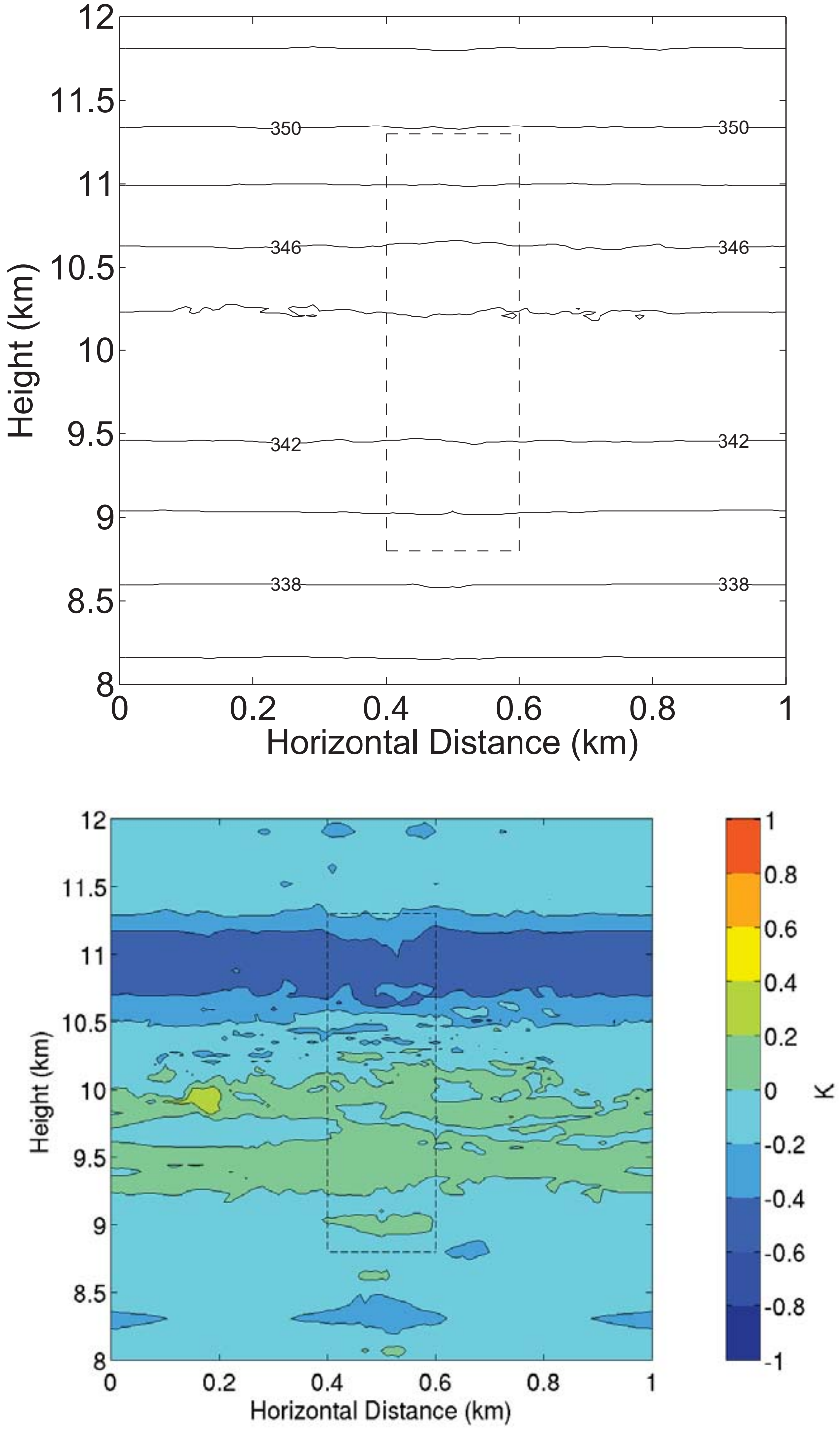

Figure F.8: Cross section of θ_v contours through a cloud with L=100 m and q_i=1 g kg^{-1} after 3600 s of simulation as well as the difference between the final and initial states

F.9 Case 8: $S = 130$, $E = 0.35$

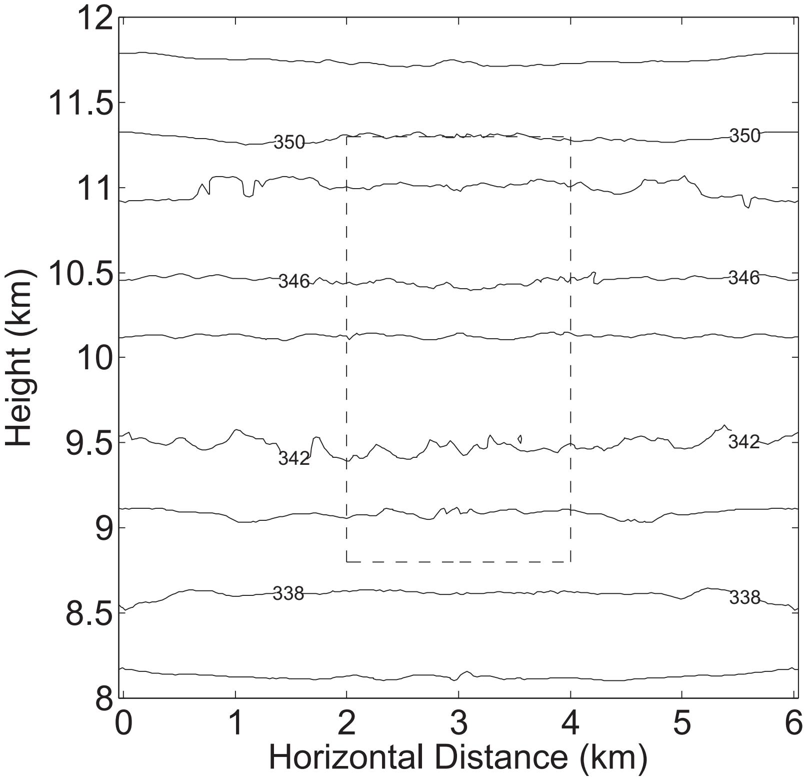

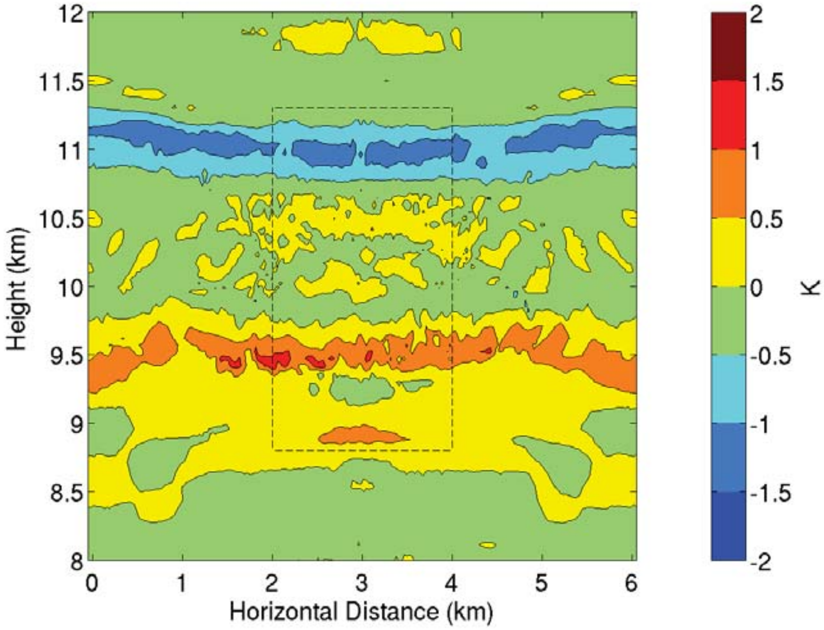

Figure F.9: Cross section of θ_v contours through a cloud with L=1 km and q_i=1 g kg^{-1} after 3600 s of simulation as well as the difference between the final and initial states

F.10 Case 9: $S = 1300$, $E = 0.35$

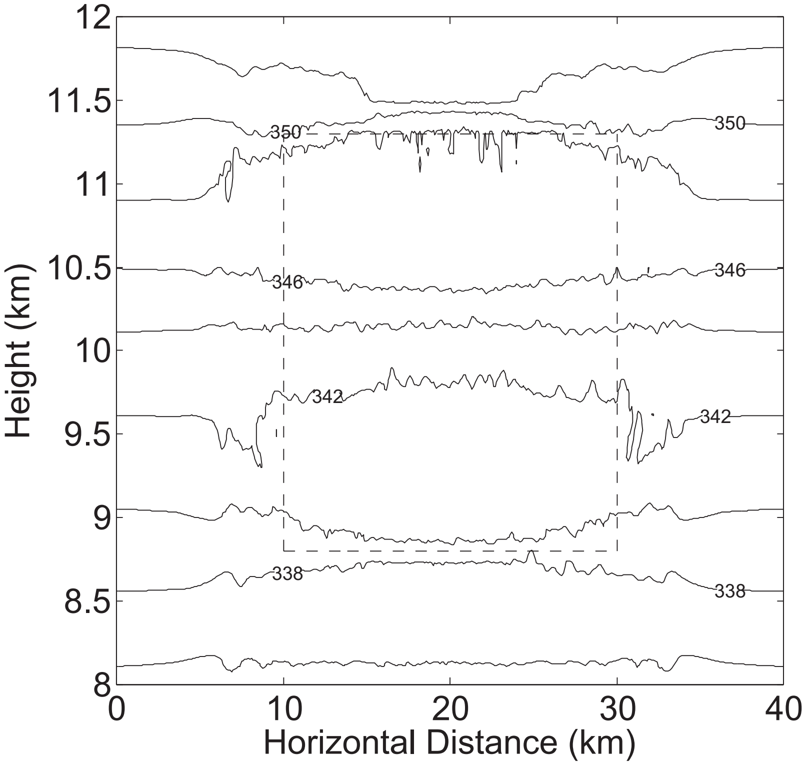

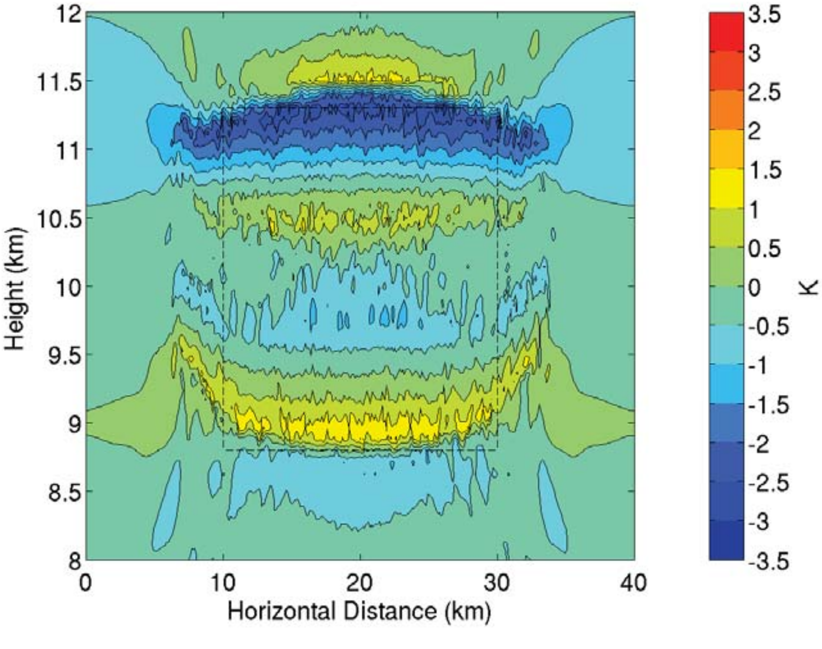

Figure F.10: Cross section of θ_v contours through a cloud with L=10 km and q_i=1 g kg^{-1} after 3600 s of simulation as well as the difference between the final and initial states

REFERENCES

Ackerman, S. A., W. L. Smith, H. E. Revercomb, and J. D. Spinhirne, 1990: The 27-28 october 1986 fire ifo cirrus case study: Spectral properties of cirrus clouds in the 8-12 micrometer window. *Mon. Wea. Rev.*, **118**, 2377–2388.

Ackerman, T. P., K. N. Liou, F. P. J. Valero, and L. Pfister, 1988: Heating rates in tropical anvils. *J. Atmos. Sci.*, **45**, 1606–1623.

Campbell, J. R., E. J. Welton, C. J. Flynn, D. D. Turner, J. D. Spinhirne, V. S. S. III, and I. H. Hwang, 2002: Full-time, eye-safe cloud and aeroslo lidar observation at atmospheric radiation measurement program sites: Instruments and data processing. *J. Atmos. and Oceanic Tech.*, **19**, 431–442.

Cess, R. D., 1976: Climate change: An appraisal of atmospheric feedback mechanisms employing zonal climatology. *J. Atmos. Sci.*, **33**, 1831–1843.

Corti, T., B. P. Luo, T. Peter, H. Vömel, and Q. Fu, 2005: Mean radiative energy balance and vertical mass fluxes in the equatorial upper troposphere and lower stratosphere. *Geophys. Res. Lett.*, **32**, L06802, doi:10.1029/2004GL021889.

Davis, A., A. Marshak, R. Cahalan, and W. Wiscombe, 1997: The landsat scale break in stratocumulus as a three-dimensional radiative transfer effect: Implications for cloud remote sensing. *J. Atmos. Sci.*, **54**, 241–260.

Deardorff, J. W., 1980: Stratocumulus-capped mixed layers derived from a three dimensional model of atmospheric turbulence. *Bound.-Layer Meteor.*, **18**, 495–527.

Dinh, T. P., D. R. Durran, and T. Ackermann, 2010: The maintenance of tropical tropopause layer cirrus. *J. Geophys. Res.*, **115**, D02104, doi:10.1029/2009/JD012735.

Dobbie, S. and P. Jonas, 2001: Radiative influences on the structure and lifetime of cirrus clouds. *Q.J.R.Meteorol.Soc.*, **127**, 2663–2682.

Droegemeier, K. K. and R. B. Wilhelmson, 1987: Numerical simulation of thunderstorm outflow dynamics. part i: Outflow sensetivity experiments and turbulence dynamics. *J. Atmos. Sci.*, **44**, 1180–1210.

Dufresne, J. L. and S. Bony, 2008: An assessment of the primary sources of spread of global warming estimates from coupled ocean-atmosphere models. *J. Climate*, **21**, 5135–5144.

Durran, D. R., T. Dinh, M. Ammerman, and T. Ackerman, 2009: The mesoscale dynamics of thin tropical tropopause cirrus. *J. Atmos. Sci*, **66**, 2859–2873.

Emanuel, K., 1981: A similarity theory for unsaturated downdrafts withing clouds. *J. Atmos. Sci.*, **38**, 1541–1557.

Emanuel, K. and M. Bister, 1996: Moist convective velocity and buoyancy scales. *J. Atmos. Sci.*, **53**, 3276–3285.

Evans, K. F., 1998: The spherical harmonics discrete ordinate method for three-dimensional atmospheric radiative transfer. *J. Atmos. Sci.*, **55**, 429–446.

Fu, Q., S. K. Krueger, and K. N. Liou, 1995: Interactions of radiation and convections in simulated tropical cloud clusters. *J. Atmos. Sci*, **52**, 1310–1328.

Fu, Q. and K. Liou, 2008: Parameterization of the radiative properties of cirrus clouds. *J. Atmos. Sci.*, **50**, 2008–2025.

Fusina, F. and P. Spichtinger, 2010: Cirrus clouds triggered by radiation, a multiscale phenomenon. *Atmos. Chem. Phys.*, **10**, 5179–5190, doi:10.5194/acp-10-5179-2010.

Garrett, T. J., L. Avey, P. I. Palmer, A. Stohl, J. A. Neuman, C. A. Brock, T. B. Ryerson, and J. S. Holloway, 2006a: Quantifying wet scavenging processes in aircraft observations of nitric acid and cloud condensation nuclei. *J. Geophys. Res.*, **111**, D23S51, doi:10.1029/2006JD007416.

Garrett, T. J., B. C. Navarro, C. Twohy, E. J. Jensen, D. G. Baumgardner, P. T. Bui, H. Gerber, R. L. Herman, A. J. Heymsfield, P. L. Lawson, P. Minnis, L. Nguyen, M. Poellot, S. K. Pope, F. P. J. Valero, and E. M. Weinstock, 2005: Evolution of a florida cirrus anvil. *J. Atmos. Sci.*, **62**, 2352–2371.

Garrett, T. J., M. A. Zulauf, and S. K. Krueger, 2006b: Effects of cirrus near the tropopause on anvil cirrus dynamics. *Geophysical Research Letters*, **33**, L17804.

— 2006c: Effects of cirrus near the tropopause on anvil cirrus dynamics. *Geophysical Research Letters*, **33**.
URL `doi:10.1029/2006GL027071`

Hartmann, D. L. and K. Larson, 2002: An important constraint on tropical cloud-climate feedback. *Geophysical Research Letters*, **29**, 1951–1955.
URL `doi:10.1029/2002GL015835`

Hartmann, D. L., M. E. Ockert-Bell, and M. L. Michelsen, 1992: The effect of cloud type on earth's energy balance: Global analysis. *J. Climate*, **5**, 1281–1304.

Heymsfield, A. J. and L. M. Miloshevich, 1991: On radiation and latent heat feedback in clouds: Implications and a parameterization. *J. Atmos. Sci.*, **48**, 493–495.

Hong, S., J. Dudhia, and S. Chen, 2004: A revised approach to ice microphysical processes for the bulk parameterization of clouds and precipitation. *Mo. Wea. Rev.*, **132**, 103–120.

James, J. F., 1999: *A Student's Guide to Fourier Transforms With Applications in Physics and Engineering*. Cambridge University Press, fourth edition.

Jensen, E. J., O. B. Toon, H. B. Selkirk, J. D. Spinhirne, and M. R. Schoeberl, 1996: On the formation and persistence of subvisible cirrus clouds near the tropical tropopause. *J. Geophysical Research*, **101**, 21,361–21,375.

Kanak, K. M., J. M. Straka, and D. M. Schultz, 2006: Numerical simulation of mammatus-like clouds in cirrus outflow anvils. *12th Conference of Cloud Physics*.

Kiehl, J. T., J. J. Hack, and B. P. Briegleb, 1994: The simulated earth radiation budget of the national center of atmospheric research community climate model ccm2 and comparisons wi the earth radiation budget experiment(erbe). *J. Geophysical Research*, **99**, 20,815–20,827.

Kittel, C. and H. Kroemer, 1998: *Thermal Physics*. W. H. Freeman and Company, second edition, 77,246,262 pp.

Krueger, S. K. and M. A. Zulauf, 2005: Radiatively-induced anvil spreading. *ARM Science Team Meeting Proceedings, Daytona Beach, Florida, March 14-18*, **15**, 1–9.

Kuang, Z. and D. L. Hartmann, 2007: Testing the fixed anvil temperature hypothesis in a cloud resolving model. *J. Climate*, **20**, 2051–2057.

Lilly, D. K., 1968: Models of cloud-topped mixed layers under a strong inversion. *Quart. J. Roy. Meteor. Soc.*, **94**, 292–309.

— 1988: Cirrus outflow dynamics. *J. Atmos. Sci.*, **45**, 1594–1605.

Middleton, G. V., 2000: *Data Analysis in the Earth Sciences Using Matlab*. Prentice Hall, first edition.

Morton, B. R., G. I. Taylor, and J. S. Turner, 1956: Turbulent gravitational convection from maintained and instantaneous sources. *Proc. R. Soc. A*, **234**, 1–23.

Ovarlez, J., J. Gayet, K. Gierens, J. Strom, H. Ovarlez, F. Auriol, R. Busen, and U. Schumann, 2002: Water vapour measurments inside cirrus clouds in northern and southern hemispheres during inca. *Geophysical Research Letters*, **29**, 1813.

Petty, G. W., 2004: *A first Course in Atmospheric Radiation*. Sundog Publishing, first edition, 198-199,281-312 pp.

Ramanathan, V., R. D. Cess, E. F. Harrison, P. Minnis, B. R. Barkstrom, E. Ahmad, and D. Hartmann, 1989: Cloud-radiative forcing and climate: Results from the earth radiation budget experiment. *Science*, **243**, 57–63.

Ramanathan, V., E. J. Pitcher, R. C. Malone, and M. L. Blackmon, 1983: The response of a spectral general circulation model to refinements in radiative processes. *J. Atmos. Sci.*, **40**, 605–630.

Raymond, D. J. and R. Rotunno, 1989: Response of a stably stratified flow to cooling. *J. Atmos. Sci.*, **46**, 2830–2837.

Rogers, R. R. and M. K. Yau, 1989: *A Short Course in Cloud Physics*. Butterworth and Heinemann, third edition.

Salby, M. L., 1996: *Fundamentals of Atmospheric Physics*. Academic Press, first edition.

Schneider, S. H., 1972: Cloudiness as a global climate feedback mechanism: The effects on the radiation balance and surface temperature of variations in cloudiness. *J. Atmos. Sci*, **29**, 1413–1422.

Schultz, D. M., K. M. Kanak, J. M. Straka, R. J. Trapp, B. A. Gordon, D. S. Zrnic, G. H. Bryan, A. J. Durant, T. J. Garrett, P. M. Klein, and D. K. Lilly, 2006: The mysteries of mammatus clouds: Observations and formation mechanisms. *J. Atmos. Sci.*, **63**, 2409–2435.

Sellers, W. D., 1969: A global climatic model based on the energy balance of the earth-atmospere system.

Senior, C. A., 1999: Comparison of mechanisms of cloud-climate feedbacks in gcms. *J. Climate*, **12**, 1480–1489.

Slingo, A., 1989: A gcm parameterization for the shortwave radiative properties of water clouds. *J. Atmos. Sci.*, **46**, 1419–1427.

Soden, B. J. and I. M. Held, 2006: An assesment of climate feedbacks in coupled ocean-atmosphere models. *J. Climate*, **19**, 3354–3360.

Squires, P., 1958: Penetrative downdraughts in cumulii. *Tellus*, **10**, 381–389.

Starr, D. O. and S. K. Cox, 1985a: Cirrus clouds. part i:a cirrus cloud model. *J. Atmos. Sci.*, **42**, 2663–2681.

— 1985b: Cirrus clouds. part ii:numerical experiments on the formation and maintenance of cirrus. *J. Atmos. Sci.*, **42**, 2682–2694.

Stephens, G. L., 2005: Cloud feedbacks in the climate system: A critical review. *J. Climate*, **18**, 237–273.

Stull, R. B., 2009: *An Introduction to Boundary Layer Meteorology*. Springer, tenth edition.

Tompkins, A. M., 2002: A prognistic parameterization for the subgrid-scale variability of water vapor and clouds in large-scale models and its use to diagnose cloud cover. *J. Atmos. Sci.*, **59**, 1917–1942.

Wallace, J. M. and P. V. Hobbs, 2006: *Atmospheric Science: An Introductory Survey*. Academic Press, second edition, 88-91 pp.

Wang, Z. and K. Sassen, 2002: Cirrus cloud microphysical property retrieval using lidar and radar measurements. part i: Algorithm description and comparison with in situ data. *J. Atmos. Sci.*, **41**, 218–229.

Webster, P. J. and G. L. Stephens, 1980: Tropical upper-tropospheric extended clouds: Inferences from winter monex. *J. Atmos. Sci.*, **37**, 1521–1541.

Wetherald, R. T. and S. Manabe, 1980: Cloud cover and climate sensetivity. *J. Atmos. Sci.*, **37**, 1485–1510.

Xu, K., M. T. Wong, B. A. Wielicki, L. Parker, Z. A. Eitzen, and M. Branson, 2007: Statistical analyses of satellite cloud object data from ceres. part ii: Tropical convective cloud objects during 1998 el niño and evidence for supporting the fixed anvil temperature hypothesis. *J. Climate*, **20**, 819–842.

Zemanksy, M. W. and R. H. Dittman, 1997: *Heat and Thermodynamics*. McGraw-Hill, seventh edition, 487 pp.

Zulauf, M. A., 2001: Modelling the effects of boundary layer circulations generated by cumulus convection and leads on large scale surface fluxes. *Ph.D. Thesis, The Univesity of Utah*.